EXPERIMENT AND THEORY OF A DRIFT WAVE IN THE LEVITATED OCTUPOLE

by

Evan Andrew Rose

A thesis submitted in partial fulfillment

of the requirements for the degree of

DOCTOR OF PHILOSOPHY

(Physics)

at the

University of Wisconsin - Madison

1982

EXPERIMENT AND THEORY OF A DRIFT WAVE

IN THE LEVITATED OCTUPOLE

Evan Andrew Rose

Under the supervision of Associate Professor Stewart C. Prager

A very coherent 30 kHz drift wave is observed in the Levitated Toroidal Octupole at the University of Wisconsin - Madison. The density and floating potential fluctuations have a well-defined spatial structure in the poloidal magnetic field. Radially the wave has a standing wave structure with amplitude peaked in regions of locally bad magnetic curvature. Poloidally the wave has a standing wave structure with odd symmetry; nodes are located in the regions of locally good magnetic curvature. The wave propagates toroidally in the electron diamagnetic drift direction with a wavelength of 20 centimeters. No changes occur in the wave structure as the plasma is varied over three orders of magnitude in density and beta (from 1×10^{9}/cc, $\beta = 0.004\%$ to 2×10^{12}/cc, $\beta = 8\%$).

The drift wave is observed for a limited range of ion gyroradius, being stabilized for larger and smaller ion gyroradius. Application of a toroidal magnetic field also stabilizes the wave.

No enhanced transport is observed, despite the 20 - 30% relative amplitude of the density fluctuation. Observed magnetic fluctuations are consistent with diamagnetic effects, and no evidence for coupling to an Alfven wave is seen.

The drift wave is modeled with a linear kinetic theory which treats finite ion gyroradius and the poloidal variation of both the magnetic field strength and the magnetic drift velocity. Electron Landau damping is included, and trapped particle effects are ignored. The theory is able to predict all the major trends in spatial structure: odd poloidal symmetry, stabilization of the wave with increasing good magnetic curvature, and a limited range of ion gyroradius for instability.

ACKNOWLEDGEMENTS

I should like to thank Professor Stewart C. Prager for his enthusiastic support of my research effort. His ready advice and counsel have been invaluable in the pursuit of this project.

Thanks is also extended to those who, as fellow students, spent their time and effort introducing me to the research effort at the Unversity of Wisconsin. Dr. C. J. Armentrout was particularly helpful with explaining the concepts and operation of the levitated octupole and with introducing me to his data analysis techniques; M. C. Zarnstorff provided considerable aid with the PDP11/20 data acquisition system; and Dr. J. R. Drake provided an opportunity to learn to operate the levitated octupole at an early date under a watchful eye.

Fellow student M. A. Makowski is thanked for the many hours he spent giving his perspective on the problems and ideas that I brought to him.

Professor J. D. Callen provided help with the theoretical aspects of this work.

Day to day operation of the levitated octupole was made possible, in large part, through the efforts of John Laufenberg.

Work supported by U. S. D. O. E.

DEDICATION

This thesis is dedicated to Mr. Fred Holzhauser,

teacher and respected friend.

CHAPTER 1 - INTRODUCTION

Drift waves, and their role in promoting anomolous plasma transport, have elicited an extremely high level of interest on the part of plasma theorists and experimentalists. This interest has led to a multitude of studies of the drift wave over a period spanning three decades.

The theoretical work has been extensive,[1] using several different approaches to examine drift waves under many different conditions. The effects of gradients in density, temperature, magnetic field, and impurity concentration have all been investigated, as have the effects of particle trapping in local magnetic wells. The role of magnetic shear in promoting drift wave stability has been actively studied for more than ten years and continues today[2]. The complexity of the drift wave problem and the diversity of the effects to be considered, coupled with the importance of anomolous transport in plasma devices, ensures that drift waves will remain a field of active inquiry for many years.

The experimental study of drift waves has also proceeded, but at a much slower pace than the theoretical studies. There is a shortage of experimental results for comparison with theoretical models. This shortage is due, in part, to the difficulty of setting up an experiment to study a particular aspect of drift wave behavior, free of unwanted effects introduced by the experimental device. In addition,

the drift wave may be difficult to detect and its characterization elusive.

One area of notable experimental success has been the study of drift waves in Q-machines[3]. These simple linear devices are particularly free of competing instabilities which could obscure drift wave observations. Further, they can be diagnosed with Langmuir probes, a simple diagnostic tool which can give local measurements of density and potential. Coherent drift waves have been observed, with properties that are in good agreement with theory.

The experimental results in toroidal devices, such as tokamaks, has been disappointing, with a generally poor application of the theory to experimental results. The toroidal devices exhibit complicated magnetic field geometries. In the case of the tokamak, plasma currents are required to establish the magnetic field, adding a complication to the experimental situation. Further, a limited range of poloidal to toroidal field ratios are available at which MHD instabilities are suppressed, limiting the versatility of the tokamak for drift wave studies. A further complication is that the high temperatures and currents in tokamaks severely restrict the use of Langmuir probes for drift wave diagnosis, necessitating the use of remote diagnostics, such as microwave scattering. These remote diagnostics lack the ability of Langmuir probes to sense local plasma properties in detail. The frequency spectra of fluctuations in tokamaks tend to be broad,[4] limiting the analysis.

The levitated octupole is a toroidal device, and it has a complicated magnetic geometry. However, it is much better suited to drift wave studies than a tokamak. The magnetic field structure is stable to MHD stabilities,[5] a property that does not depend on the poloidal to toroidal field ratio. Thus the field ratio can be varied without losing the suppression of MHD instabilities. The magnetic fields themselves are generated with external conductors, so that the plasma-perturbing currents necessary to the tokamak are not present for the octupole. Further, diagnosis with Langmuir probes is possible for the octupole.

The most telling argument in favor of using the levitated octupole for drift wave studies is the observation of an extremely coherent, long-lived wave, with a well-defined spatial structure. This is in contrast to the broad spectrum of waves seen in the tokamak.

The appearance of an extremely coherent drift wave in the levitated octupole offers a unique opportunity to do a definitive drift wave study in a toroidal device. Such a study is undertaken and reported in this paper. An outline of the approach is given below.

In chapter 2 the levitated octupole is described. A physical description is given and the magnetic field geometry is explained in some detail. Flux coordinates based on the magnetic field geometry of the octupole are introduced for later reference. The properties of plasmas produced by plasma guns are defined.

In chapter 3 drift waves are introduced with a simple theoretical description. The stable drift wave in a plasma slab is described, and instability mechanisms and wave induced transport are discussed.

In chapter 4 diagnostic techniques are discussed. Analysis of Langmuir probe data with the correlation function and fast Fourier transform are described in some detail.

In chapter 5 the experimental observations are presented. With Langmuir probes to measure fluctuations in plasma density and floating potential, the techniques of chapter 4 are used to define the radial, poloidal, and toroidal structure of the drift wave. The wave's dependences on plasma density, ion gyroradius size, and toroidal field are presented. Plasma transport is considered and magnetic fluctuations discussed. A comparison of these results is made with the observations of a drift wave in the Princeton linear quadrupole.

In chapter 6 a dispersion relation is derived for a drift wave in the levitated octupole. Examples of two theoretical approaches are chosen from the literature and discussed. The approach of Coppi and Minardi is selected, and the derivation of the dispersion relation is presented in detail.

In chapter 7 the results of the theoretical model are presented and the implications for the octupole are discussed. Aspects of the observed poloidal and radial structure and the ion gyroradius dependence are found to be in agreement with theory.

References for Chapter 1

1. W. M. Tang, "Microinstability Theory in Tokamaks: A Review", PPPL-1354 (1977).

2. L. Chen, F.-J. Ke, M.-J. Xu, S.-T. Tsai, Y. C. Lee, and T. M. Antonsen, Jr., "On the Stability of Drift Waves with the Integral Eigenmode Equation", PPPL-1842 (1981).

3. H. W. Hendel and T. K. Chu, "Collisional Drift Instabilities", in Methods of Experimental Physics, ed. R. H. Lovberg and H. R. Griem, (Academic Press, New York, 1971), volume 9A, chapter 9.

4. E. Mazzucatto, "Low-Frequency Microinstabilities in the PLT Tokamak", Physics of Fluids 21, 1063 (1978).

5. T. Ohkawa and W. D. Kerst, "Multipole Magnetic Field Configurations for Stable Plasma Confinement", Nuovo Cimento 22, 784 (1961).

CHAPTER 2 - OCTUPOLE DESCRIPTION

A. Mechanical

The levitated octupole is shown in figure 2.1, and its parameters are defined in table 2.1. The vacuum vessel has a major radius of 139 cm, inside height of 112 cm, and inside width of 120 cm. The aluminum walls are 5 cm thick. Four internal rings of 8.9 cm minor radius rest on a total of sixteen titanium supports of about one centimeter diameter. The supports are manipulated pneumatically by levators bolted to the octupole wall[1]. There are five levators each for the outer rings and three each for the inner rings, with each levator supporting about 300 pounds. Each levator consists of a piston connected to a shaft, the motion of the piston being controlled by valves applying pressurized air, and the motion of the shaft operating a lever which moves the supports. Vacuum integrity is maintained with stainless steel bellows attached to the lever arm of each levator. The supports can be removed from the octupole into wall-mounted vacuum housings for a 20 millisecond period. During this time the rings are free from the plasma-disturbing supports, but are subject to gravitational and JxB forces. By making adjustments to the rings' supported positions, the balance of these forces can be altered. Ideally, the rings are positioned to feel no net forces, and are caught softly by the returning supports. However, the magnetic field strength in the octupole is a function of time, which

means that there are upper limits on the magnitude and duration of magnetic fields which can be used in the octupole.[2]

The experiments described below take place with a base pressure for the octupole's 8.6 cubic meter volume of about 2x10-8 Torr, as determined by ionization gauges. This pressure is obtained by use of a turbo-molecular pump, titanium getters, liquid nitrogen cold panel, and helium cryopanel. A residual gas analyser provides information about which gases constitute the background pressure and helps determine whether atmospheric leaks are present.

B. Magnetic Fields

B1. Poloidal Magnetic Field

The levitated octupole's poloidal magnetic field (figures 2.2 and 2.3) is produced by electrical currents flowing in four internal rings and the octupole's conducting wall. The four aluminum rings form the secondary winding of a transformer, whose 60 ton laminated iron core is driven by a 90 turn primary winding connected to a 48 millifarad capacitor bank. A poloidal gap in the octupole's aluminum shell allows magnetic field penetration to the interior of the octupole. Continuity windings encircle the iron core and connect to either side of the poloidal gap. These continuity windings allow image currents from the rings to flow in the wall, confining the magnetic flux within the octupole. As time passes, resistive losses within the wall and rings allow magnetic flux to soak into these

structures, escaping to the outside after passing through the wall or annihilating itself at the rings' centers.

The magnetic field can be run in either a half sine wave mode or a crowbar mode. In the half sine wave mode ignitrons are fired to allow the poloidal field capacitor bank to discharge through the primary windings of the transformer. After 21.5 milliseconds the current in the primary winding reaches a maximum, the magnetic field strength in the octupole having peaked at about 20 milliseconds, earlier due to soak-in effects. At the end of the 43 millisecond half sine wave period the current in the primary winding returns to zero and the ignitrons open, leaving the capacitor bank charged with opposite its initial polarity and the field in the octupole close to zero. In the crowbar mode, the current peak through the primary winding is detected, causing an ignitron to close, shorting the poloidal capacitor bank and allowing the primary current to continue flowing. The crowbar ignitron closes a few milliseconds after peak field is reached, and common practice is to approximate the magnetic field in the octupole after crowbar by the situation at 25 milliseconds into the half sine wave case.

For poloidal capacitor bank voltages lower than 500 volts switching is done with a silicon controlled rectifier, and crowbar operation is through a solid state diode.

Willig and Morin[3,4] have produced flux plots for the octupole geometry, taking into account the resistive losses in the walls and rings, which lead to magnetic field soak-in. Figure 2.2 shows a plot

of the magnitude of the magnetic field in the octupole at 25 milliseconds after field initiation. The plot shows field strength in kilogauss, assuming a 5 kilovolt initial charge on the poloidal capacitor bank. Figure 2.3 shows the flux surfaces for the octupole at 25 milliseconds. A flux surface is defined by rotating a field line toroidally about the octupole. The convention for the levitated octupole is to label flux surfaces from zero to ten, neighboring surfaces containing one tenth of the total magnetic flux at peak field. By 25 milliseconds the magnetic field is past its peak and some flux has leaked into the rings and walls, so that only surfaces two through nine are shown in figure 2.3 as still inside the vacuum region of the octupole.

Measurements by the author show 1/e decay times for the magnetic field of 70 milliseconds midway between the lower outer ring and the wall and 130 milliseconds at a position on the midcylinder 20 centimeters above the lower lid. Magnetic field soak-in reduces decay times more in regions of the octupole which are closely bounded by conductors.

The flux surfaces form two classes: those which encircle only one ring (private flux) and those encircling four rings (common flux). (Although some field lines encircle two rings, these are very rare.) The two classes of flux surface are divided by a surface called the separatrix, and designated Ψ_{sep} in figure 2.3. The separatrix is the surface with the largest volume per unit flux. Flux surfaces closer to a ring or a wall have progressively less

volume per unit flux associated with them, until the critical surface Ψ_{crit} is reached. The volume per unit flux increases outside the critical surface. This magnetic field geometry is commonly referred to as "minimum average B" geometry, and such a geometry has the benefit of being stable to flute waves or interchange moodes.

Plasmas in the octupole, particularly gun-produced plasmas, tend to have their peak density on the separatrix due to MHD stability considerations. Plasma parameters, such as density and temperature, are generally constant along a field line. This constancy of plasma parameters along a field line allows the characterization of the plasma by sampling in the ten centimeter region between a ring and a wall, known as the "bridge". The indentations in the wall on the horizontal midplane are referred to as "noses", while the upper and lower walls are referred to as "lids". Common flux in the bridge regions have "bad" magnetic curvature from the standpoint of MHD stability, while the noses and central lids are characterized by "good" magnetic curvature. In bad curvature regions the local volume per unit flux increases from the separatrix toward the wall, while in good curvature regions this quantity decreases. However, good curvature predominates in the octupole when the average is taken over a common flux surface. For private flux surfaces the curvature is locally good everywhere.

B2. Toroidal Magnetic Field

The levitated octupole also has the capability of producing a toroidal magnetic field with a magnitude inversely proportional to

radial position (as measured from the octupole's center line). Electrical currents flow in the octupole's aluminum wall, which forms a single-turn magnetic field coil fed by 44 pairs of cables attached to either side of an insulated toroidal gap. The cable pairs form parallel secondary windings of a transformer with a 40 turn primary winding, which is driven by a 370 millifarad capacitor bank.

The addition of toroidal field does not modify the flux plot of figure 2.3. However, individual field lines no longer close on themselves, but make excursions in the toroidal direction around the octupole. Field lines on neighboring flux surfaces will, in general, have different orientations, a condition known as magnetic shear. Magnetic shear is of interest because of the possibility that it stabilizes microinstabilities.

C. Flux Coordinates

In figure 2.3 a coordinate system is shown, labeled psi, chi, and theta (ψ, χ, and θ). This is a flux coordinate system, standard for complex magnetic field geometries. The coordinates are defined below.

PSI, the radial coordinate, is the poloidal flux enclosed by a line drawn around the octupole toroidally. Mathematically $\Psi = \int dR\, B_p R$, where B_p is the poloidal magnetic field strength and R is the radial position, measured from the octupole's center line. The flux surfaces of figure 2.3 correspond to surfaces of constant psi value.

CHI, the parallel coordinate, is the poloidal magnetic scalar potential, found by taking the line integral of the poloidal magnetic field strength along a field line. Mathematically $\chi = \int dl\ B_p$, where B_p is the poloidal magnetic field strength and dl is a unit distance along a field line. From Maxwell's equations we know that this quantity, when integrated over a closed contour, is proportional to the current through the contour-defined surface. Thus chi measured around a private flux surface gives the current in a single ring, while chi measured around a common flux surface gives the current total of all four rings. Figure 2.4 is a sketch of the chi coordinate system of the octupole, superimposed on a flux plot. Note the ratio of inner ring current to outer ring current is 6.44 to 3.40. The origin of the chi coordinate is the inner half of the horizontal midplane. The total contribution of the four rings brings chi to 19.68 in arbitrary units, convertible to gauss-centimeters using the factor 450 times V, where V is the voltage on the poloidal field capacitor bank.

THETA is the toroidal coordinate, measured in radians clockwise from the poloidal field gap as viewed from above the octupole. The octupole is treated as symmetrical with respect to the toroidal coordinate, a good approximation when the poloidal field is slowly changing.

The relationship $\nabla\Psi \times \nabla\Theta = \nabla\chi = \vec{B}_p$ is satisfied by the coordinate system.

D. Plasmas

Hydrogen plasmas are produced in one of three coaxial plasma guns,[5] designated the small, intermediate, and large guns according to the relative plasma densities they produce. Each gun consists of two concentric metal cylinders, separated at the back by an insulating plate and open at the front. Gas is puffed into the rear section of the gun through holes in the inner conductor, and the gas is broken down by the discharge of a capacitor bank across the coaxial gun. A current sheet travels from the rear to the front of the gun, ionizing the gas and accelerating the resulting plasma via JxB forces until the plasma is ejected from the front of the gun. Gun operation has been shown to be dependent on the volume of the gas puff, time delay between gas puff and initiation of breakdown, design of the coaxial section, and inductance and resistance in the transmission line to the capacitor bank[6]. Plasma parameters such as temperature, density, and ionized fraction can be modified.

Gun-produced plasmas are injected radially into a previously established magnetic field within the octupole, a process which has been studied extensively in the doctoral thesis of D. M. Meade[7]. Essentially, the plasma enters the magnetic field region of the octupole by becoming polarized as a result of Lorentz forces. The polarization electric field is in the toroidal direction and of the correct sign to produce a radial ExB velocity drift (see section 3A) allowing the plasma to continue penetrating the magnetic field, approaching the separatrix in the octupole center. After crossing

the separatrix, the plasma stream encounters field lines of opposite direction and attempts to establish a polarization electric field of opposite polarity. But these are field lines that the plasma has previously encountered, and the good electrical conductivity parallel to field lines causes the toroidal electric field to be shorted out, bringing radial plasma motion to a halt. Toroidal plasma motion takes place through the establishment of a radial electric field by means of the Lorentz force, producing two oppositely directed plasma streams traveling toroidally until they meet. The plasma thus fills the octupole by cross-field motion in a process that takes a few hundred microseconds.

The process of plasma penetration and trapping is more efficient in a stronger magnetic field, as evidenced by an increase in plasma density and ion temperature as the magnetic field strength (poloidal and toroidal) is increased within the available range. Levitation of the rings has little effect on the initial plasma parameters, but decay times for density and temperature are lengthened by the removal of the ring supports.

The various gun-produced plasmas are briefly characterized below.

D1. Intermediate Density Gun

The intermediate density gun is capable of producing plasmas in the $1x10^{9}$/cc to $1x10^{12}$/cc density range, depending on the gun's operating parameters. When operated with a full-sized gas reservoir, the gun produces a denser, cooler plasma. If the size of the

reservoir is drastically reduced or the hydrogen in the reservoir is reduced to a fraction of atmospheric pressure, the gun produces a less dense, but much hotter plasma.

With full gas reservoir, the gun produces a plasma with a 10 eV ion and electron temperature two milliseconds after injection. Run in the "starved" mode, the gun produces a plasma with ion temperature increased to 30 to 40 eV, with somewhat lower temperatures at lower magnetic field strengths.

D2. Large Density Gun

The large density gun is capable of producing plasmas in the 10^{12}/cc density range. Although the initial ion temperature is highly dependent on magnetic field strength, by one millisecond after injection all cases tested showed ion temperatures of 6 to 7 eV. Thus the large gun may be characterized as a source of high density, but low temperature plasma.

(The results quoted above pertain to the large gun as modified by A. Kellman in late 1979. At that time a considerably larger capacitor bank was attached to the gun, and ballistic temperatures of 400 eV were obtained, as opposed to the 30 eV ballistic temperatures quoted by G. A. Navratil[8].)

D3. Small Density Gun

The small density gun produces a plasma in the 10^{9}/cc to mid-10^{10}/cc density range, depending on the mode of operation, as explained below.

The small density gun produces a large flux of neutral particles, due to poor ionization of the gas it is fed. In order to minimize the amount of neutral gas entering the octupole, the gun is placed at the end of a differentially pumped drift tank. The room temperature neutrals are effectively screened out of the octupole, but the density and temperature of the plasma are also reduced by passage through the drift tank and injection into the octupole through a hole in the wall. Two milliseconds after injection the ion temperature is 30 eV and the electron temperature is 7 eV with this scheme.

In order to improve the fraction of plasma reaching the octupole after passage through the drift tank, a guide field using Ioffe bars was installed by R. S. Post. Density and temperature are increased, with the ion temperature at two milliseconds rising to about 80 eV with the rings supported, 105 eV with levitation.

Further increases in ion temperature are possible by increasing the pressure of the gas in the gun's reservoir. An ion temperature of 125 eV is obtainable at two milliseconds after plasma injection with rings supported.

The ion temperature decay time of the small gun is found to increase when the rings are levitated. With 2 kV on the poloidal field capacitor bank and using the guide field, the 1/e decay time of T_i at 2.5 milliseconds after injection is 6.2 milliseconds for levitated rings and 3.4 milliseconds for supported rings.

Table 2.1 - Levitated Octupole Parameters

Physical

Vacuum Tank	
Major Radius	139 cm
Height	112 cm
Width	120 cm
Volume of Vacuum	8.6 m^3
inside Ψ_{crit}	7.9 m^3
Wall Thickness	5 cm
Hoops	
Minor Radius	8.9 cm
Major Radius Inner	99 cm
Outer	179 cm

Electrical

Poloidal Magnetic Field		Toroidal Magnetic Field	
Capacitor Bank		**Capacitor Bank**	
Capacitance	.048 F	Capacitance	0.37 F
Voltage	5 kV	Voltage	450 V
Energy	600 kJ	Energy	37 kJ
Transformer Core		**Transformer Core**	
Inductance (with leads)	3.9 mH	Inductance (with leads)	0.5 mH
No. of Windings	90	No. of Windings	40
Peak Flux	0.72 Wb	Peak Flux	0.15 Wb
Currents (maximal)		**Currents (maximal)**	
Wall	1.42 MA	Wall	500 kA
Inner Ring	0.46 MA	Primary Winding	12 kA
Outer Ring	0.25 MA		
Primary Winding	17.5 kA		
Half Sine Period	43ms	Half Sine Period	43 ms

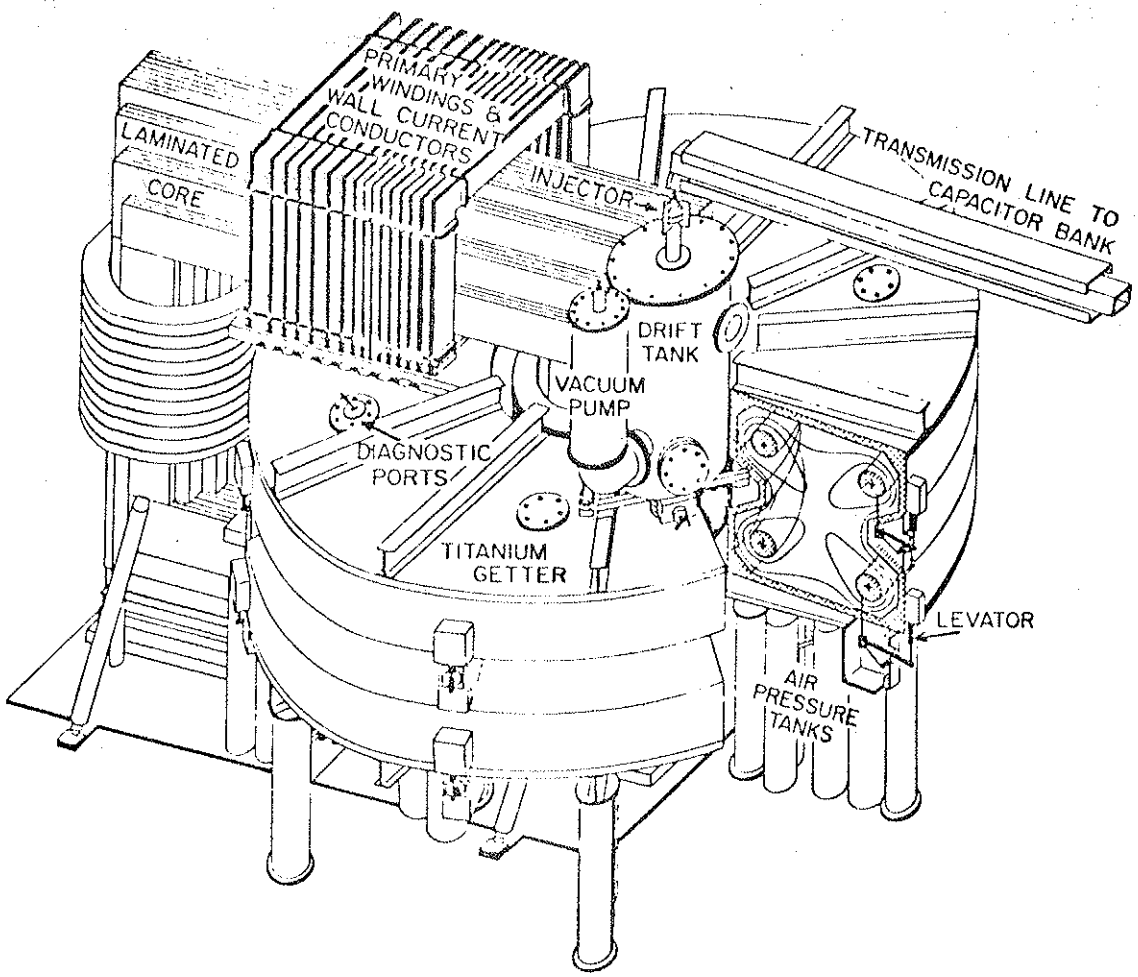

WISCONSIN LEVITATED OCTUPOLE

Figure 2.1 - The Wisconsin Levitated Octupole

The diagram shows the experimental apparatus with many of its salient features: internal rings, levators, magnetic core, drift tank with small density gun (injector) and vacuum pumping ports, etc. Octupole parameters are listed in table 2.1.

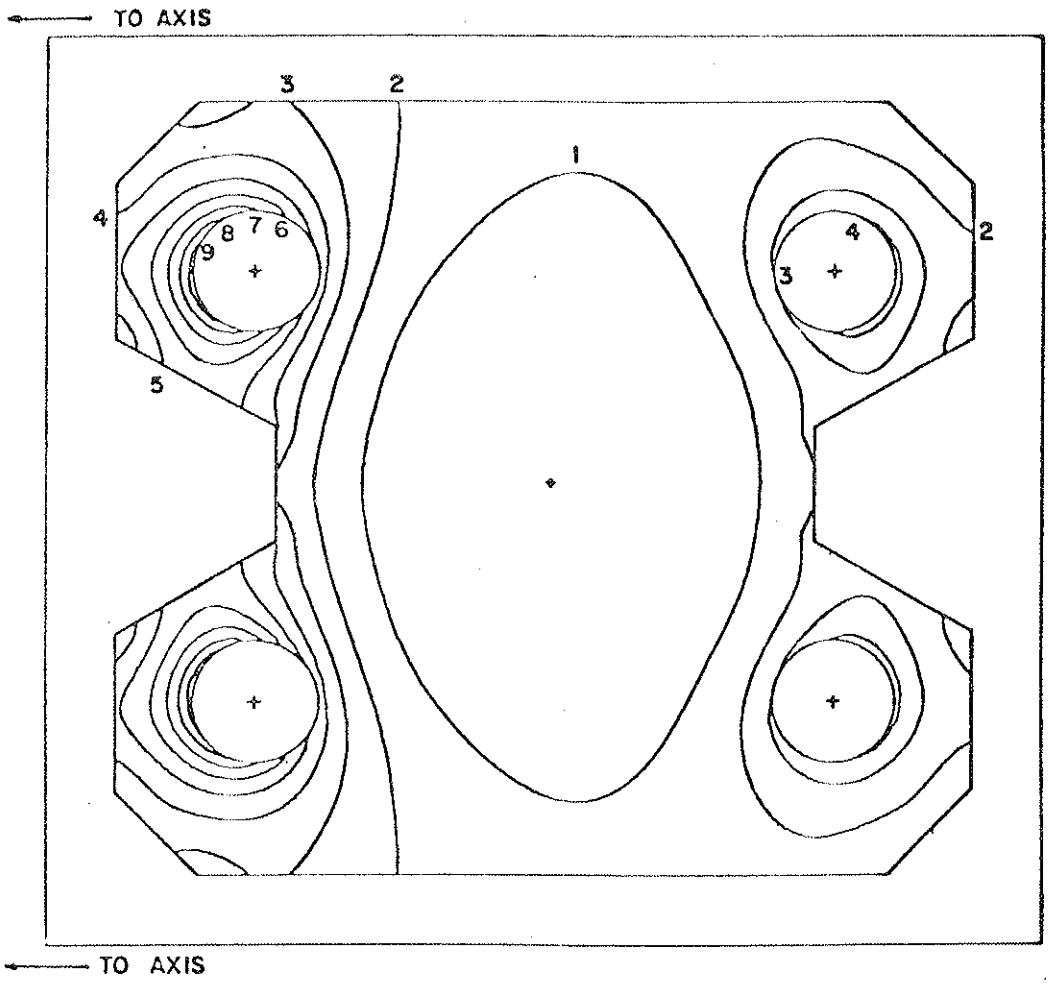

Figure 2.2 - Magnetic Field Strength in the Levitated Octupole Poloidal magnetic field contours are shown on a cross section of the octupole. Field strength is in kilogauss for a time 25 milliseconds after field initiation with 5 kilovolts on the poloidal field capacitor bank.

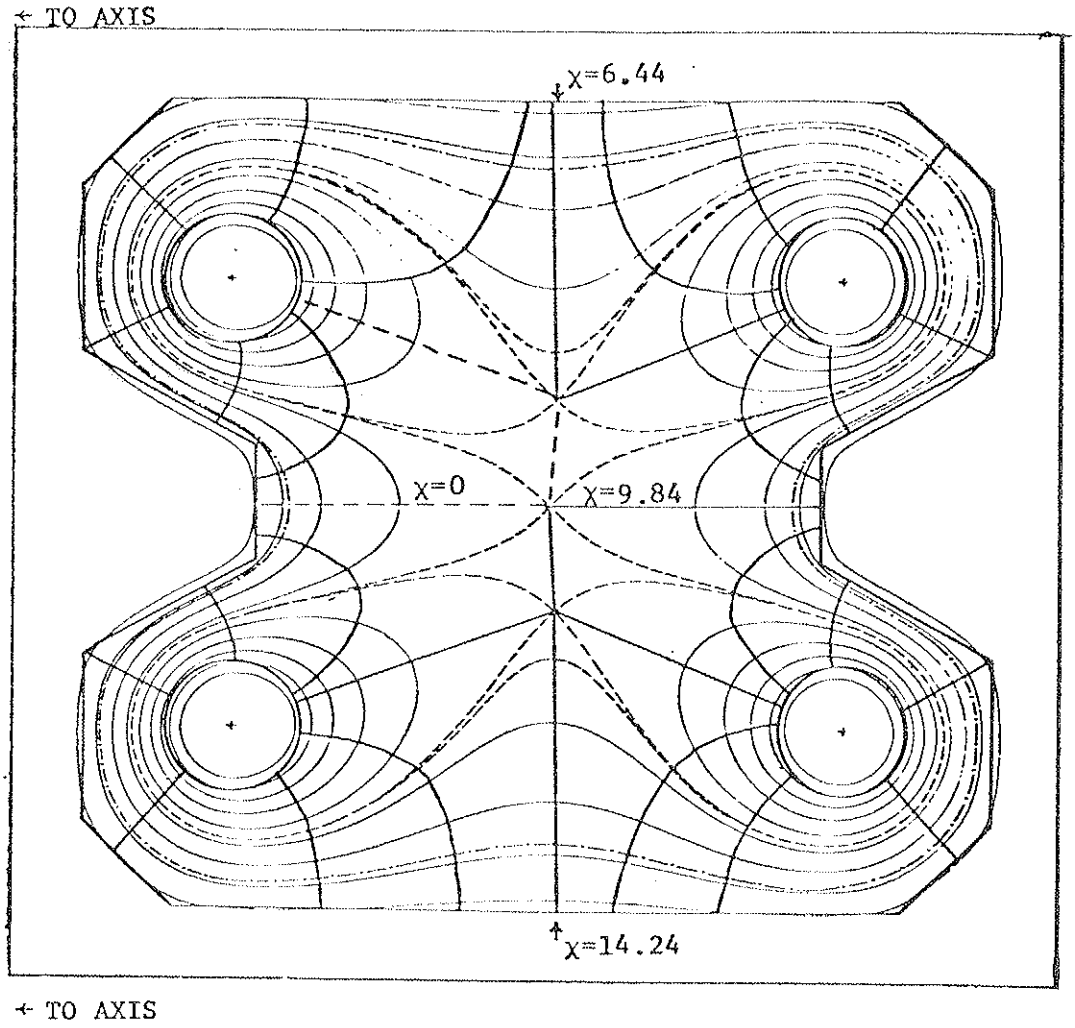

Figure 2.4 - Chi Coordinate System in the Levitated Octupole Superimposed on the flux surfaces of figure 2.3 is a chi coordinate system with the unlabeled lines drawn at arbitrary intervals. χ and Ψ are orthogonal. (See section 2C for discussion.)

References for Chapter 2

1. N. C. Lien, I. N. Sviatoslavsky, "Hoop Levator Design for a Plasma Octupole", University of Wisconsin PLP 275 (1969).

2. E. A. Rose, D. W. Kerst, "Flat Top Field for the Levitated Octupole", University of Wisconsin PLP 849 (1981).

3. R. L. Willig, "Instructions for Using Proogram SOAK", University of Wisconsin PLP 471 (1972).

4. D. C. Morin, "Computed Values of Ψ versus Position for the Levitated Octupole", University of Wisconsin PLP 523 (1973).

5. J. Marshal, "Performance of a Hydromagnetic Plasma Gun", Physics of Fluids 3, 134 (1960).

6. A. G. Kellman, "Performance of Coaxial Gun Plasmas on the Levitated Octupole", University of Wisconsin PLP 859 (1981).

7. D. M. Meade, "Experimnetal Study of Plasma Motion in a Toroidal Octupole Magnetic Field", Ph.D. thesis - University of Wisconsin PLP 51 (1965).

8. G. A. Navratil, "Diffusion Coefficient Scaling in the Wisconsin Levitated Octupole", Ph.D. thesis - University of Wisconsin PLP 693 (1976).

CHAPTER 3 - BASIC DRIFT WAVE THEORY

This chapter presents an introduction to drift waves in slab geometry using kinetic theory. A more extensive kinetic treatment of drift waves in octupole geometry is presented in chapter 6.

A. Single Particle Drifts

In order to address the problem of a drift wave in an inhomogeneous plasma, single particle orbits in the magnetic field must be considered[1]. The motion of a single charged particle is averaged over a gyroperiod to give drift velocities for plasmas with gradients in magnetic field and electric potential. In the fluid model of a drift wave these drift velocities are the unperturbed fluid velocities for the ion and electron species. For the kinetic model the drift velocities are the gyro-averaged trajectories over which an integration over unperturbed orbits is performed. The various drifts are introduced below for later reference.

A1. Electric Field Drifts

ExB drift velocity is the single particle velocity in an electric field $\vec{E}$ perpendicular to the magnetic field $\vec{B}$.

$$\vec{V}_{ExB} = c \frac{\vec{E}x\vec{B}}{B^2} \tag{3.1}$$

where c is the speed of light.

A2. Magnetic Gradient and Curvature Drifts

Magnetic gradient drift velocity is the single particle velocity in a magnetic field with a gradient in a direction perpendicular to the field direction. It has the magnitude of half the thermal velocity of the species times the ratio of the gyroradius to the magnetic field scale length.

$$\vec{V}_{gj} = \frac{\vec{B}x\nabla B}{2B^2} \frac{v_{\perp j}^2}{\Omega_j} \tag{3.2}$$

where $v_{\perp j}$ is the single particle gyrovelocity. Subscript j refers to the plasma particle species.

Magnetic curvature drift velocity is the single particle velocity in a magnetic field which changes its direction. It has the magnitude of half the thermal velocity of the species times the ratio of the gyroradius to the magnetic field's radius of curvature.

$$\vec{V}_{cj} = \frac{\vec{B}x(\vec{B}\cdot\nabla)\vec{B}}{B^3} \frac{v_{\parallel j}^2}{\Omega_j} \tag{3.3}$$

where $v_{\parallel j}$ is the single particle velocity along the field line.

In a current-free region of the plasma, where $\nabla x\vec{B}=0$, equations 3.2 and 3.3 can be combined to give a magnetic gradient and curvature drift velocity

$$\vec{V}_{dj} = \frac{\vec{B}x\nabla B}{B^2} \frac{v_{\parallel j}^2 + v_{\perp j}^2/2}{\Omega_j} \tag{3.4}$$

A3. Diamagnetic Drifts

Another drift velocity, which has validity as a fluid velocity but not as a single particle velocity, is the diamagnetic drift velocity. Diamagnetic drift velocity is the distribution-averaged particle velocity in a plasma having a density gradient. Electrons and ions have fluid velocities that are oppositely directed, resulting in a current which provides a JxB force to balance the pressure gradient caused by the density gradient. The diamagnetic velocity has the magnitude of half the thermal velocity of the species times the ratio of the gyroradius to the density scale length.

$$\vec{V}_{*j} = \frac{\vec{B}x\nabla n}{B\ n} \frac{T_j}{m_j\Omega_j} \tag{3.5}$$

where Ω is the gyrofrequency, B the magnetic field, n the density, m the particle mass, and T the temperature.

B. Drift Waves in a Plasma Slab

In this section the dispersion relation for a drift wave in a plasma slab is investigated. This is a simplification of the more general drift wave dispersion relation generated in chapter 6 using a

linearized kinetic theory. Care is taken in the presentation that follows to identify those terms in the dispersion relation which determine the wave frequency and growth rate, with the intention of giving a physical picture of the drift wave and its growth mechanisms. In particular, attention is paid to the role played by finite ion gyroradius, magnetic gradient drift velocity, and electron Landau damping. It is shown that electron Landau damping with either finite ion gyroradius or magnetic gradient drift is necessary to promote an instability.

For an introduction to kinetic treatment of plasma waves the reader is directed to texts by Krall and Trivelpiece[2] and by Ichimaru[3]. Drift waves are discussed in a review article by Krall[4]; and Chen[5] gives a physical picture of drift waves, discussing the role of finite ion gyroradius.

B1. Plasma Slab Model

Consider the case of an electrostatic drift wave in a plasma slab. In this model, all plasma and magnetic field properties are constant in the θ and χ directions, allowing a (x,y,z) coordinate system to be used in place of the standard (ψ,θ,χ) system, introduced in chapter 2. The equilibrium plasma density n_0 has a gradient, with density decreasing in the x direction. The magnetic field has a gradient in the x direction as well, but no curvature. There is no equilibrium electric field. A wave is assumed to exist with fluctuating values of electric potential ϕ and density n_j, where the subscript j refers to plasma species. The fluctuating quantities

have an assumed spatial and temporal structure $\exp(ik_\perp y + ik_\parallel z - i\omega t)$, with $\omega \ll \Omega_j$. Values for electron and ion temperatures are assumed such that $[T_i/m_i]^{1/2} \ll \omega/k_\parallel \ll [T_e/m_e]^{1/2}$. (This allows us to neglect ion Landau damping, while considering electron Landau damping.) Also, in order that the wave be purely electrostatic;[6] $\omega/k_\parallel \ll C_{Alfven} = B/(4\pi n m_i)^{1/2}$.

Figure 3.1 illustrates the drift wave structure in the slab model for the simple case of cold ions ($T_i=0$) and no magnetic field gradient. This picture of the drift wave is justified in section B3 of this chapter, dealing with stable drift waves.

B2. Dispersion Relation

From equation 7.1 the dispersion relation for the slab case is[7]

$$n_0 \frac{e\phi}{T_e}\left[1 + \frac{\omega-\omega_{*e}}{k_\parallel v_e} Z\left(\frac{\omega-\omega_{de}}{k_\parallel v_e}\right)\right] = -n_0 \frac{e\phi}{T_i}\left[1 + \frac{\omega-\omega_{*i}}{k_\parallel v_i}\beta\, Z\left(\frac{\omega-\omega_{di}}{k_\parallel v_i}\right)\right] \quad (3.6)$$

where $v_{e,i} = (2T_{e,i}/m_{e,i})^{1/2}$, $\beta = I_0(b)\, e^{-b}$ and $b = k_\perp^2 T_i/m_i\Omega_i^2 = k_\perp^2\rho_i^2$, $\omega_{*e} = k_\perp v_{*e}$, and Z is the plasma dispersion function of Fried and Conte.[8] The quantity β is the finite ion gyroradius factor. It is one for $k_\perp\rho_i = 0$ and decreases toward zero with increasing $k_\perp\rho_i$. The plasma dispersion function Z has a simple expansion for large and small arguments

$$Z(\zeta) \cong -2\zeta + i\sqrt{\pi}\, e^{-\zeta^2} \quad \text{for } |\zeta| \ll 1 \quad (3.7)$$

$$\cong -1/\zeta - 1/2\zeta^3 \quad \text{for } |\zeta| \gg 1$$

where the imaginary term for small argument is a Landau damping term. The usual drift wave ordering $k_\parallel v_i \ll \omega, \omega_d \ll k_\parallel v_e$ yields electron Landau damping and negligible ion Landau damping. For the case of equal ion and electron temperatures and no drift frequency (constant magnetic field strength) we obtain a particularly simple dispersion relation

$$n_0 \frac{e\phi}{T}\left[1 + i\sqrt{\pi}\,\frac{\omega - \omega_{*e}}{k_\parallel v_e}\right] = n_0 \frac{e\phi}{T}\left[-1 + \beta + \beta\frac{\omega_{*e}}{\omega}\right] \tag{3.8}$$

Recognizing that the left hand side of equation 3.8 represents the perturbed electron density and the right hand side the perturbed ion density, the terms of the equation can be identified as follows: The term $n_0\, e\phi/T$ on the left hand side of equation 3.8 is the Boltzmann response of the electrons moving along field lines. The second term of the left hand side is the electron Landau damping, resulting from the parallel phase velocity of the wave being resonant with a significant fraction of the electron distribution. For the ions the Landau damping term is absent, due to a small fraction of resonant ions. The ions have a Boltzmann response, $-n_0\, e\phi/T$, with a sizeable correction factor $\beta\, n_0\, e\phi/T$. This correction factor casues a reduction in the ion Boltzmann response due to the large ion mass. The correction term itself is modified by the ion finite gyroradius. In the third term of the right hand side is the effect of ion ExB motion in the electric field of the wave, $\beta\omega_{*e}/\omega$ times $n_0\, e\phi/T$.

B3. Stable Drift Waves

In the limit of zero ion gyroradius (β=1) and no magnetic gradient, the drift wave is stable and has a simple explanation. (This is the case illustrated in figure 3.1.) The electrons respond to the electric potential of the wave with a Boltzmann response $n_e = n_0\, e\phi/T$, and the ions match the perturbed electron density by convection across field lines with an ExB velocity determined by the wave's electric field. The ExB velocity is $ck_\perp\phi/B$, and the ions move in the x direction with frequency ω. Since the ions have a density gradient, the ExB generated displacement causes a change in local density through the continuity equation $\partial n_i/\partial t = -V_{ExB}\, \nabla n_i$. We obtain for the perturbed ion density $n_i = (ck_\perp\phi/B\omega)(dn_0/dx)$ $= n_0(e\phi/T)(\omega_{*e}/\omega)$. The dispersion relation becomes

$$n_0 \frac{e\,\phi}{T} = n_0 \frac{\omega_{*e}}{\omega} \tag{3.9}$$

and it is evident that $\omega = \omega_{*e}$ for this simple case.

The perturbed density and the electric potential of the wave are in phase, as shown in figure 3.1. The electric field drift velocity shown in the diagram causes the density perturbation to propagate in the direction of the electron diamagnetic drift velocity with phase velocity ω_{*e}. With $\omega = \omega_{*e}$, however, there is no contribution to the dispersion relation from the electron Landau damping term of equation 3.8 and consequently the wave is stable.

B4. Instability Mechanisms

B4a. Finite Ion Gyroradius

The coefficient of the Landau damping term suggests that a mechanism which shifts ω from ω_{*e} could cause wave growth by introducing a complex term into the dispersion relation. One such mechanism is finite ion gyroradius[9]. Finite ion gyroradius causes the ions to sample ϕ over their gyro-orbits, performing an averaging of ϕ which reduces the effective potential of the wave to $(1 - k_\perp^2\rho_i^2/2)\phi$[10]. Writing $\omega = \omega_r + i\gamma$ and assuming $\gamma << \omega_r$, the real frequency becomes $\omega_r = \beta\omega_{*e}/(2-\beta)$, which is less than ω_{*e} since $0< \beta <1$ for finite ion gyroradius. Now the Landau term contributes to give a growth rate $\gamma = 2\beta(1-\beta)(2-\beta)^{-3}\sqrt{\pi}\omega_{*e}^2/k_\parallel v_e$, which is positive and has a maximum for $\beta \cong 0.73$, which is $k_\perp\rho_i \cong 0.57$.

B4b. Magnetic Gradients

A similar role of shifting the real frequency from ω_{*e} can be played by the magnetic gradient drift frequency ω_{di}[11]. Neglecting finite ion gyroradius ($\beta=1$), the real frequency becomes $\omega_r = \omega_{*e} + 2\omega_{di}$, the growth rate $\gamma = -2\omega_{di}(\omega_{*e} + \omega_{di})\sqrt{\pi}/k_\parallel v_e$. The growth rate is positive for $-\omega_{*e} < \omega_{di} < 0$, for which $\omega < \omega_{*e}$. The condition $\omega_{di} < 0$ describes bad magnetic curvature, a term introduced in chapter 2, section B1, with reference to MHD stability. Here we see that bad curvature promotes instability for the drift wave in a slab geometry. We also see that instability brought on by magnetic gradients, as well as the finite ion gyroradius induced instability, results in $\omega < \omega_{*e}$.

B4c. General Case

Returning to the general dispersion relation, we can determine ω_r and γ for a slab plasma with electron Landau damping, finite ion gyroradius, gradient drift, and unequal electron and ion temperatures ($\sigma = T_e/T_i$).

$$\omega_r = \frac{\beta\omega_{*e} + (1+\sigma)\omega_{di}}{1 + \sigma(1-\beta)} \tag{3.10}$$

$$\gamma = \frac{\beta(1+\sigma)(\omega_{*e} + \sigma\omega_{di})((1-\beta)\omega_{*e} - \omega_{di})}{(1 + \sigma(1-\beta))^3} \frac{\sqrt{\pi}}{k_\parallel v_e}$$

with the condition for instability $-\omega_{*e}/\sigma < \omega_{di} < (1-\beta)\omega_{*e}$. It is seen that unequal ion and electron temperatures alone cannot cause an instability, but can affect the conditions for instabilities driven by magnetic gradient drift. Figure 3.2 shows graphically the condition on ω_{di} for instability in the slab as a function of β. It is seen that finite ion gyroradius extends the range of ω_{di} for instability to include magnetic configurations with good curvature ($\omega_{di} > 0$). The lower bound on ω_{di} for instability is $\omega_{*i} = -\omega_{*e}/\sigma$.

B5. Wave-Induced Transport

The density perturbation for the general slab case is

$$\frac{n}{n_0} = \frac{e\,\phi}{T}\left[\, 1 + i\sqrt{\pi}\,\frac{\omega - \omega_{*e}}{k_\parallel v_e}\,\right] \tag{3.11}$$

which shows that the density perturbation leads the potential perturbation by an angle $\theta = \sqrt{\pi}\ (\omega - \omega_{*e})/k_{\parallel} v_e$ (in radians) for small angle θ. For $\omega < \omega_{*e}$ this phase angle is positive, negative for $\omega > \omega_{*e}$. As we show below, the sign of the phase angle θ determines whether plasma transport is induced to flow up or down the density gradient, with ramifications for wave growth.

Figure 3.3 illustrates the situation. Shown are graphs of the perturbed density n, the electric potential of the wave ϕ, the ExB velocity induced by the wave v, and the flux nv. These quantities are shown as a function of distance along y for a full wave period for two cases: n and ϕ in phase, and n leading ϕ by 60 degrees.

When the density and potential perturbations are in phase, the ExB velocity and the density perturbation are 90 degrees out of phase. The result is a purely oscillatory density perturbation with no net excursion in the x direction, and thus no net transport. This is the case encountered for the stable drift wave of section B3.

When the density perturbation leads the potential perturbation by 60 degrees, the ExB velocity and the density perturbation are 30 degrees out of phase. The purely oscillatory motion of the previous case is replaced by plasma motion in which, on average, positive density perturbations move toward positive x and negative perturbations move toward negative x.[12] The result is plasma transport down the density gradient, as shown by the predominence of positive nv for this case. This phase relationship is representative of the unstable drift wave of section B4, as we show below.

Expressing the flux as $\Gamma = \langle n\, v_x \rangle_\zeta$, where an average is taken over a wave period,[13] the plasma flux down the density gradient becomes

$$\Gamma = n \frac{\sin(\theta)}{2} \frac{k_\perp \phi}{B} c \qquad (3.12)$$

Examination of equation 3.12 shows that transport down the density gradient takes place for θ positive, which occurs when $\omega < \omega_{*e}$. In the previous section we saw that $\omega < \omega_{*e}$ for the unstable waves caused by finite ion gyroradius or magnetic gradients. Thus these waves are associated with plasma transport down the density gradient, a process which allows the waves to tap the free energy of the density gradient. This ability to tap the plasma's free energy is the physical mechanism behind drift wave instability.[14]

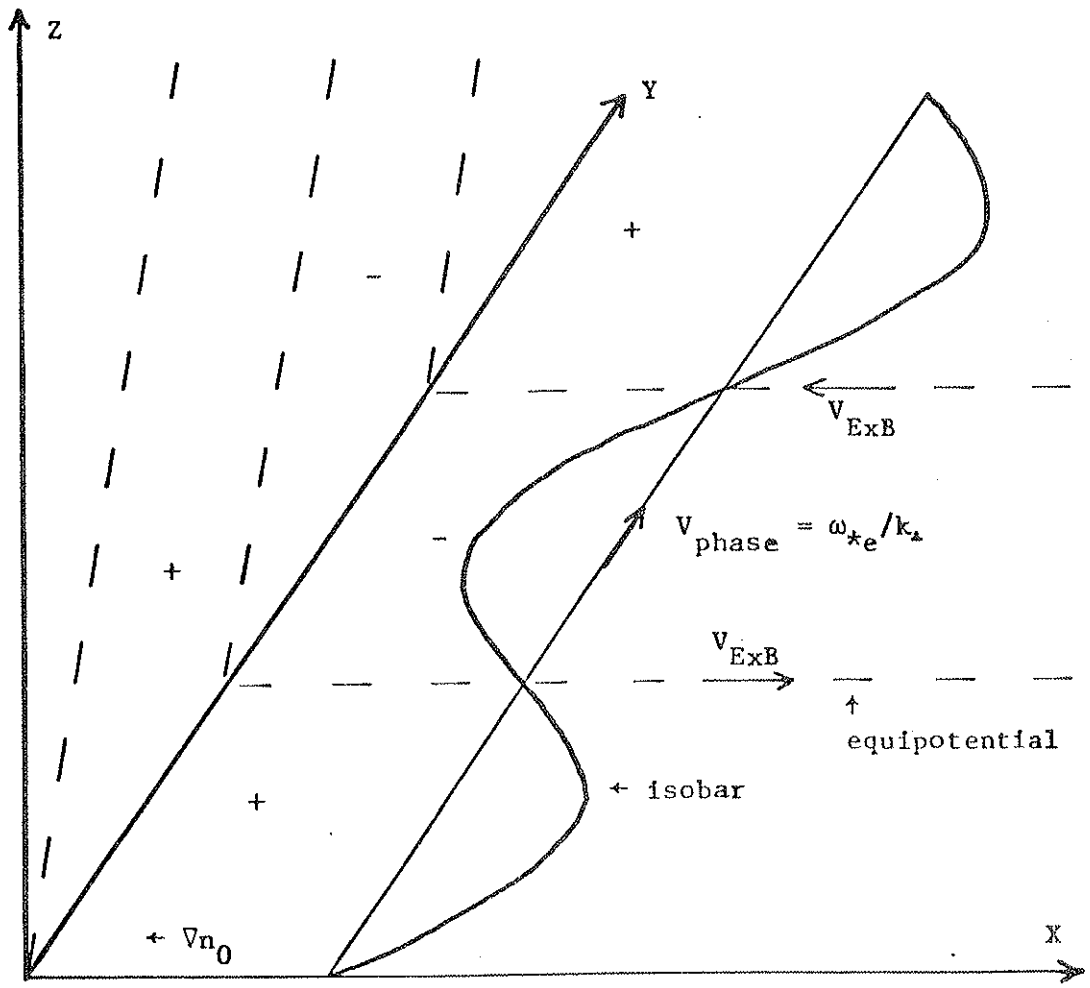

Figure 3.1 – Stable Drift Wave in a Plasma Slab with Density Gradient and No Magnetic Field Gradient

The solid curve is the projection of the constant density surface on the X-Y plane. The dashed lines are the projections of the equipotentials $\phi = 0$ on the X-Y and Y-Z planes. Regions of positive perturbed potential are marked + and negative −. Density decreases with increasing x. Wave phase velocity and ExB drifts are indicated.

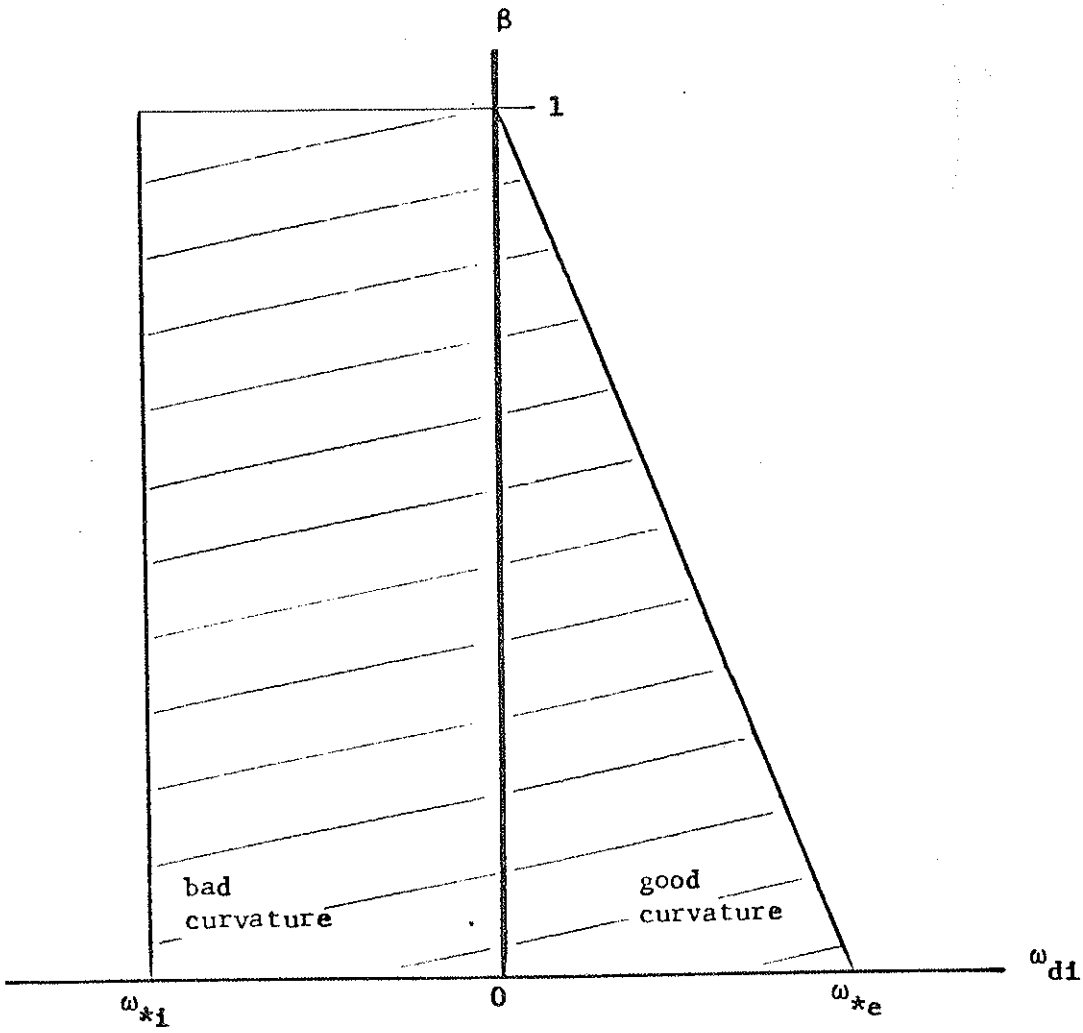

Figure 3.2 - Instability Criteria for a Drift Wave

The shaded region shows the conditions on the ion magnetic gradient drift frequency ω_{di} and the ion gyroradius parameter β to produce an unstable drift wave in plasma slab geometry.

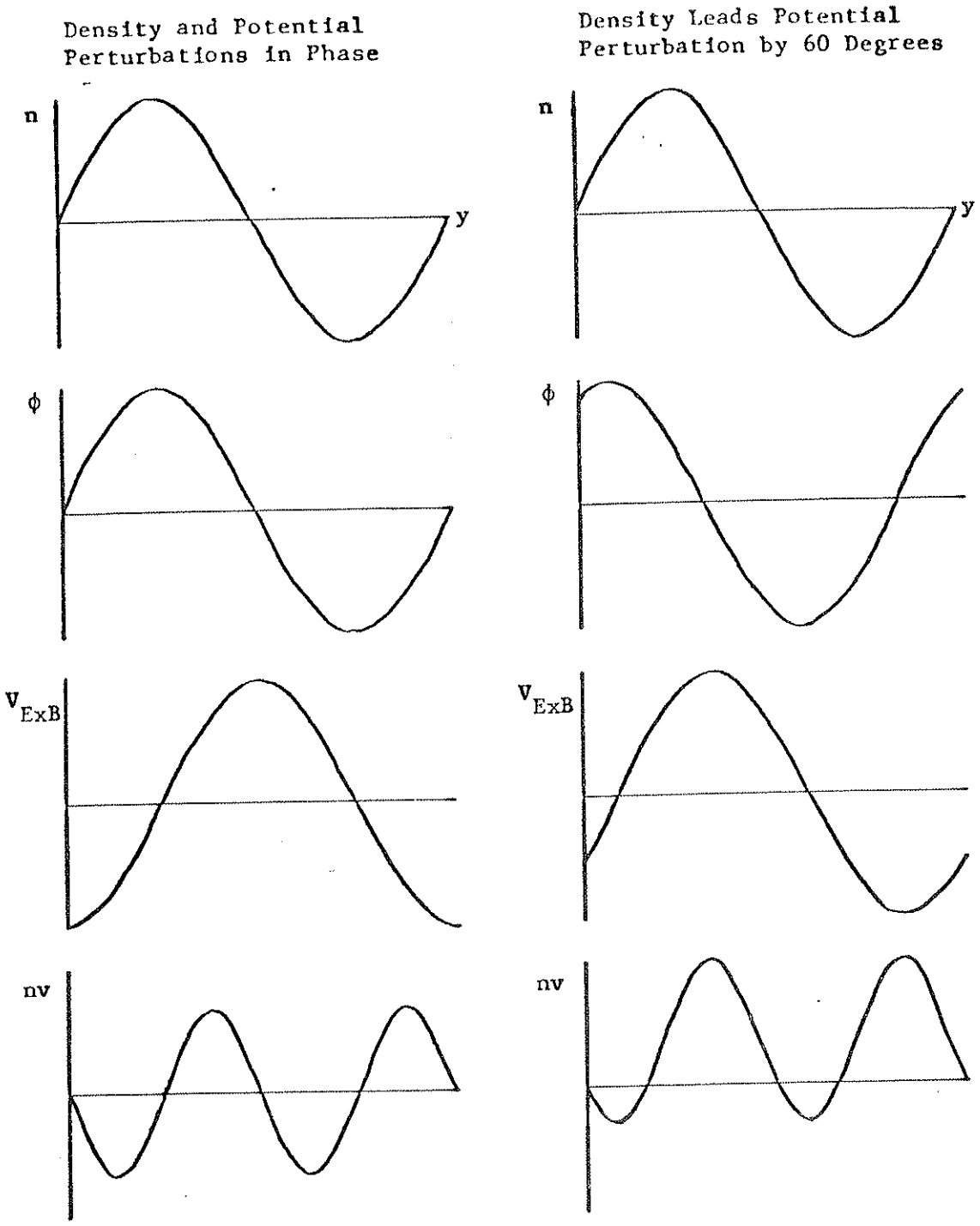

Figure 3.3 - Drift Wave Induced Transport

Flux of the perturbed density down the density gradient is shown (nv) over one wavelength for two cases.

References for Chapter 3

1. L. Spitzer, Jr., Physics of Fully Ionized Plasmas, (John Wiley & Sons, New York, 1962), chapter 1.

2. N. A. Krall and A. W. Trivelpiece, Principles of Plasma Physics, (McGraw-Hill, New York, 1973), chapters 8 and 9.

3. S. Ichimaru, Basic Principles of Plasma Physics, (W. A. Benjamin, Reading, 1973).

4. N. A. Krall, "Drift Waves" in Advances in Plasma Physics, ed. A. Simon and W. B. Thompson, (Interscience, New York, 1968), p. 153.

5. F. F. Chen, "Resistive Overstabilities and Anomalous Diffusion", Physics of Fluids 8, 912 (1965).

6. B. B. Kadomtsev, Plasma Turbulence, (Academic Press, New York, 1965), p. 82.

7. Ibid., p. 85.

8. B. F. Fried and S. Conte, The Plasma Dispersion Function, (Academic Press, New York, 1961).

9. B. B. Kadomtsev, op. cit., p. 86.

10. G. Schmidt, Stevens Institute of Technology Report SIT-131, 1964.

11. S. Yoshikawa, "Low-Frequency Instabilities", in Methods of Experimental Physics, ed. R. H. Lovberg and H. R. Griem, (Academic Press, New York, 1971), volume 9A, chapter 8.

12. F. F. Chen, op. cit., p. 913.

13. B. B. Kadomtsev, op. cit., p. 9.

14. S. Ichimaru, op. cit., p. 142.

CHAPTER 4 - DIAGNOSTICS

A. Mode Structure

A1. Data Acquisition

A program is undertaken to determine the structure of the drift wave in the levitated octupole. Of interest is the mode's frequency, wavelength, and amplitude, as well as its propagation characteristics. Wave structure is determined in three dimensions: radial (psi), toroidal (theta), and poloidal (chi).

Langmuir probes are used for the purpose of investigating the wave. The mode structure is determined by using an array of Langmuir probes, typically three, and comparing the amplitudes and phases of the floating potentials or of the ion saturation currents. Figures 4.1 and 4.2 illustrate the locations of probe ports available for this study. Figure 4.1 shows the poloidal distribution of ports at a position 45 degrees counterclockwise from the poloidal gap. Ports are lettered A through K from the center of the lower lid around the outer wall to above the upper inner ring. Figure 4.2 shows the toroidal distribution of ports from 45 degrees to 55 degrees. The port at 45 degrees is labeled E, and the ports from 46 to 55 degrees are labeled L, M, and N. In addition to these ports, there are probe ports at other toroidal locations, which are useful for checking that the wave properties are uniform throughout the octupole.

Data is quantified with oscilloscopes and with waveform digitizers in conjunction with a digital computer. Changes in bulk

plasma properties, such as density and temperature, are characterized by millisecond time scales, while the frequencies of the waves are in the range 10 KHz to 100 KHz.

Figure 4.3 shows schematically the steps taken to electronically acquire and process the data. A data signal from a Langmuir probe is sent to a nearby Tektronix AM-502 amplifier, serving as amplifier, frequency filter, and line driver. The signal is then digitized using a Le Croy 8102 Hex Attenuator and a Le Croy 2256 Waveform Analyzer. A Digital Equipment Corporation PDP 11/20 computer is used to analyze the stored data and to produce displays. Data can be displayed via cathode ray tube or x-y recorder, printed on a teletype, or saved on floppy disk, magnetic tape, or paper tape. Figure 4.4 shows some wave forms taken with this method.

A2. Data Analysis

In this section we discuss the methods used to determine the frequency, wavelength, and phase shifts from the data stored in the computer. At the heart of the routines used to do this are several assembly language subroutines: CORLAT, FULCOR, and FFT! These subroutines allow the Basic program to analyze the data in the time between shots, typically one and a half minutes.

The sequence used to analyze the data is first to take a correlation of the data and then to take the fast Fourier transform of the correlation function. The correlation function preserves the common frequency components of the two data signals while reducing the noise level. It also provides an indication of propagation time for a wave

train from one probe to another. The complex fast Fourier transform of the correlation function yields the wave frequency, wavelength, and phase shift between two probes.

A2a. Correlation Function

A short description of the correlation function and its utility is given below. The interested reader is referred to the excellent account of the correlation function given by C. J. Armentrout.[2]

Introduction to Correlation Function

The correlation function C(t) is defined for complex valued functions A and B as the product of the complex conjugate A*(s) and B(s+t), integrated over s from zero to T. An autocorrelation has A = B, while a cross correlation has A and B distinct.

$$\text{Autocorrelation} \qquad C(t) = \frac{1}{T}\int ds\ A^*(s)\ A(s+t) \tag{4.1}$$

$$\text{Cross Correlation} \qquad C(t) = \frac{1}{T}\int ds\ A^*(s)\ B(s+t) \tag{4.2}$$

Decomposition of two functions A and B into their Fourier components, followed by a cross correlation, reveals that the cross correlation preserves common frequency components and eliminates components peculiar to a single function. Furthermore, the phase of a Fourier component of the cross correlation is the difference between the phases of that Fourier component in functions A and B.

$$C(t) = \frac{1}{T}\int ds\ \sum_j A_j \exp(i\omega_j s + i\phi_j)\ \sum_k B_k \exp(-i\omega_k(s+t) - i\theta_k) \tag{4.3}$$

$$= \sum_k A_k B_k \exp(-i\omega_k t + i\phi_k - i\theta_k)$$

Note that a Fourier coefficient of function B is the correlation function element C(0) when A is a sinusoidal wave. Also, the Fourier transform of the autocorrelation is the power spectrum.

Another useful property of the correlation function is the improvement of the signal to noise ratio it provides[2]. Consider a function A(t) + N(t), where a random noise function N(t) is superimposed on an organized signal A(t). In the autocorrelation function C(t), the cross terms of the form A*N will average out to zero. Likewise, for $t \neq 0$, the N*N terms will also average out. But at $t = 0$ the N*N terms will all be of the same sign and will add to produce a noise "spike" on what is essentially the autocorrelation of function A. As a generalization of this result, if two functions share a noise pattern, separated in time by t_0, a noise spike will show up in the cross correlation element $C(t_0)$.

Use of the Correlation Function

In the previous section it was shown that the correlation function improves the signal to noise ratio of the common frequency components of two signals. Further, the noise spike gives an indication of the time delay between signals. In the discussion below, attention is drawn to some of the complications presented by real data and the methods used to obtain correlation functions which are as close to ideal as possible.

Ideal data signals consist of an infinitely recurring periodic pattern with few Fourier components. In reality, the data are taken over a finite period of time and have a tendency to change frequency components during the sampling period. One must attempt to take the data in such a way as to approximate as nearly as possible the ideal.

In general, one wants a large data sample to average out the random noise. In addition it is necessary to have a data signal with a large number of oscillations to get accurate values for the amplitude and phase of the correlation function. This problem with amplitude and phase is addressed below, where we consider the case of two sine waves of frequency ω and phases ϕ_1 and ϕ_2:

$$C(t) = \frac{1}{T}\int ds\ A_1\cos(\omega s + \phi_1)\ A_2\cos(\omega s + \omega t + \phi_2) \qquad (4.4)$$

$$= \frac{A_1A_2}{2}\left(1 + \frac{2\ \sin\omega T}{\omega T}\cos\theta + \frac{\sin^2\omega T}{\omega^2T^2}\right)^{1/2}\cos(\omega t + \phi_1 - \phi_2 + \zeta)$$

where $\theta = 2\phi_1 + \omega T$ and $\zeta \cong \sin(2\phi_1 + \omega T)\ \sin(\omega T)/\omega T$ for large ωT. For an unbounded integration interval ($T\to\infty$, the ideal case) $C(t) = A_1A_2\cos(\omega t + \phi 2 - \phi 1)/2$. The descrepancy between the ideal case and the results of equation 4.4 comes when T is not an integral number of wave periods long, which is the general case. Then the amplitude and the phase of the correlation function both have error terms that vary as $\sin(\omega T)/\omega T$. By integrating over many wave periods, however, ωT can be made large and the errors reduced. The error in amplitude should be small to retain the relative amplitudes of the various fre-

quency components of the signals. The error in phase should be small to accurately judge the phase difference between signals to get accurate values for wavelength. Thus one would like to have a large number of oscillations in the data interval to get an accurate correlation function.

On the other hand, if the frequency is slowly changing the data time interval should be short for the data at late times to be consistent with the data at early times. In addition, there are only 254 usable points available in the digitized sample interval, and the more oscillations one has, the less phase information is available. In practice a balance must be struck when choosing a data window size, and in the experiment six to twelve oscillations per data window are found optimal.

A few comments about the use of the noise spike in the data analysis are in order. The correlation function of two data signals which are pure sine waves has an ambiguity in phase of an integral multiple of two pi. However, individual oscillations in a wave train tend to be of different sizes or have slightly different shapes. As the wave train propagates around the octupole, it retains these characteristic features to some degree. A correlation function of data signals from two probe ports will indicate these shared characteristics by a noise peak at t_0, the propagation time of the wave train, removing the phase ambiguity. Another method of removing the phase ambiguity is to use three probes and to look for a

consistent phase velocity, but the noise spike method is reliable and particularly simple for use in a computer program.

An example of the cross correlation function of two data signals is shown in figure 4.5.

Subroutines CORLAT and FULCOR

The routine used to perform the correlations is CORLAT, an assembly language subroutine that can be called from a program written in Basic. This routine asks for the two functions to be correlated and a window size for the integration. It returns the correlation function.

Since the data is discrete and finite, the integration takes the form of a summation of products: $C(t) = \sum_s A(s)\ B(s+t)/N$, where s varies over the indices of data in the integration window (N points) and s+t must be within the range of indices of the data interval. This method can be wasteful of the data, however, since the number of points in the data interval is the sum of the integration window size and the number of values of t. Thus a large integration window results in a small range for t and vice versa. Further, the data functions A and B are not treated in a symmetric fashion, and only a limited range of data function A is ever used.

A solution to the problem above is illustrated in Figure 4.6 and implemented in the assembly language subroutine FULCOR. A zero buffer is added to either side of the non-zero data, and the full non-zero data interval is used as the integration window. The example is for a data interval of 254 points. One now uses the total

data intervals of functions A and B to the fullest extent and in a symmetric fashion. A form factor S(t) must be used to normalize the data, since the extent of the non-zero integrand varies. A correlation function is generated with 257 points.

$$C(t) = \sum_s A(128 + s)\ B(128 + s + t)\ S(t) \tag{4.5}$$

where $S(t) = (254 - \text{abs}(t))^{-1}$.

A2b. Fast Fourier Transform

A short description of the fast Fourier transform (FFT) and its utility is given below. An extensive treatment of FFT theory and application is given in the book by E. Oran Brigham[3].

Introduction to Fast Fourier Transform

The fast Fourier transform is an algorithm for computing the Fourier series ($\sum_k A_k \exp(-i\omega_k t)$, where A_k is complex-valued) using discrete data. A very rapid computation is possible when the number of points is a power of two. In this experiment 256 points from the correlation function discussed above are analyzed.

The complex-valued coefficients of the Fourier series over a period T are $A_k = \frac{1}{T}\int dt\ \exp(i\omega_k t)\ C(t)$. The finite period of integration leads to the requirement that ω_k be of the form $2\pi n/T$, where n is an integer. A purely sinusoidal signal may fall between two frequencies of the discrete spectrum. Then the Fourier series will return high amplitudes for the closest frequency components in its allowed spectrum, complicating the analysis somewhat. A further

consequence of having a wave outside the discrete Fourier spectrum is that, viewed as a periodic function, it has a sharp jump discontinuity from the end of the data interval to the start of the data interval. In its attempt to fit this pattern the Fourier series generates high frequency components, a process known as leakage. Leakage does not interfere with data analysis for this experiment, however.

As mentioned previously, the FFT is distinguished from the Fourier series in being applied to discrete data, that is, data having a finite number of points. The integral above becomes a summation.

$$A_k = \frac{1}{T}\sum_t \exp(i\omega_k t)\ C(t) \qquad (4.6)$$

One effect of the discrete data is to limit the frequency bandwidth of the FFT to a range of zero to N/2T, with frequency step size of 1/T. That N/2T is the highest frequency is easily seen, since two points (a high point and a low point) are the fewest number of points capable of defining an oscillation. If one were to digitize a higher frequency signal that N/2T the FFT would interpret this as a lower frequency, modulo N/2T (e.g. (2N+6)/2T becomes 6/2T). This process, known as aliasing, is easily avoided by making the sampling interval much smaller than the period of the wave.

Let us return for a moment to the earlier discussion of the number of oscillations in a data window, taken up in the section

dealing with the correlation function. We see that for accurate frequency determination the FFT requires T/N to be large. However, the smallest phase difference that can be measured is $\omega T/N$, so that for accurate phase determination, a small T/N is desirable. As was the case for the correlation function, a compromise must be made in the number of oscillations ωT in the data window.

Use of the Fast Fourier Transform

The function analyzed with the FFT is the correlation function, discussed above. The data are in the form of a low noise sinusoidal function, with a peak amplitude at the time t_0 corresponding to the time of propagation of the wave train. The FFT is used to find the frequency of the wave train and also its velocity and wavelength from the phase shift indicated by t_0.

The frequency of the wave train is found using the power spectrum of the FFT, which is $\|A_k\|^2$. Cases for which one component dominates the power spectrum are the simplest to analyze, for they comprise the cases for which the wave train is sinusoidal with one of the FFT's discrete spectral components. From the complex amplitude of a frequency component, a phase for the component can be found for any point of the correlation function. The phase of interest is the difference between the phase of the amplitude peak at time t_0 and the phase at time zero. Actually, the peak at t_0 is a group propagation time for the common pattern of the wave train. Since we are interested in the propagation time for one component A_k, we find the time closest to t_0 for which $A_k \exp(-i\omega_k t)=1$ and determine a phase.

The phase difference and the distance of separation of the two probes yields the wavelength, and the wavelength with the frequency yields the phase velocity.

Subroutine FFT

The routine used to perform the fast Fourier transform is FFT, an assembly language program callable from a Basic program. This routine asks for a function to be analyzed (the correlation function), data length (256), and type of analysis. It returns either a complex Fourier series or a power spectrum, depending on the type of analysis specified.

B. General Plasma Diagnostics

Following is a short description of the diagnostics used to quantify general plasma properties, such as density, floating potential, and ion and electron temperature.

B1. Langmuir Probes

Langmuir probes are used to find local density, floating potential, and electron temperatures. A short paper by Chen[4] discusses the use of Langmuir probes and contains the equations presented in this section.

Density measurements can be made by biasing a probe into the ion saturation region of the characteristic I-V curve.

$$I_{si} = \frac{neA^*}{4}\langle V_i \rangle \tag{4.7}$$

The probe repells all electrons and collects all ions over the effective probe area A*. The ions drift into the probe collection area with their thermal velocity, creating a flux $n\langle V_i\rangle/4$. The ion saturation current is dependent on the effective area and ion thermal speed, which are not accurately determined. Therefore, the Langmuir probe is used to give relative local densities and is calibrated with the microwave interferometer descussed below. In practice -45 volts bias on the Langmuir probe is used to find ion saturation current. Experiments using -90 volts show no significant deviations from the -45 volt data.

Floating potential is found with a Langmuir probe having a 10 MΩ impedance to ground. For gun plasmas, where T_i greater than T_e is the rule, the relationship between the floating potential V_f and the plasma potential V_p is given by

$$V_p - V_f = \frac{T_e}{e} \ln\left[\frac{\langle V_e\rangle}{\langle V_i\rangle}\right] \cong 3.5 \frac{T_e}{e} \quad \text{for } T_e = \frac{T_i}{2} \tag{4.8}$$

Typical measured floating potential gradients are one volt per centimeter, so that an electron temperature gradient of 0.3 volt/cm, out of a typical electron temperature of about ten volts, would equal the measured floating potential gradient. Thus substituting floating potential gradients for plasma potential gradients is not an accurate method of finding electric fields in these plasmas, although other

authors do use floating potential gradients to deduce electric fields[5].

Electron temperatures are found using the current-voltage curves of Langmuir single-tipped and double-tipped probes and assuming a Maxwellian velocity distribution. For a single-tipped probe in the transition region the relationship between bias voltage V and current drawn to the probe I is

$$\frac{d\ \ln I}{dV} = \frac{e}{T_e} \tag{4.9}$$

while for a double probe in the transition region the relationship is

$$I \cong \tanh(eV/2T_e) \tag{4.10}$$

B2. Microwave Interferometers

Two microwave interferometers are available for measuring plasma density. Each transmits microwaves through the midcylinder of the octupole, the region in which the separatrix dominates and in which the peak density of gun-produced plasmas is found.

A Fabry-Perot interferometer[6] measures low plasma densities (5×10^{8}/cc to 1×10^{11}/cc peak density. The interferometer consists of a high Q (3.5×10^{4}) microwave Fabry-Perot etalon operating with small frequency excursions about 35 GHz. Introduction of a plasma between the mirrors of the device changes the resonant frequency, which is

electronically detected, and gives a measure of the peak plasma density.

A 35 GHz fringe shift microwave interferometer measures high plasma densities (to 1.5×10^{13}/cc). Comparison between phases of microwaves taking a path through the plasma and those in a reference arm yield a measure of the plasma density in terms of 180 degree phase shifts (fringes).

B3. Ion Energy Analyzer

Several versions of an electrostatic ion energy analyzer are used. Figure 4.7 illustrates the construction and usage of one of these probes. The probe operates by having a first grid at floating potential, behind which is a second grid negatively biased to exclude all electrons. A collector is biased to various positive potentials, yielding the ion temperature by the relationship $d \ln I/dV = e/T_i$. An alternate method of operation is to insulate the first grid from the probe case and bias it to exclude the electrons. The second grid is used as a secondary electron suppressor.

Another form of ion energy analyzer, called a skimmer probe[7], excludes electrons from its interior by utilizing the electron's small gyroradius in a magnetic field. It is built as a thin wafer and operated with the magnetic field parallel to the plane of the collector. Ions have a large enough gyroradius to enter the probe and impinge on the collector, while electrons are prohibited from entering due to their much smaller gyroradius. Biasing the collector and measuring the I-V characteristic yields the ion temperature.

Data from both versions of the energy analyzer are used in this experiment.

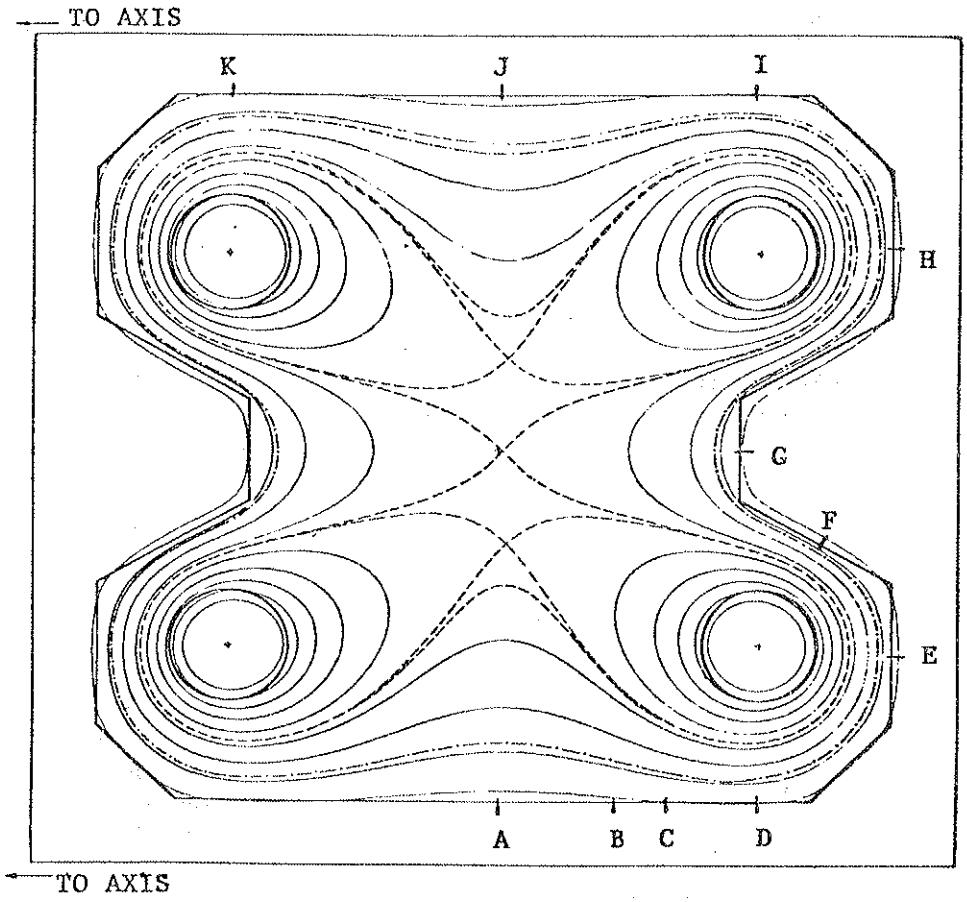

Figure 4.1 - Poloidal Positions of Probe Ports at a Location 45 Degrees from the Poloidal Gap

Figure 4.2 - Toroidal Positions of Probe Ports

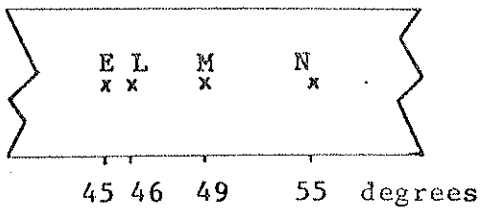

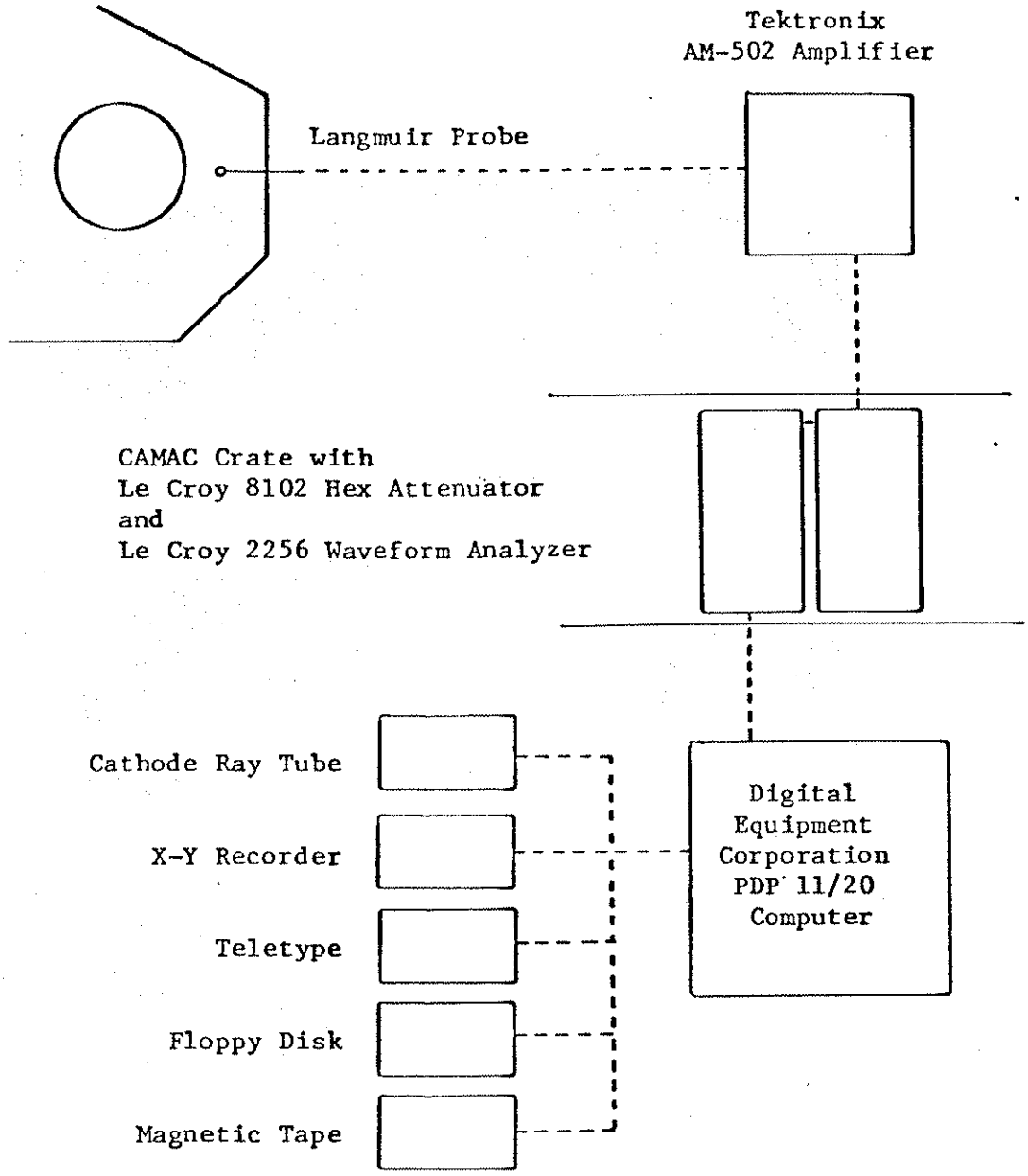

Figure 4.3 - Schematic of Data Acquisition System

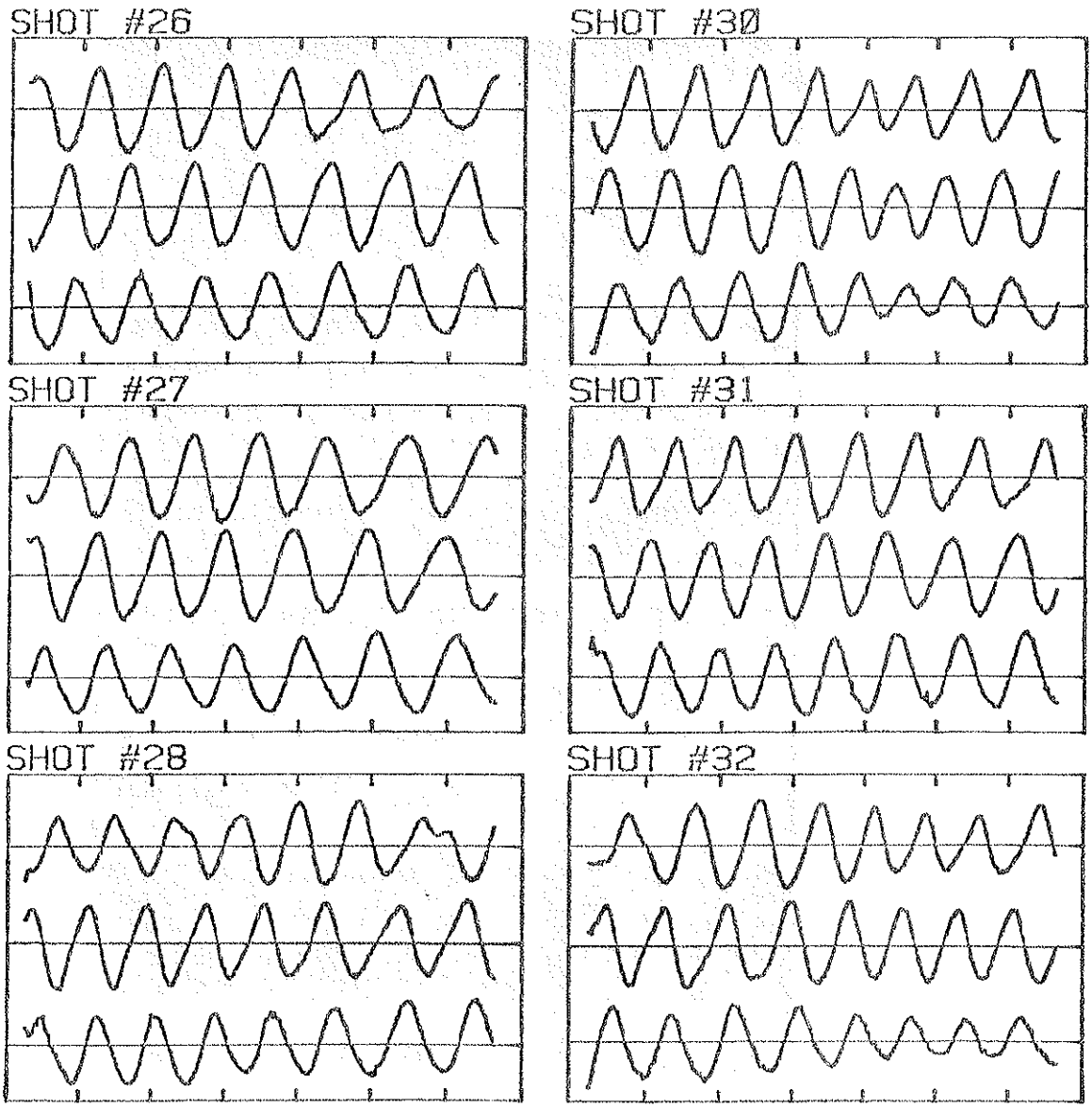

Figure 4.4 - Sample Waveforms

The waveforms above are ion saturation fluctuations (~30 kHz) taken with the data acquisition system of figure 4.3. Langmuir probes are positioned at probe ports E, H, and J (swivel port).

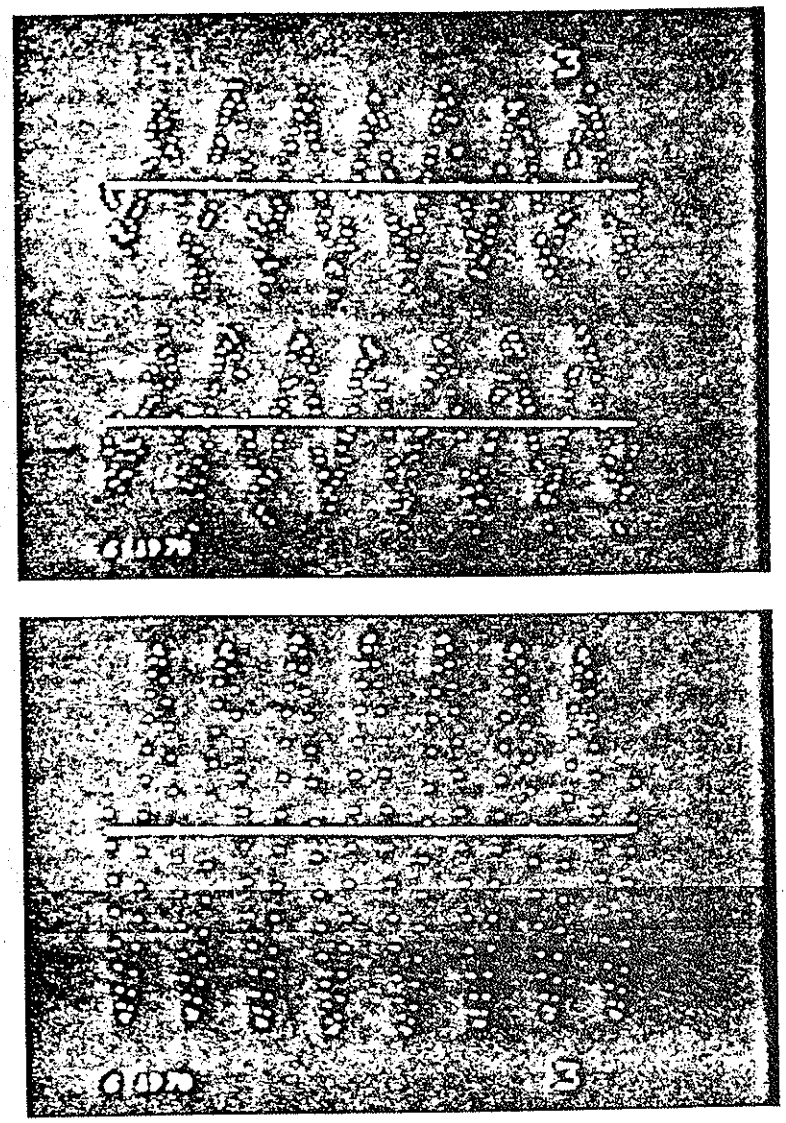

1 μsec/point

Figure 4.5 - Correlation Function of Two Data Signals

The top two pictures show ion saturation fluctuations which have been digitized. The bottom picture shows their cross correlation. The signal to noise ratio is greatly increased. The central peak is the largest, indicating no phase shift between signals.

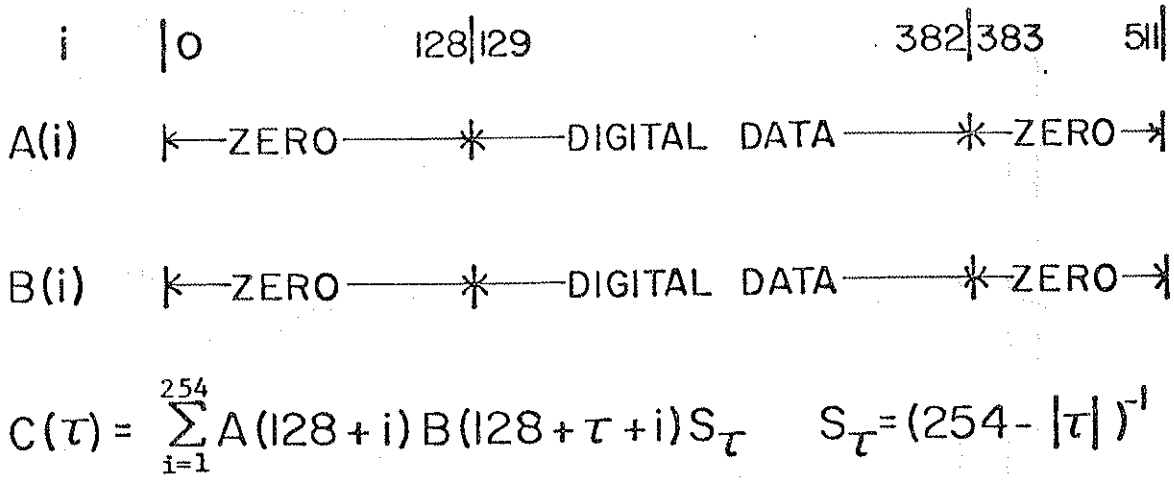

Figure 4.6 - Efficient Use of a Finite Data Interval in the Calculation of the Correlation Function

There are 254 data points in the data interval, with a zero buffer of 129 points added before and after. The normalization function S_τ is used to correct for the difference in the number of non-zero products that make up $C(\tau)$, where $-129 < \tau < 129$.

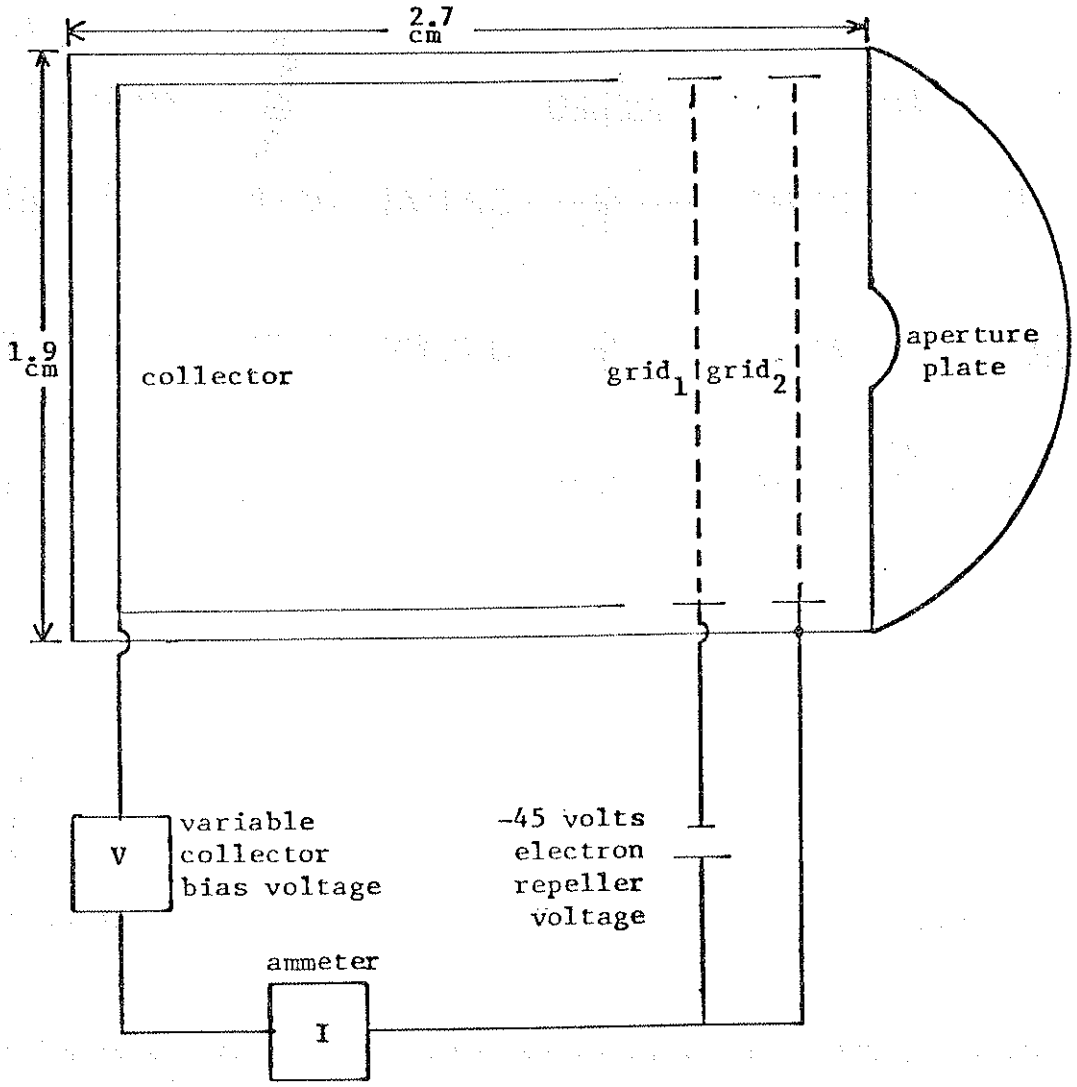

Figure 4.7 - Electrostatic Ion Energy Analyzer

Plasma enters the analyzer through the aperture plate and $grid_2$. $Grid_1$ excludes the electrons, while the collector accepts ions with energy greater than V times charge. The ammeter records the collected ion current.

References for Chapter 4

1. E. A. Rose, "Rebel Subroutines: Computations", University of Wisconsin PLP 759a, 1980.

2. C. J. Armentrout, "A Note on the Correlation Function: Subroutine CORLAT", University of Wisconsin PLP 480, 1974.

3. E. O. Brigham, The Fast Fourier Transform, (Prentice-Hall, Englewood Cliffs, 1974).

4. F. F. Chen, "Electric Probes", in Plasma Diagnostic Techniques, ed. R. H. Huddlestone and S. L. Leonard, (Academic Press, New York, 1965), p. 113.

5. J. R. Drake, "Observations of Plasma Density and Potential Sturcture in a Toroidal Octupole Magnetic Field", Ph.D. Thesis, University of Wisconsin PLP 549, 1973.

6. R. J. Chaffin, "Application of the Microwave Fabry-Perot Resonator to Plasma Diagnostics", Ph.D. Thesis, University of Wisconsin PLP 138, 1967.

7. D. A. Brouchous, "Plasma Resistivity Measurements in the Wisconsin Levitated Octupole", Ph.D. Thesis, DOE/ET53051/13, 1980.

CHAPTER 5 - EXPERIMENTAL RESULTS

This chapter presents the results of observations on the drift wave in the levitated octupole. The wave is observed as an extremely coherent oscillation in the ion saturation current and floating potential, as detected by Langmuir probes. This coherence of the wave makes it an ideal subject for study using the methods of chapter 4. The frequencies and wavelengths are all obtained using the correlation and fast Fourier techniques, as are the poloidal, toroidal, and radial structures.

The wave properties are characterized in table 5.1. Briefly, the wave has a frequency of about 30 kHz and a toroidal mode number of 60 (20 cm wavelength in the outer bridge). The wave amplitude is maximal in the bad curvature regions of the octupole and has an odd poloidal symmetry. The wave is seen over a broad range of plasma densities (10^9/cc to mid-10^{12}/cc), but is restricted to the regime of low magnetic field strengths, due to ion gyroradius considerations. The addition of toroidal magnetic field stabilizes the wave. Although the wave is of large amplitude, typically $\delta n/n_0$ = 20-30%, its effect on plasma transport is negligible.

In section A the experimental observations are presented in detail, viewed in light of the simple drift wave theory of chapter 3. In section B a comparison is made with similar observations from a linear quadrupole.

A. Wave Properties

A1. Radial Structure

The wave structure in the radial (Ψ) direction is that of a standing wave. A Langmuir probe with three tips spaced one centimeter apart is used to sample three radial positions at once, verifying that there is no phase shift in the radial direction. However, there is a marked difference in wave amplitude across psi surfaces.

Figure 5.1 shows a scan across the lower outer bridge region of the octupole. It is seen that the ratio of the density fluctuation amplitude (half of the peak-to-peak value) to the background density increases monotonically from the ring to the wall and that the absolute fluctuation amplitude is a maximum at about seven centimeters from the ring. In the bridge region the separatrix (at about 5 cm from the ring) divides a region of good magnetic curvature close to the ring from a region of locally bad magnetic curvature close to the wall. It is seen from the figure that the wave has its largest amplitude in the region of large density gradient and locally bad magnetic curvature. (Refer to figure 5.2.)

A2. Poloidal Structure

The wave structure in the poloidal (χ) direction is that of a standing wave. Langmuir probes are positioned at various points along a field line and the phases and amplitudes of the fluctuations are compared. Wave amplitude is maximized in the bridge regions of the octupole, and minimized in the nose and lid regions. Figure 5.3

illustrates this poloidal structure. Nodes are located in the noses and lids, while antinodes are located in the bridges. Across each nose or lid there is a 180 degree phase shift, so that in following a field line around the octupole a 720 degree total phase shift is encountered. Figure 5.4 illustrates the 180 degree phase shift between density fluctuations as seen at probe ports E and H.

The electric potential fluctuations associated with the wave show the same structure as described above for the density fluctuations. In going through a nose or a lid region the wave potential is observed to change sign, giving this structure the designation "odd poloidal symmetry".

The value of $k_\parallel$ indicated by this poloidal structure is 2π divided by L_c = 225 centimeters, the distance half way around the octupole along a field line. For a 10 eV plasma this yields $k_\parallel V_e/2\pi$ = 800 kHz and $k_\parallel V_i/2\pi$ = 20 kHz. Since the wave frequency $\omega/2\pi$ is 30 kHz, this gives an ordering ($k_\parallel V_e \gg \omega \gtrsim k_\parallel V_i$). This ordering gives electron Landau damping, but ω is close enough to $k_\parallel V_i$ to indicate ion Landau damping. However, there is some uncertainty in the exact value of ω as discussed in the next section. Let us assume that the plasma frame frequency is actually closer to the diamagnetic frequency, as predicted by the simple drift wave theory. Substituting the diamagnetic frequency $\omega_{*e}/2\pi$ (70 kHz) for ω, the condition of section 3B1 ($k_\parallel V_e \gg \omega \gg k_\parallel V_i$) is recovered and ion Landau damping is avoided.

The wave is seen to have its maximal amplitude poloidally in regions of locally bad magnetic curvature, just as the wave is seen to peak radially in bad curvature. (Refer to figure 5.2.)

A3. Toroidal Structure

The wave structure in the toroidal (θ) direction is that of a propagating wave. Langmuir probes positioned toroidally about the octupole indicate that the wave amplitude is independent of toroidal position and that the wave propagates in the direction of V_{*e}, the electron diamagnetic drift velocity. For the octupole, this is in the clockwise direction, when viewed from above. A typical toroidal wavelength is 20 centimeters, and the wave propagates at somewhat less than V_{*e} in the laboratory frame.

There is some uncertainty in the phase velocity of the wave in the plasma frame arising from the difficulty of arriving at an accurate value for the plasma potential gradient. (This problem is discussed in section 4B1.) If the floating potential gradient is used to calculate the ExB velocity of the plasma, the plasma is found to be moving in the V_{*e} direction. If this indication were accurate, we would have the situation of figures 5.5 and 5.6.

Figure 5.5 shows the floating potential profile for the common flux at probe port E. Note that the electric field is toward the ring, causing V_{ExB} to be in the V_{*e} direction. In figure 5.6 the phase velocity of the wave is plotted along with the ExB velocity indicated by the floating potential. For the position chosen, 7.5 centimeters from the ring, the two velocities are remarkably close,

with the ExB velocity being larger. However, a small gradient in T_e (less than .5 eV/cm, with T_e larger on the separatrix than at the wall) could account for the whole of the measured floating potential gradient, indicating no ExB drift velocity.

Also note that there is essentially no potential gradient from 4.0 to 6.0 centimeters from the ring, yet the wave is still found in this region with the same wavelength and phase velocity. Drake[1], faced with a similar situation in a different experiment, concluded that two modes were present. In this case, however, there is no variation in wave properties across the common flux region, save for the difference in V_{ExB} calculated on the basis of floating potential. There is only one mode in this experiment, and it is treated from this point onward as if its frequency in the laboratory and plasma frames of reference were the same.

A4. Density Dependence

The wave structure remains unchanged for plasmas with densities from $1x10^9$/cc to $2x10^{12}$/cc. The wave's relative amplitude ($\delta n/n_0$) is also relatively unchanged, as shown in figure 5.7. (It should be noted that the cases represented in figure 5.7 are optimized for fluctuation amplitude.) From the drift wave theory of chapter 3, we see that the characteristic plasma drift velocities V_* and V_d are density independent, so that the density independence of the wave is not surprising from this viewpoint.

Increasing density does provide for greater collisionality, however. The collision frequencies may be expressed as[2]

$$\nu_e = 2.9\times10^{-6}\ n\ \ln\Lambda\ T_e^{-3/2} \qquad (5.1)$$

$$\nu_i = 4.8\times10^{-8}\ n\ \ln\Lambda\ T_i^{-3/2}$$

$$\nu_{Nj} = 4.9\times10^{-9}\ N\ (T_j/m_j)^{1/2}$$

where n is plasma density, N is neutral density, and $\ln\Lambda$ is the Coulomb logarithm. Temperatures are in eV, densities in cm^{-3}, and mass in terms of the proton mass.

For a 1×10^{11}/cc density plasma with a temperature of 10 eV and a background neutral density of 1×10^{-6} torr, the ions are collisionless (ν_i = 3 kHz) and the electrons are collisional (ν_e = 160 kHz) with respect to the wave frequency of 30 kHz. Dropping the density to the 10^9/cc range with neutral density less than 5×10^{-7} torr makes both the ions and electrons collisionless, while raising the density to the 10^{12}/cc range makes both the electrons and ions collisional. Thus the wave is seen over a wide range of ion and electron collisionality, although at the high density end of the range the waves are not quite so coherent as at the low densities.

The magnetic field structure between the bad magnetic curvature regions of figure 5.2 is that of a magnetic mirror. Plasma particles with large values of $v_\perp/v_\parallel$ are confined in the low field strength region of these mirrors, executing trapped particle motion.[3] Those ions trapped in the mirror cell by probe port G have a bounce frequency of approximately 30 kHz for 10 eV ions, and the fraction of

trapped ions is 70 - 90%, depending on radial position. However, at plasma densities greater than $1x10^{12}$/cc the ions cannot execute a complete bounce before suffering a collision. Since the drift wave is observed at densities greater than $1x10^{12}$/cc, the importance of trapped ions for the observed mode is in doubt. (A similar statement holds for electrons, which become detrapped at plasma densities greater than $8x10^{11}$/cc.)

Figure 5.8 shows the effect of increasing the background neutral density of a low-10^9/cc density plasma from less than $1x10^{-6}$ torr to $7x10^{-6}$ torr. The fluctuations are quenched by the neutrals, presumably through charge exchange cooling of the ions[4].

A5. Ion Gyroradius Dependence

Four pieces of evidence are presented below to show that the wave amplitude depends on the ion gyroradius size:

1. The wave amplitude depends on the poloidal magnetic field strength for a wide range of densities.

2. The time of onset of the wave depends on the poloidal magnetic field strength.

3. The length of time that the wave is present depends on the ion temperature cooling time.

4. The toroidal wavelength increases with time as the ion gyroradius decreases with time, keeping $k_\perp \rho_i$ relatively constant.

(1.) A marked dependence of wave amplitude and mode structure is seen as magnetic field strength is varied. Figure 5.9 illustrates the dependence of wave amplitude on poloidal magnetic field strength

in the bridge. Three different plasma densities are indicated in the figure, and each shows a range of magnetic field strengths over which large fluctuations are seen. Outside this range, the fluctuations are very small or the wave structure is significantly modified from that described above, and a different wave is being observed.

The restriction of the wave to a narrow range of field strengths strongly suggests that an ion gyroradius effect is responsible. For low magnetic field ion gyroradii are large, while for high magnetic field gyroradii are small. It is only in a restricted range of the ion gyroradius that the wave is seen. A justification for this type of behavior is found in the discussion of the drift wave in slab geometry from chapter 3. There it is noted that there is an optimal value of $k_\perp \rho_i$ for wave growth.

(2.) Supporting evidence for an ion gyroradius effect is shown in figure 5.10. A series of oscillographs are shown for a 10^{11}/cc plasma generated by the intermediate gun (T_i nominally 10 eV). Voltage on the poloidal capacitor bank is varied from 250 volts to 400 volts. It is seen that the onset of the wave is earlier for higher magnetic fields. This can be explained as an ion gyroradius effect as follows: For higher magnetic field strengths, the ion gyroradius is in the right range to produce large fluctuations as soon as the plasma enters the octupole. For lower magnetic fields, however, the gyroradius is too large when the plasma is injected, but after the ion temperature has had time to cool, the ion gyroradius falls into the right range to produce the fluctuations.

(3.) Further evidence for the ion gyroradius effect is shown in figure 5.11. Two oscillographs are shown, one for levitated rings and one for supported rings. The fluctuations last longer for the levitated case. For the levitated case the decay time of T_i is longer, and the ion gyroradius stays larger for later times than for the supported case. As a result, the gyroradius shrinks to an unsuitably low value for the supported case before it does so for the levitated case. The result is longer lasting fluctuations for levitated cases.

(4.) Figure 5.12 shows the time dependence of $\lambda_\perp$, the toroidal wavelength, for plasmas in the mid-10^{11}/cc density range. Graphs are shown for plasmas with 300, 400, and 500 volts on the poloidal field capacitor bank. In each case $\lambda_\perp$ decreases with time, while ρ_i is also decreasing. This behavior is interpreted as an adjustment of the wavelength to maintain a value of $k_\perp \rho_i$ optimal for wave growth. For a 10 eV ion temperature, the wavelengths of figure 5.12 represent a range in $k_\perp \rho_i$ of 0.5 to 0.9. This range includes the optimal value for growth, $k_\perp \rho_i \cong 0.6$, from the slab theory of section 3B4a.

In this context, the steeper decline of $\lambda_\perp$ with time for the smaller poloidal bank voltages is due to the 1/B dependence of the ion gyroradius ρ_i.

A6. Toroidal Field Effects

The wave is studied with a toroidal magnetic field added to the poloidal field. One effect of toroidal field is to modify the path taken by a field line. The flux surfaces of figure 2.3 are not

modified, but field lines are no longer closed. Since the toroidal and poloidal field strengths vary their ratio in different parts of the octupole, individual field lines change their pitch as a function of poloidal position, and field lines on neighboring flux surfaces have different pitch, a condition known as magnetic shear[3].

Wave properties are relatively unchanged with the addition of small toroidal magnetic fields. Figure 5.13 shows how the wave adjusts its poloidal and toroidal structures to maintain wavefronts which are parallel to the magnetic field lines.

With the addition of enough toroidal field, the wave is stabilized or completely changes character. Figure 5.14 shows the reduction in amplitude of the wave due to the addition of toroidal magnetic field. In the slab theory the condition for magnetic stabilization of a drift wave through magnetic shear is[5]

$$L_s < \frac{L_n^2}{\rho_i}, \text{ where } L_s = \frac{\pi}{2}\left[\frac{d \arctan B_t/B_p}{dx}\right] \qquad (5.2)$$

L_s and L_n are the magnetic shear length and density scale length, and ρ_i is the ion gyroradius. For the case shown in figure 5.14 the shear length is 200 centimeters, while the density scale length is 3 centimeters and the ion gyroradius is 1.5 centimeters. Thus the shear length is much too long to explain the observed stabilization of the wave with equation 5.2.

The question of shear stabilization of drift waves is an active field of inquiry, and there are many different criteria presented by different authors. Ross and Mahajan[6], for example, have a much more restrictive criterion for wave stabilization: $L_n/L_s > 6x10^{-3}$, which would indicate stability for our case.

Evidently, the toroidal magnetic field does disrupt the drift wave structure in this experiment, although the mechanism is as yet undetermined.

A7. Transport

Wave induced transport is discussed in section 3B5. In that discussion we saw that the phase difference between the fluctuating wave potential ϕ and the fluctuating wave density n determines the direction and magnitude of the plasma transport. Using the Langmuir probe with three radially separated tips and the knowledge that neither ϕ nor n have radial phase shifts, the phase shift between ϕ and n is obtained. One tip of the probe is used to collect ion saturation current and another is used to measure floating potential. Assuming that these quantities are accurate indicators of the wave's fluctuating potential and density, a phase shift is measured directly. The ion saturation current fluctuation leads the floating potential fluctuation by 60 to 80 degrees (figure 5.15), and wave induced transport down the density gradient is predicted. The size of the potential fluctuation ϕ, however, is an order of magnitude lower than predicted by the relationship $e\phi/T_e = n/n_0$ of section 3B5. This is not inconsistent with the linear theory, however, since the

wave that is seen in the octupole is a saturated instability, which the linear theory does not treat.

An indication that the observed wave is relatively benign with respect to transport is provided by observations with toroidal field. In the previous section it is mentioned that the wave has a rather sharp cutoff with toroidal field strength. A difference of only 5 gauss is enough for certain plasmas to make the difference between a wave with a substantial fluctuation and one that is stabilized. Since 5 gauss is too little to affect the equilibrium plasma parameters, toroidal field stabilization provides a method for turning off the wave without disturbing the system unduly. The evolution of the plasma density profile in the bridge region is studied with and without the wave. No substantial difference in profile evolution is seen for the case with the wave as compared to the case without the wave. The conclusion is that the wave is not the dominant transport mechanism in the plasmas in which it is found.

For the cases considered above, the ion saturation current profiles have decay times of 3 to 4 milliseconds immediately after plasma injection. For the case in which the drift wave is present, the calculated flux caused by the wave would, by itself, generate a decay time of about 10 milliseconds. This should be observable, and the fact that it is not may indicate that using the fluctuating floating potential, fluctuating ion saturation current, and the phase difference between them is not an accurate approximation for finding the wave induced flux?

A8. Magnetic Fluctuations

A magnetic probe, consisting of an electrostatically shielded wire coil, is used to measure magnetic fluctuations associated with the drift wave. Figure 5.16 shows density and poloidal magnetic fluctuations as a function of time. Note that they share the same frequency and maintain their phase relationship.

For a plasma in the 10^{12}/cc density range, the B_{pol} fluctuations reach a 0.06% level, referenced to the applied magnetic field. The density fluctuation level is about 20% in this 10 eV plasma, and the two fluctuation levels are of the same magnitude as expected from diamagnetic effects.

There are also fluctuations in the toroidal magnetic field, which seems to indicate that there are currents associated with the drift wave which flow along the magnetic field lines.

In section 3B1 the condition $\omega/k_{\parallel} \ll C_{Alfven}$ is introduced as the condition that the wave be purely electrostatic. For a 3.5×10^{12}/cc plasma $\omega/k_{\parallel} \cong 7\times10^{6}$cm/s $\ll C_{Alfven} \cong 4\times10^{7}$cm/s. As a rough check that the magnetic character of the wave is not changing as the density is increased (and C_{Alfven} correspondingly decreased) the ratio of the poloidal to the toroidal magnetic fluctuations is monitored for a 2×10^{11}/cc plasma and a 3.5×10^{12}/cc plasma. No change in this ratio (about 1:3) is seen, adding indirect support to the statement made above that the magnetic fluctuations seem to be a manifestation of diamagnetic effects.

B. Linear Quadrupole Experiment

Meade and Yoshikawa[8] observed a wave in the Princeton linear quadrupole which had the same spatial structure as the mode described above. In the following section their observations are described and compared with the levitated octupole observations.

A linear quadrupole is a multipole device like the octupole, but having only two internal rings rather than four and being linear rather than toroidal. A helium plasma was produced using rf power or microwaves. Its density was 2×10^{12}/cc with a background neutral density of 1×10^{-4} torr. The ion temperature was 0.5 - 1.0 eV, while the electrons were 5 eV. Typical magnetic field strength was 2.4 kilogauss. Compared to the octupole this represents a cool, dense plasma with a large background neutral density in a high magnetic field.

A drift wave was observed with frequency 100 kHz ($\omega_{*e}/3$) propagating in the V_{*e} direction. The density fluctuation had a radial structure which peaked in the local bad curvature region (the common flux region outside Ψ_{sep}). The wave was standing in the poloidal direction with odd symmetry. Wave amplitude peaked in the local bad curvature regions of the common flux with $\delta n/n_0 = 15\%$. The toroidal wavelength was 6 - 10 mm, yielding $k_\perp\rho_i = 0.5$ to 0.8.

In all respects the wave's spatial structure, as described above, is similar to that seen in the octupole. The frequency of the wave bears the same relationship to ω_{*e} as seen in the octupole ($\omega \cong \omega_{*e}/3$) and $k_\perp\rho_i$ is in the same range(0.5 to 0.8 as compared to

0.5 to 0.9). The value of $\delta n/n_0$ is about half of the octupole value. The toroidal wavelengths are extremely small by octupole standards (10 mm as opposed to 20 cm). Wavelengths this small are not seen in the octupole, so that for small enough ρ_i the drift mode is absent.

Meade and Yoshikawa found that the wave did not alter the plasma lifetime through increased plasma transport. The ion saturation current fluctuation was found to lead the floating potential fluctuation by 15 degrees (within 20 degrees), while the condition $\delta n/n_0 = e\,\delta\phi/T_e$ was found to hold within 50%.

In this respect, the quadrupole results differ greatly from the octupole. Although the waves in the octupole are also found to produce negligible transport, the phase difference between density and potential is 60 to 80 degrees, rather than 15 degrees. Also, our potential fluctuation amplitude is an order of magnitude smaller than predicted by $T_e\delta n/n_0$, not within 50%.

On the whole, there are striking similarities between the results of Meade and Yoshikawa and the results of the octupole experiment reported above. The same type of drift wave appears to be observed in both experiments. However, Meade and Yoshikawa did not explore the density or magnetic field dependence of the wave, ion gyroradius effects, the addition of a toroidal magnetic field (axial in their case), nor magnetic fluctuations. These topics are all explored in section A for the wave in the octupole.

Table 5.1 - Typical Wave and Plasma Parameters

Wave Properties	
Frequency	30 kHz
Toroidal Mode Number	60 ($\lambda_\perp$=20 cm)
Poloidal Structure	Standing Wave Peaked in Bridges Odd Poloidal Symmetry
Radial Structure	Standing Wave Peaked in Common Flux
Effect on Transport	Negligible
Stabilization Mechanism	Toroidal Magnetic Field Ion Cooling with Neutrals
Instability Mechanism	Bad Local Magnetic Curvature Ion Gyroradius Size
Plasma Parameters	
Density	$1x10^9$ - $2x10^{12}$/cc
Temperature	T_i = 10 to 50 eV T_e = 5 to 15 eV
Neutral Density	$1x10^{-6}$ Torr
Poloidal Field	200 - 300 Gauss
Beta (8π nT/B^2)	0.004% to 8.%
Diamagnetic Frequency	$\omega_{*e}/2\pi$ = 70 kHz

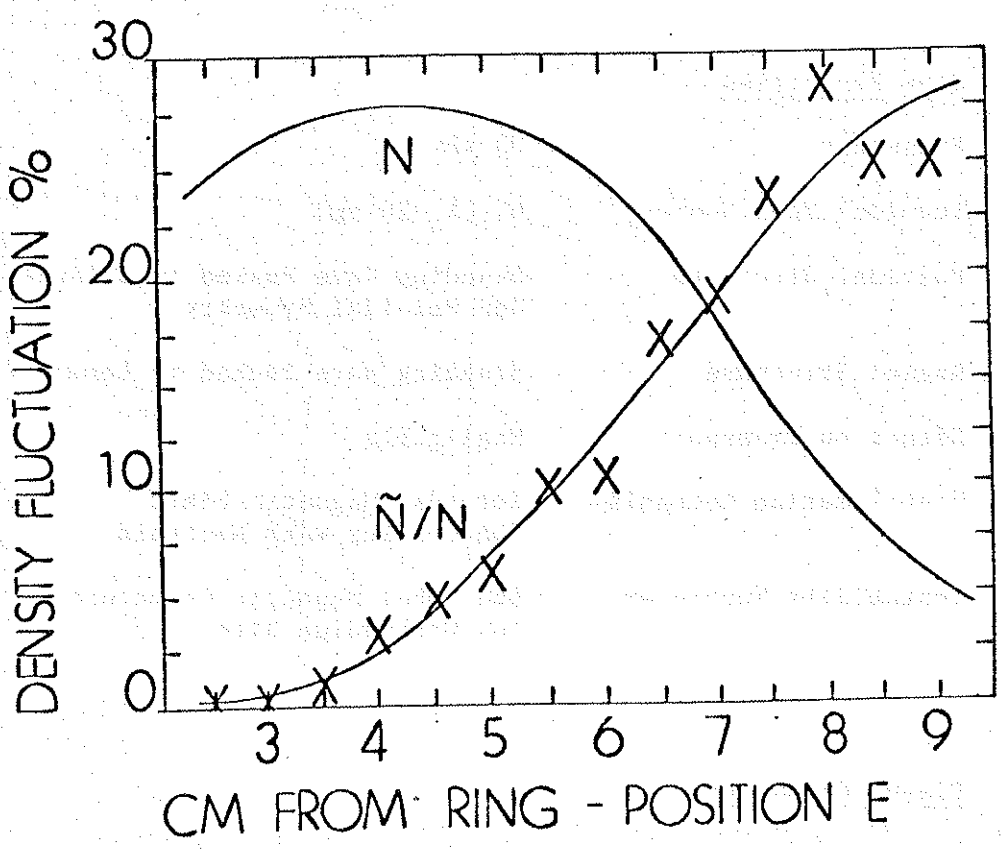

Figure 5.1 - Radial Mode Structure

The relative amplitude of the density fluctuation is shown as a function of radial position at probe port E. An equilibrium density profile is shown in arbitrary units for reference.

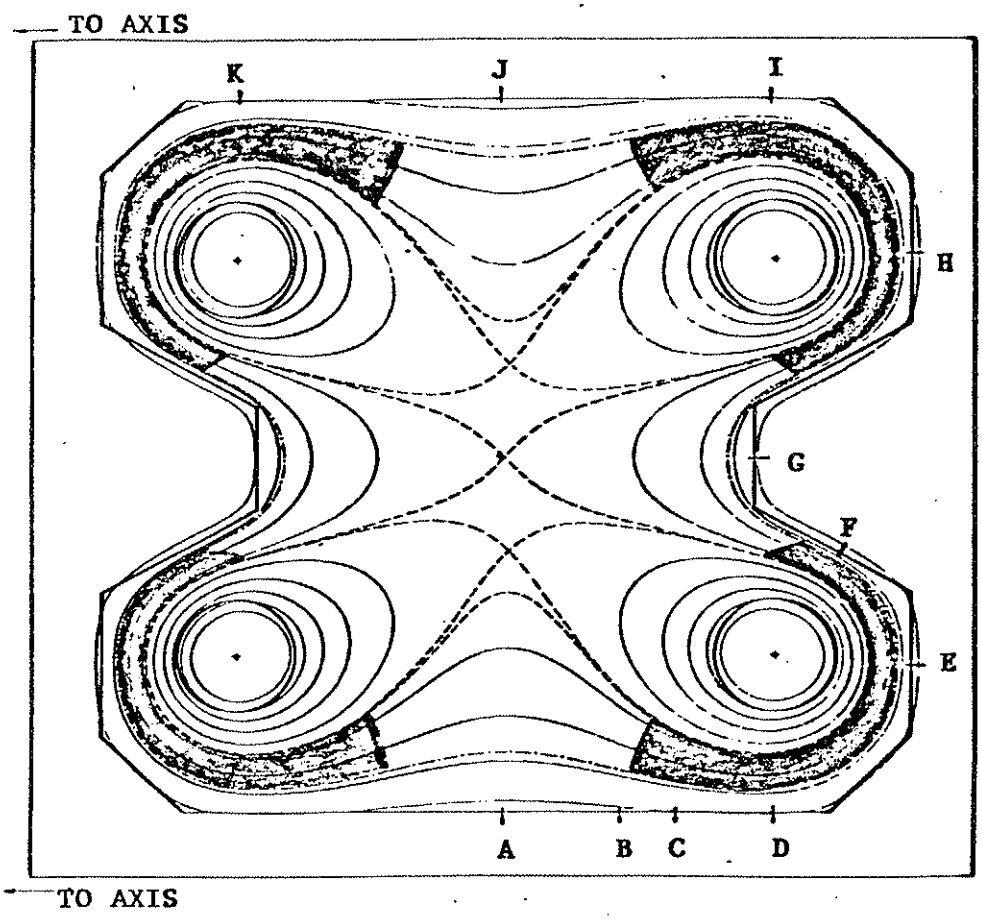

Figure 5.2 - Regions of Locally Bad Magnetic Curvature

The shaded portions of the flux plot show the regions of bad magnetic curvature referred to in the text. They occur in the bridge regions outside the separatrix.

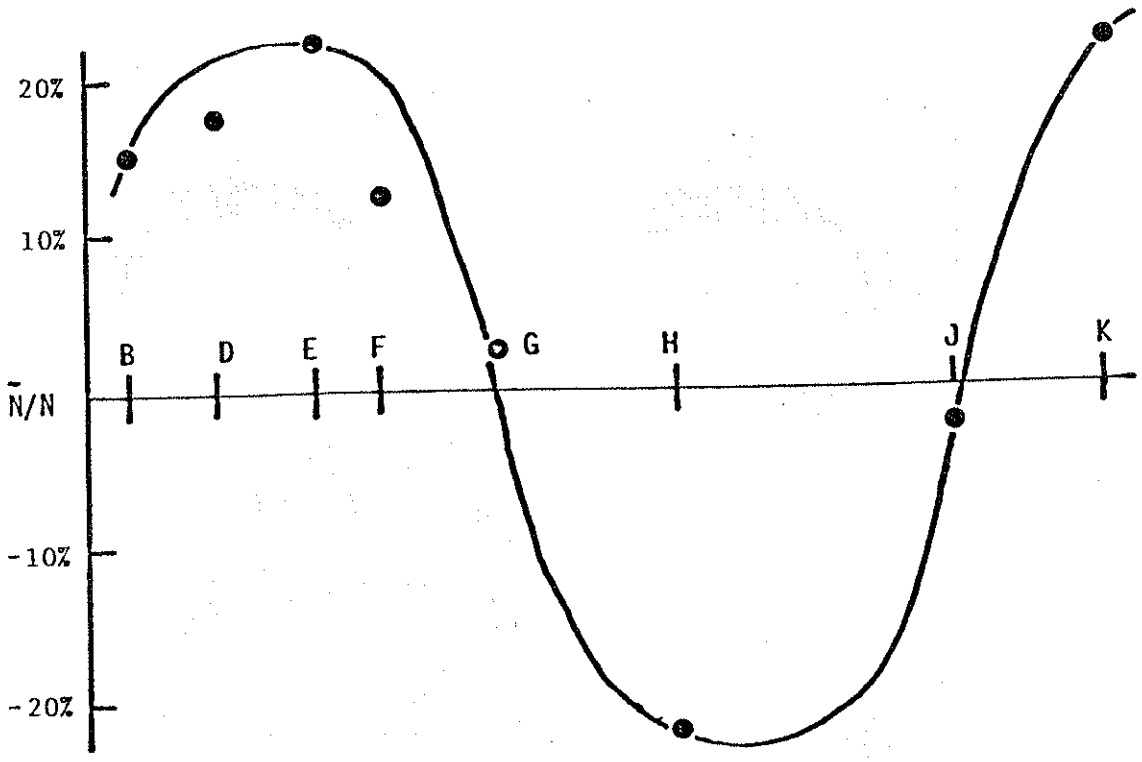

Figure 5.3 - Poloidal Mode Structure

The relative amplitude of the density fluctuation is shown as a function of poloidal position. There is a 180 degree phase shift between signals at probe ports E and H, indicated by a difference in sign of the fluctuation per cent.

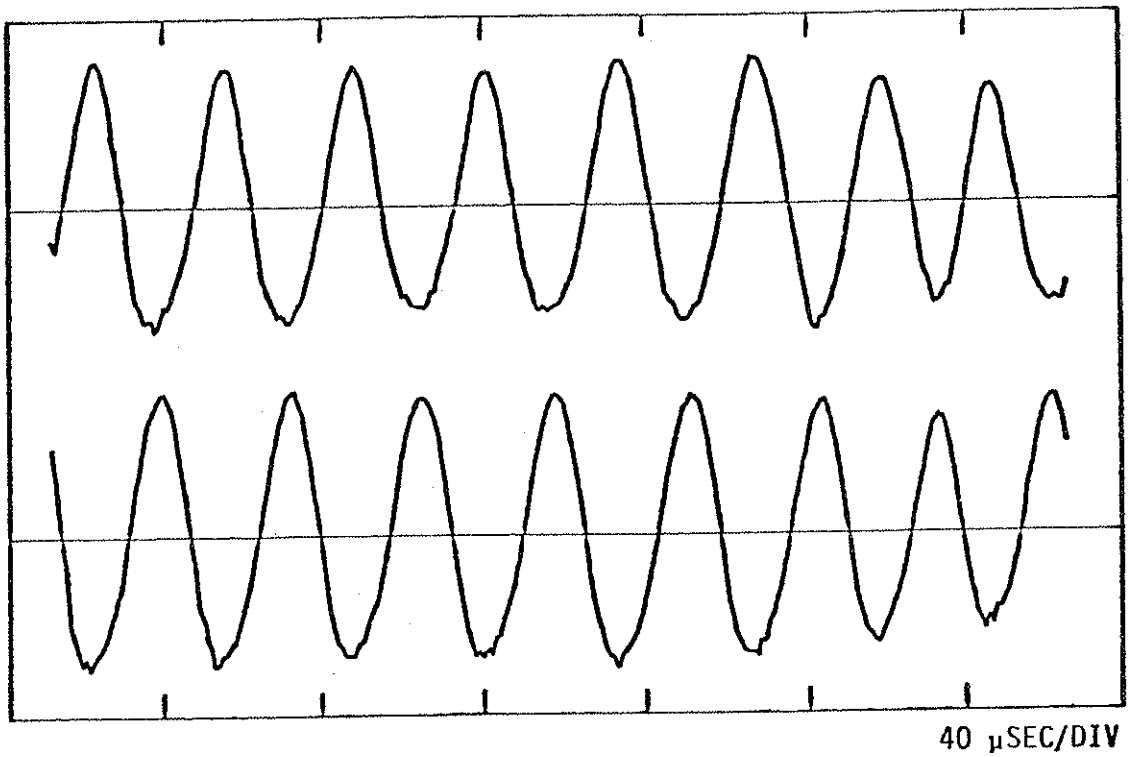

Figure 5.4 - Odd Poloidal Symmetry

The fluctuating portion of the ion saturation current is shown for port H (top) and port E (bottom). They are 180 degrees out of phase with each other.

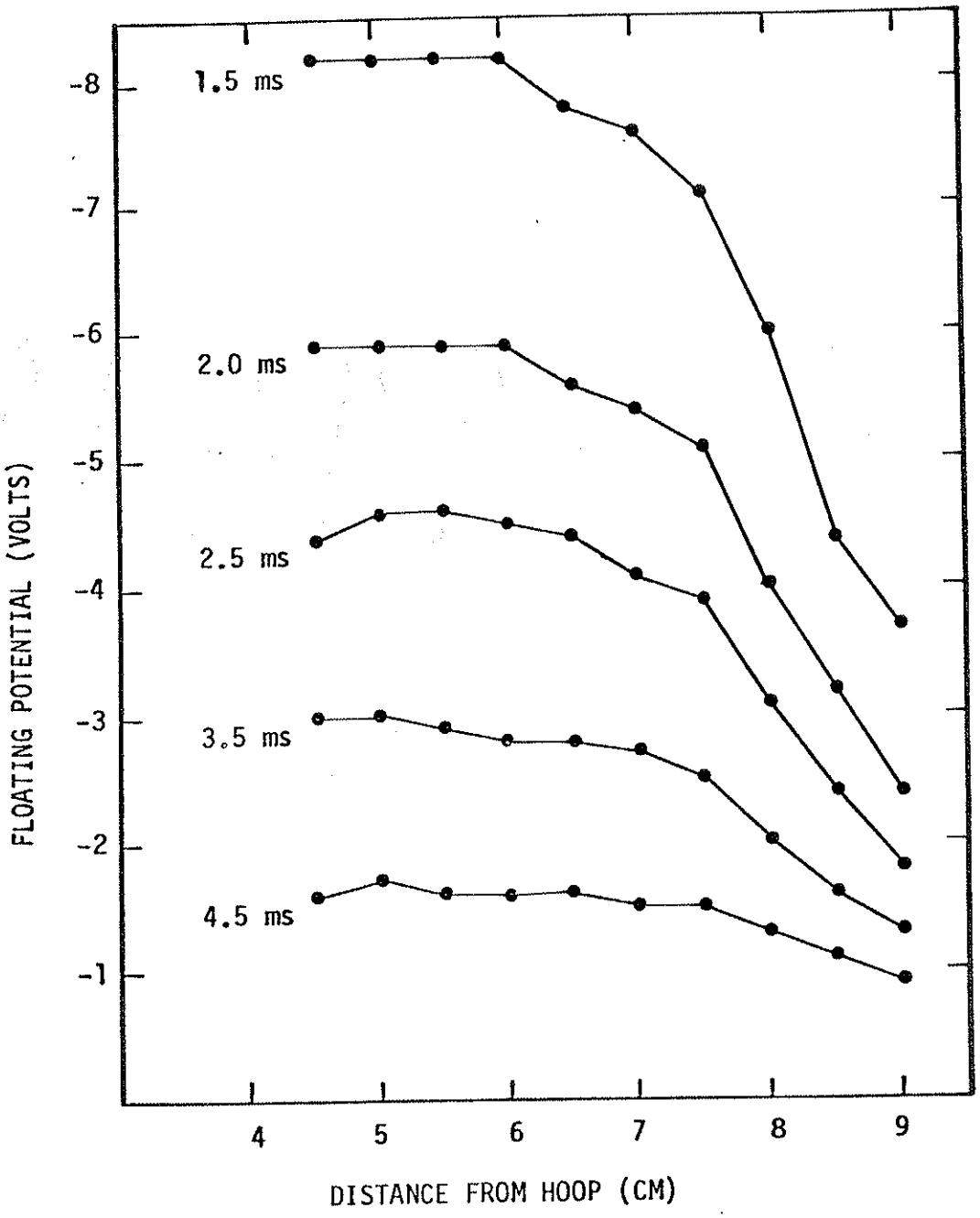

Figure 5.5 - Floating Potential Profile

The floating potential at probe port E is plotted versus radial position for various times after plasma injection. The potential gradient indicates an ExB velocity in the V_{*e} direction.

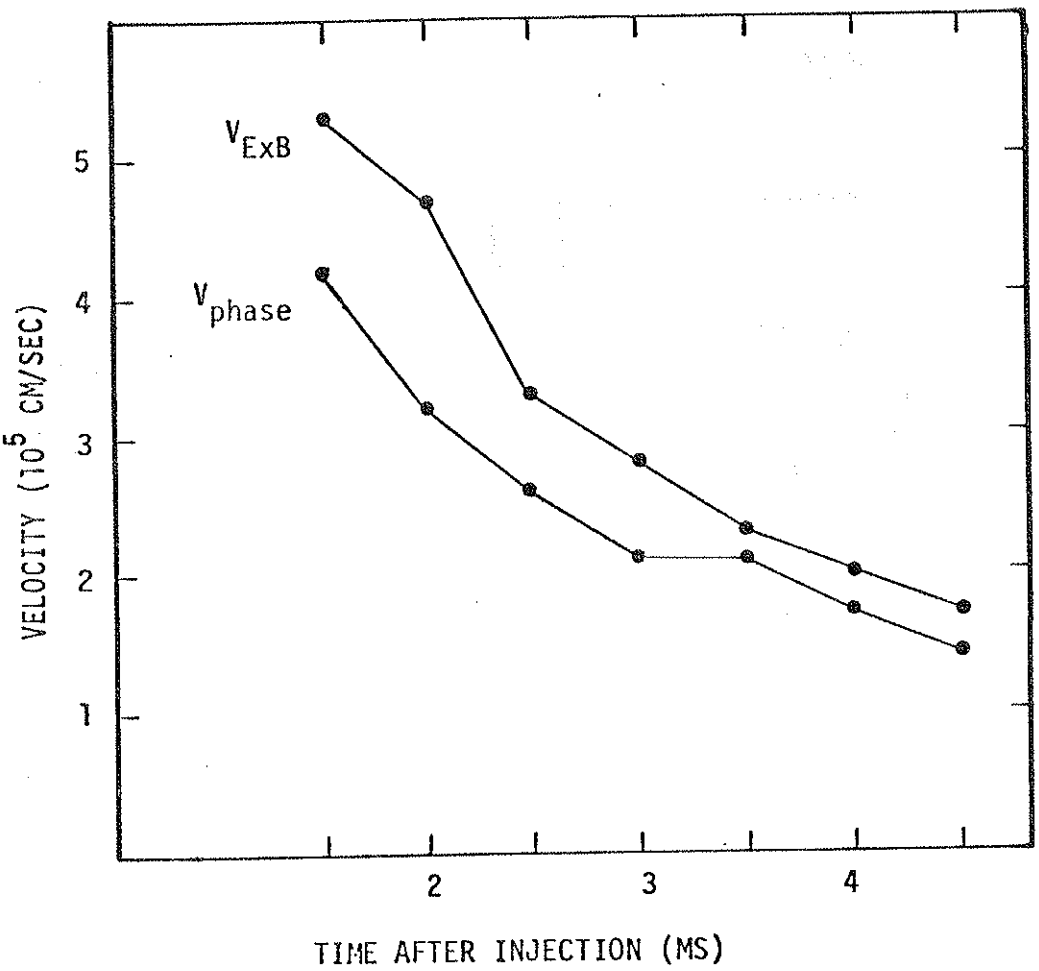

Figure 5.6 - Phase Velocity Compared with ExB Velocity

The measured phase velocity of the wave is plotted along with the ExB velocity of the plasma (calculated from the data of figure 5.5). The time development of the velocities is shown for a position 7.5 cm from the hoop.

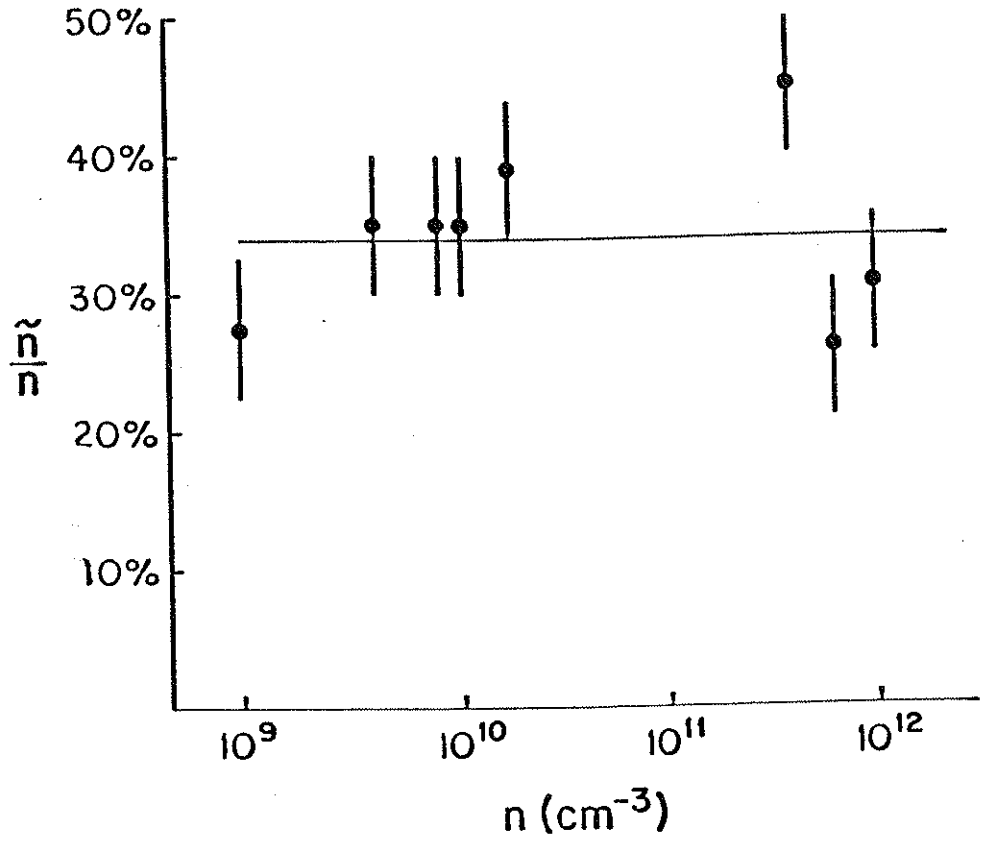

Figure 5.7 - Wave Amplitude Dependence on Density

The relative amplitude of the density fluctuation is shown as a function of plasma density. The wave is present at large amplitude over three orders of magnitude in plasma density.

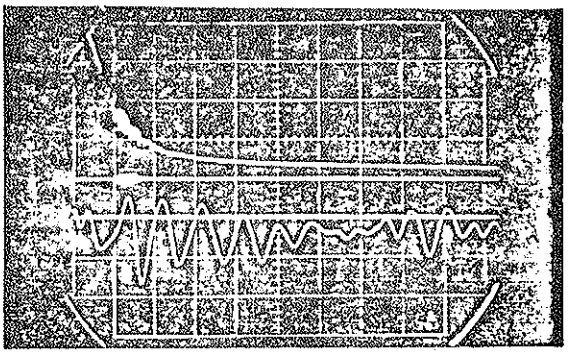

$1x10^{-6}$ Torr Neutral Pressure

(2 ms/div)

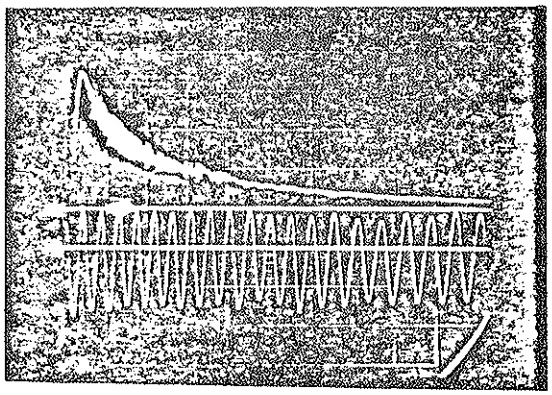

$7x10^{-6}$ Torr Neutral Pressure

(2 ms/div)

Figure 5.8 - Wave Stabilization with Neutral Gas

Density fluctuations are shown for plasmas with background neutral densities of $1x10^{-6}$ torr (top) and $7x10^{-6}$ torr (bottom). The bottom trace on each photo shows an expanded time scale for 2 to 3 ms after plasma injection. Large neutral density stabilizes the wave through cooling of the ions.

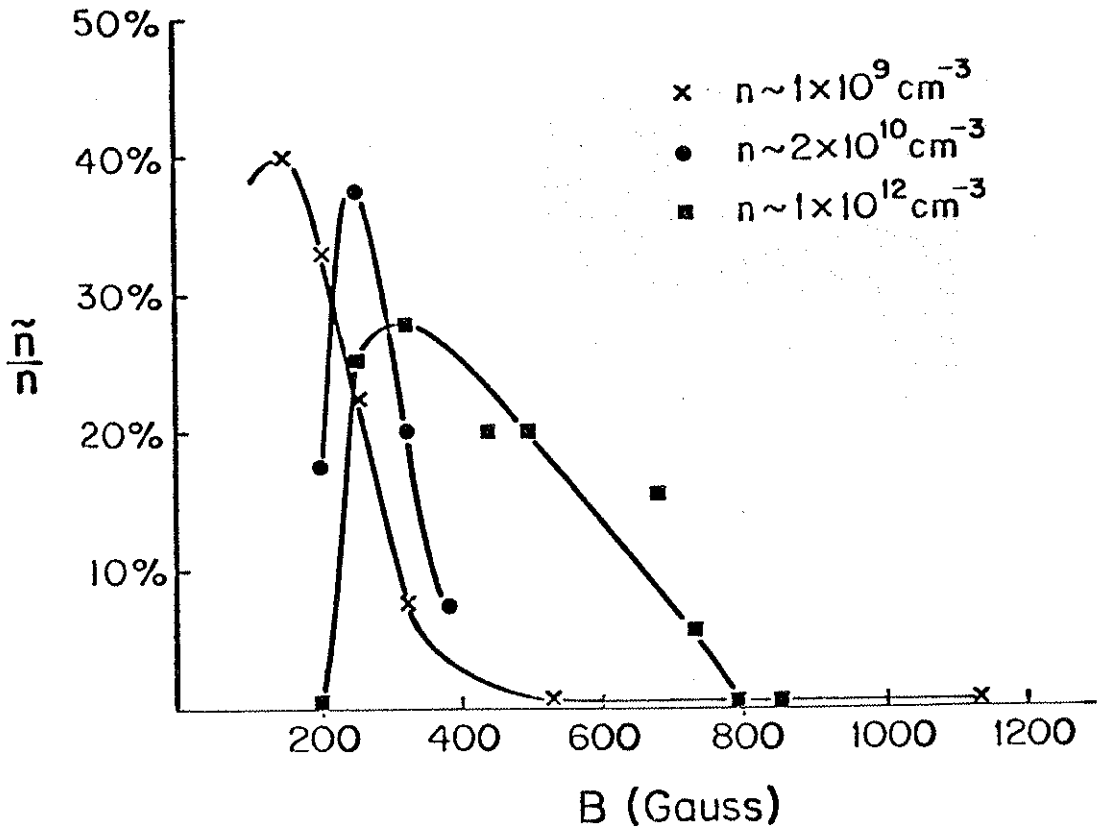

Figure 5.9 - Wave Amplitude Dependence on Magnetic Field

The relative amplitude of the density fluctuation is shown as a function of the poloidal magnetic field strength at postion E, 7.5 cm from the hoop. The wave is stabilized at very low or high magnetic fields through ion gyroradius effects.

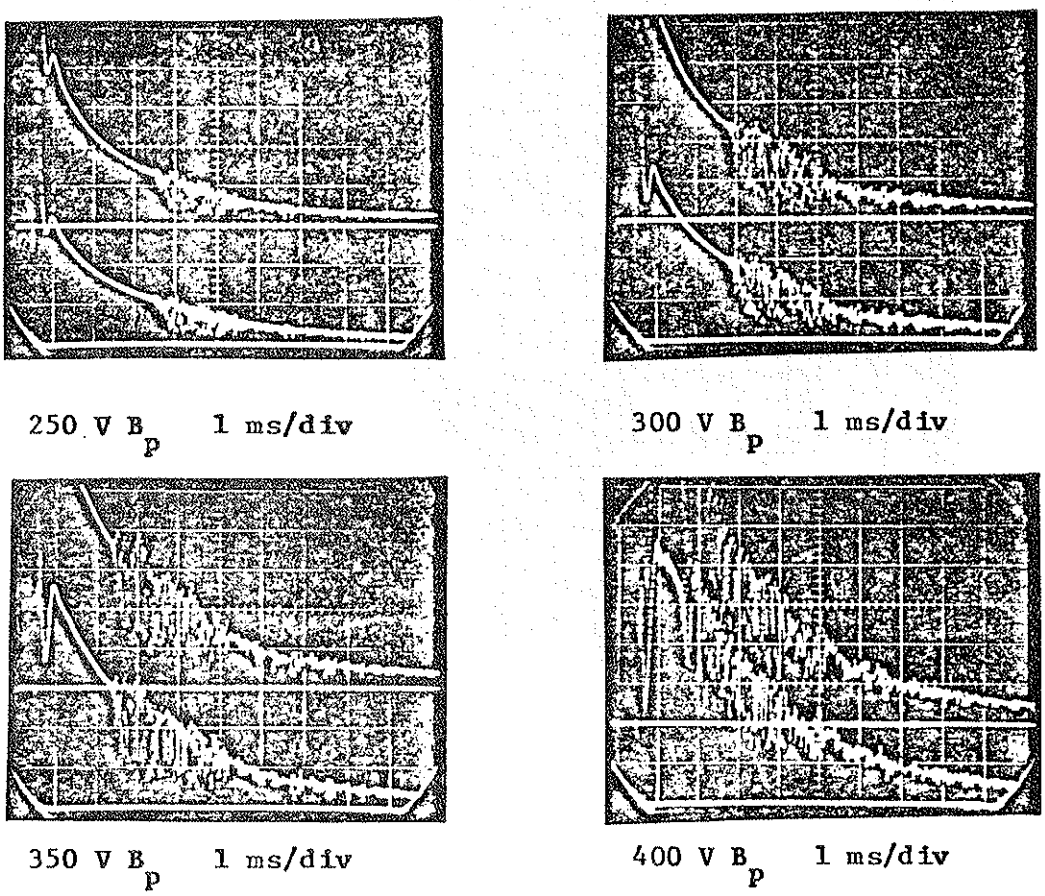

Figure 5.10 - Dependence of Mode Onset with Magnetic Field

The pictures above show ion saturation current fluctuations vs time as a function of poloidal magnetic field strength. As the field is increased, the onset of the wave becomes earlier.

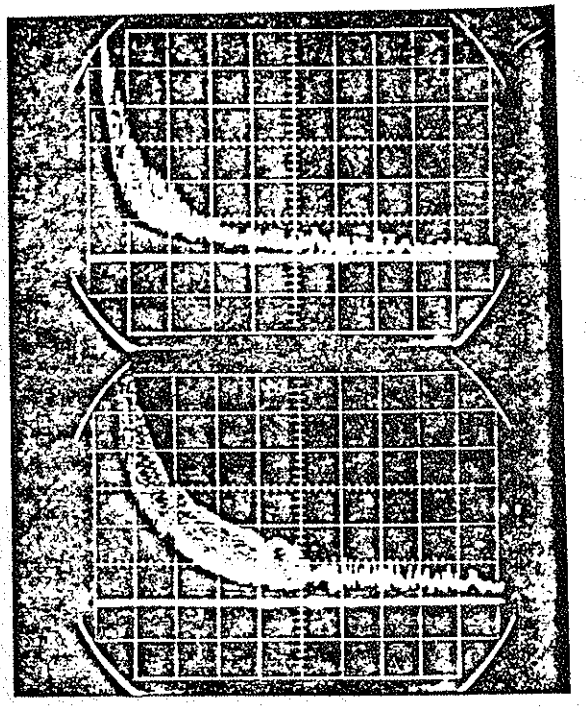

SUPPORTED RINGS

(2 ms/div)

LEVITATED RINGS

(2 ms/div)

Figure 5.11 - Effect of Levitation on Mode Turn-Off

The pictures above show ion saturation current fluctuations vs time for a levitated hoop case (top) and a supported hoop case (bottom). Fluctuations last longer for the levitated case, indicative of the slower time decay of the ion temperature.

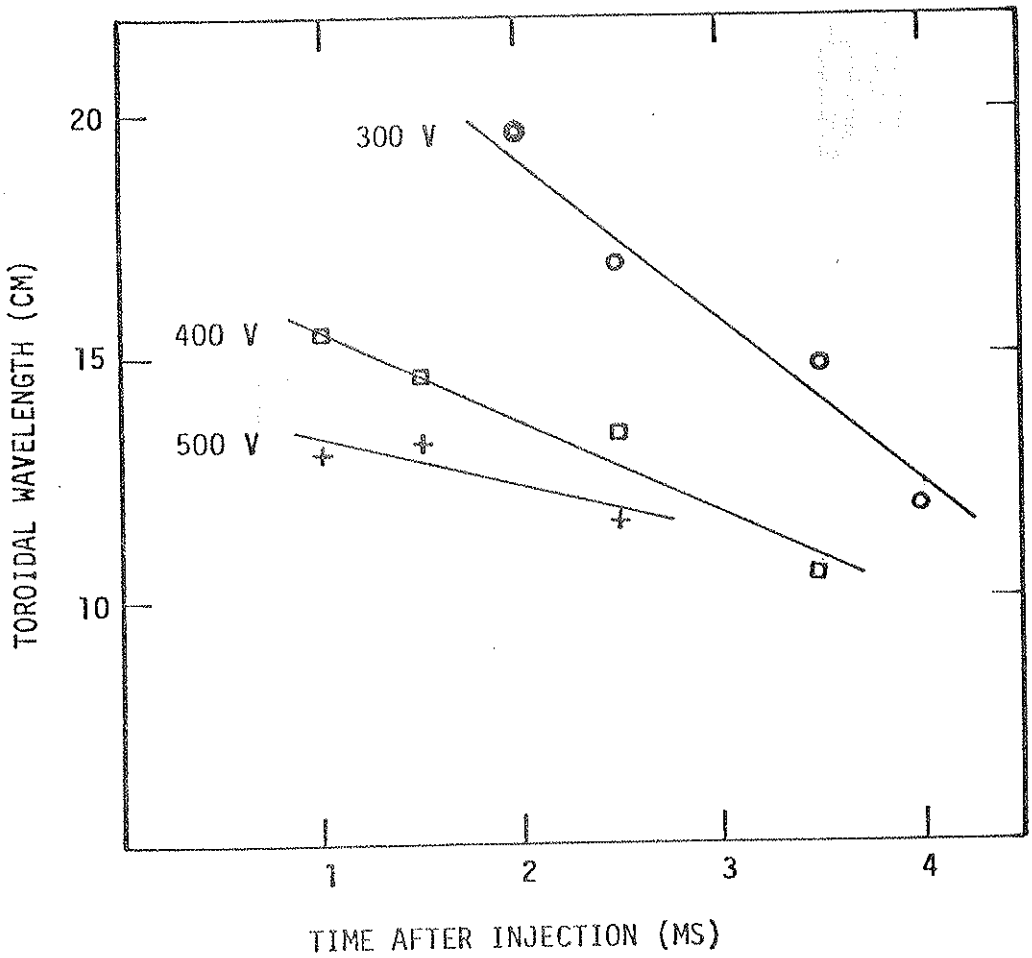

Figure 5.12 - Time Dependence of Wavelength

The graph above shows the time dependence of the toroidal wavelength $\lambda_\perp$ for three voltage settings on the poloidal field capacitor bank. Typical uncertainties in wavelength are 1 to 2 cm. The wavelength decreases with time, keeping $\rho_i/\lambda_\perp$ relatively constant.

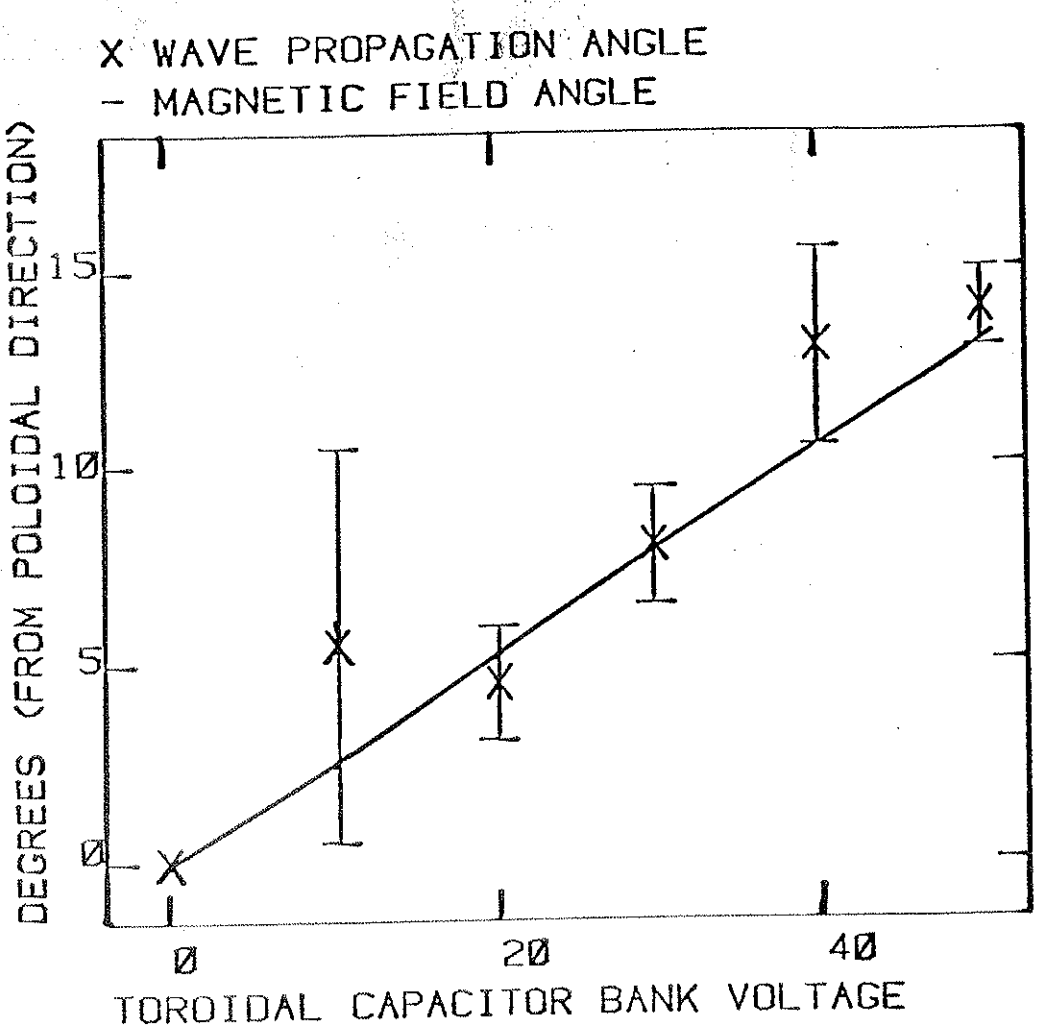

Figure 5.13 - Dependence of the Direction of Wave Propagation on Toroidal Field

The solid line shows the angle a field line makes with the poloidal direction as toroidal field is added to a poloidal field (300 volts on poloidal capacitor bank). The points X with error bars show the angle a wavefront makes with the poloidal direction. The graph shows that wavefronts coincide with field lines.

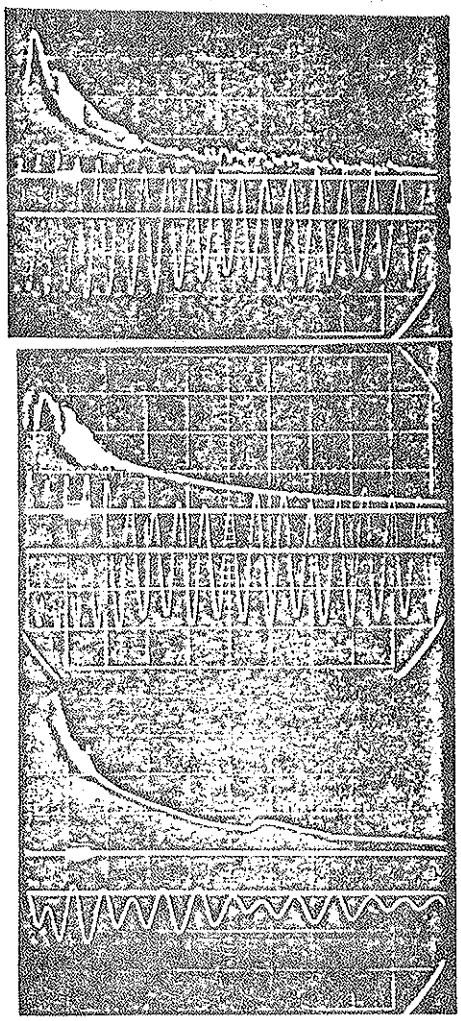

B_p = 300 gauss, B_t = 0 gauss
(2 ms/div, 100 μs/div)

B_p = 300 gauss, B_t = 25 gauss
(2 ms/div, 100 μs/div)

B_p = 300 gauss, B_t = 35 gauss
(2 ms/div, 100 μs/div)

Figure 5.14 – Mode Stabilization with Toroidal Field

The three oscillographs show ion saturation current and the associated fluctuations. As toroidal magnetic field is added (from top to bottom) the drift wave is stabilized.

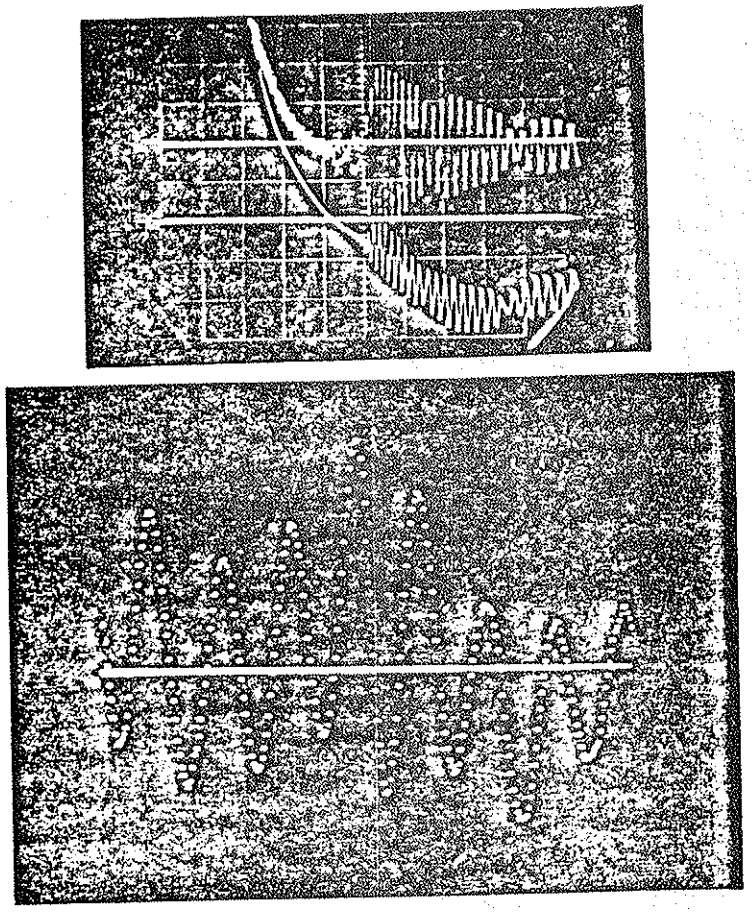

Figure 5.15 - Phase Shift between Density and Potential Fluctuations The top oscillograph shows ion saturation current (top) and floating potential (bottom) fluctuations in the first two milliseconds after plasma injection. The second oscillograph depicts the correlation function of two such signals. The shift of the large central peak to the left of center indicates that the density fluctuation leads the potential fluctuation, by 60 degrees (1/6 of a wave period) in this case.

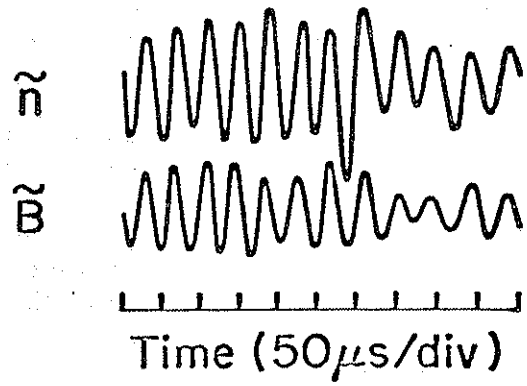

Figure 15.16 - Magnetic Fluctuations

The drawing above depicts ion saturation and poloidal magnetic field fluctuations. The signals are taken at different probe ports and the phase difference removed to show the similarity in frequency and constancy of phase difference.

References for Chapter 5

1. J. R. Drake, "Observed Instabilities in the Trapped Ion Regime in the Levitated Octupole", University of Wisconsin PLP 697, 1976.

2. S. I. Braginskii, "Transport Processes in a Plasma", in Reviews of Plasma Physics, ed. M. A. Leontovich, (Consultants Bureau, New York, 1965), volume 1, p. 215.

3. J. R. Drake, "Bounce Times, Magnetic Drifts and a Comment on Shear Length for the Levitated Octupole", University of Wisconsin PLP 681, 1976.

4. G. A. Navratil, "Diffusion Coefficient Scaling in the Wisconsin Levitated Octupole", Ph.D. Thesis, University of Wisconsin PLP 693, 1976, chapter 2.

5. J. B. Taylor, "Does Magnetic Shear Stabilize Drift Waves?", in Plasma Physics and Controlled Nuclear Fusion Research, (IAEA, Vienna, 1976), volume 2, p. 323.

6. D. W. Ross and S. M. Mahajan, "Are Drift Wave Eigenmodes Unstable?, PRL 40, 324 (1978).

7. R. W. Motley, "Hot-Probe Measurements of Space Potential Oscillations in a Plasma", J. Appl. Phys. 43, 3711 (1972).

8. D. M. Meade and S. Yoshikawa, "Observations of a Ballooning-Type Instability in a Plasma Confined by a Quadrupole Magnetic Field", Physics of Fluids 10, 2649 (1967).

CHAPTER 6 - DRIFT WAVE THEORY FOR THE OCTUPOLE

In order to analyze the experimental results of chapter 5, a more detailed theory of the drift wave is needed. The slab model deals with finite ion gyroradius, magnetic curvature drifts, and electron Landau damping. However, it does not deal with the poloidal and radial structures, which are such a prominent feature of the experimental results.

In section A a short description is given of two approaches to the problem of drift waves with poloidal structure. Rutherford and Frieman[1] used a WKB approximation, and Coppi and Minardi[2] used integration over unperturbed orbits. A discussion is made of the validity of their particular results for the octupole, and it is concluded that neither is applicable. In section B the method of integration over orbits is applied to multipole field geometry to give a dispersion relation that is applicable to the octupole.

A. Survey of Previous Work

Rutherford and Frieman[1] considered drift instabilities in a multipole. They used a WKB formulation to treat the poloidal and radial structure of the fluctuating potential. The condition $k_{\parallel} V_e \gg \omega \gg k_{\parallel} V_i$ was employed, and weak magnetic curvature ($\omega_d \ll \omega$) was assumed. The effects of trapped ions and electrons were also considered. The condition for wave growth $\omega < \omega_{*e}$ was found by constructing a quadratic form, and the actual growth rates were

determined by pertubation techniques on the quadratic form. For $\omega \cong \omega_{*e}$ they found two drift modes with the following conditions for instability:

$$\text{drift-ballooning mode} \quad \kappa b > L_n^2/L_\kappa^2 \tag{6.1}$$

$$\text{drift-universal mode} \quad b > L_n/L_b$$

where $\kappa = 2\ (d\ \ln B/d\ \ln N) = \omega_d/\omega_*$, $b = k_\perp^2\rho_i^2$, and L is a scale length. The drift-ballooning mode is localized in regions of bad curvature, and the drift-universal mode is localized in regions of large ion gyroradius. The drift-ballooning mode is found when $\kappa > b$ and the drift-universal when $b > \kappa$.

Thus Rutherford and Frieman do predict localized modes. The octupole satisfies the conditions of equation 6.1 for either mode. In fact, $b > \kappa$ since $b > 1.9$ in the outer nose, while κ has its largest value of less than 1. in the bridge. Thus Rutherford and Frieman predict that the drift-universal mode should appear in the octupole, but the drift-ballooning type structure is seen. Yoshikawa[3] makes this same complaint for the linear quadrupole experiment described in chapter 5.

Coppi and Minardi[2] approached the problem of drift waves in a multipole using the method of integration over unperturbed orbits to solve the Vlasov equation. They considered the case of trapped ions with $\omega < k_\parallel V_i \ll k_\parallel V_e$ in the presence of odd and even symmetry waves. They also used a quadratic form to obtain a condition for instability

and an estimate of the values of frequency and growth rate. Their work is not directly applicable to the octupole experiment, however, since they neglected the effects of magnetic drift velocities for the odd symmetry mode and treated the case of a temperature gradient driven mode. The large magnetic drifts in the octupole must be taken into account in any theoretical treatment. The ion temperature gradient has been measured, and it is negligible. Coppi and Minardi also neglected electron Landau damping, an effect we should like to take into account.

In the next section we make use of the same general approach used by Coppi and Minardi to generate a dispersion relation for the octupole.

B. Derivation of the Dispersion Relation

In this section a dispersion relation is derived using kinetic theory and incorporating the following features:

1. finite ion gyroradius ($k_\perp \rho_i \sim 1$)
2. poloidal mode structure
3. single particle drifts due to magnetic curvature and gradients
4. electron Landau damping ($k_\parallel V_e \gg \omega \gg k_\parallel V_i$)

Initially, the radial structure and trapped particle effects are treated, but they are not retained. The observed poloidal mode structure of the octupole is used in the final form of the dispersion relation.

The dispersion relation is derived using the general approach of Coppi and Minardi[2], outlined in this paragraph. Starting with the collisionless Vlasov equation, the perturbed particle distribution function is found by linearizing and integrating over unperturbed orbits. Calculations are carried out using flux coordinates, as introduced in chapter two. The Fourier transform of the toroidal coordinate θ and the Laplace transform of time t are taken. The wave's electric potential ϕ is separated into a product of a function of the radial coordinate $G(\psi)$ and a function of the parallel coordinate $H(\chi)$. An average is taken over the phase angle of the particle motion perpendicular to the field and integration over the particle's parallel motion is done using an expansion in bounce harmonics. Integrating over velocity space yields electron and ion density perturbations, which are equated, using quasineutrality. A quadratic form is produced from the quasineutrality condition by taking the product of ϕ^* and integrating over the volume of a flux surface. A dispersion relation is the final result.

B1. Vlasov Equation

The collisionless Vlasov equation is considered.

$$\frac{\partial F}{\partial t} + \vec{v}\cdot\nabla F + \frac{q}{m}\left(\frac{\vec{v}\times\vec{B}}{c} + \vec{E}\right)\cdot\nabla_v F = 0 \qquad (6.2)$$

where F is the single particle distribution function, $\vec{E}$ the electric

field, $\vec{B}$ the magnetic field, and q, m, and v the particle charge, mass, and velocity.

Writing F and $\vec{E}$ as sums of equilibrium and perturbed quantities (due to an electrostatic wave), we obtain $F = F_0 + f$ and $\vec{E} = \vec{E}_0 - \nabla\phi$. Linearizing the Vlasov equation with respect to perturbed quantities, we obtain, in the absence of an equilibrium electric field

$$\frac{DF_0}{Dt} = \frac{\partial F_0}{\partial t} + \vec{v}\cdot\nabla F_0 + \frac{q}{mc}\,\vec{v}\times\vec{B}\cdot\nabla_v F_0 = 0 \tag{6.3}$$

$$\frac{Df}{Dt} = \frac{\partial f}{\partial t} + \vec{v}\cdot\nabla f + \frac{q}{mc}\,\vec{v}\times\vec{B}\cdot\nabla_v f = \frac{q}{m}\,\nabla\phi\cdot\nabla_v F_0$$

where D/Dt is the total time derivative, taken over the path of a particle.

Since $DF_0/Dt = 0$, the equilibrium distribution function can be expressed as a function of constants of the motion[4]. From the Lagrangian formulation of the equations of motion, one obtains the energy $E = mv^2/2$ and the canonical angular momentum $P_\theta = q\psi/c + mR^2\dot{\theta}$ as constants of the motion. Here R is the distance from the axis of symmetry (the center line of the octupole) and ψ is the radial flux coordinate of a particle. The guiding center of the particle is related to the canonical angular momentum by the relation $\psi_{gc} = cP_\theta/q$.

An equilibrium distribution function with temperature T, density

n_0 at position ψ_0, and a density gradient scale α can be written simply as

$$F_0 = (1 + \alpha(\psi_0 - \psi_{gc}))\ F_{Max} \tag{6.4}$$

where $F_{Max} = n_0(m/2\pi T)^{3/2}\exp(-E/T)$ is the Maxwellian distribution function.

B2. Unperturbed Orbit Integration

Equation 6.3 expresses the time evolution of f in terms of the trajectories of particles along their unperturbed orbits. Taking the time integral of equation 6.3 with respect to the unperturbed orbits yields

$$f = \frac{q}{m}\int_{-\infty}^{t} dt'\ \nabla\phi\cdot\nabla_v F_0 \tag{6.5}$$

where the quantities being integrated depend on t′ through the particle position and velocity $\vec{x}(t')$ and $\vec{v}(t')$, as well as t′ explicitly. At time t, this particle is at $\vec{x}(t)$ and $\vec{v}(t)$, the values for which f is evaluated.

The integrand may be rewritten, noting that

$$\frac{D\phi}{Dt} = \frac{\partial\phi}{\partial t} + \vec{v}\cdot\nabla\phi \tag{6.6}$$

$$\nabla\phi\cdot\nabla_v F_0 = m\,\frac{\partial F_0}{\partial E}\,\vec{v}\cdot\nabla\phi + \frac{mc}{q}R\,\frac{\partial\phi}{\partial\theta}\,\frac{\partial F_0}{\partial\psi_{gc}} \tag{6.7}$$

Since F_0 and its derivatives $\partial F_0/\partial E$ and $\partial F_0/\partial \psi_{gc}$ are constants of the motion, we can take them outside of the integral to obtain

$$f = q \frac{\partial F_0}{\partial E} \phi - q \frac{\partial F_0}{\partial E} \int_{-\infty}^{t} dt' \frac{\partial \phi}{\partial t} + c \frac{\partial F_0}{\partial \psi_{gc}} \int_{-\infty}^{t} dt' \frac{\partial \phi}{\partial \theta} \tag{6.8}$$

B3. Laplace and Fourier Transforms

Taking the Laplace transform in time t and the Fourier transform in the toroidal coordinate θ yields

$$\hat{f}_{l\omega} = q \frac{\partial F_0}{\partial E} \hat{\phi}_{l\omega} + \left[i\omega q \frac{\partial F_0}{\partial E} + ilc \frac{\partial F_0}{\partial \psi_{gc}} \right] \tag{6.9}$$

$$\cdot \left[\int_{-\infty}^{t} dt' \hat{\phi}_{l\omega}(t') \exp(i\omega(t-t') + il(\theta(t')-\theta(t)) \right]$$

where ω is the mode frequency in radians per second, assuming a positive but small imaginary part, and l is the toroidal mode number of the mode. In what follows we treat the case of a single mode, and drop the subscripts l and ω and the carat over f and ϕ.

B4. Particle Orbits

In order to perform the integral over unperturbed orbits we consider the time evolution for the coordinates of a particle, expanded about the particle's gyrocenter. To lowest order in the ratio of gyroradius to radial and magnetic scale lengths ($\rho RB\, \partial \ln R/\partial\psi = \rho/L_{R\psi}$, $\rho RB\, \partial \ln B/\partial\psi = \rho/L_{B\psi}$, $\rho B\, \partial \ln R/\partial\chi = \rho/L_{R\chi}$, $\rho B\, \partial \ln B/\partial\chi = \rho/L_{B\chi}$) the orbit is

$$\psi(t') - \psi(t) = \frac{RB}{\Omega} [2\mu B/m]^{1/2} \cos(\xi) \Big[_t^{t'} \tag{6.10}$$

$$\theta(t') - \theta(t) = [2\mu B/m]^{1/2} \frac{\sin(\xi)}{R\,\Omega} \Big[_t^{t'} + \int_t^{t'} d\tau\, (\mu B/m + v_\parallel^2) \frac{B}{\Omega} \frac{\partial \ln B}{\partial \psi}$$

$$\chi(t') - \chi(t) = \int_t^{t'} d\tau\, [2E/m - 2\mu B/m]^{1/2}\, B$$

$$\xi(t') = \xi_0 + \int_t^{t'} d\tau\, \Omega$$

where ξ is the phase angle of the particle in its gyro-orbit and B, R, and Ω are evaluated at $\psi(t)$ and $\chi(t, t', \text{or } \tau)$. The shorthand expression $X \Big[_t^{t'}$ is interpreted $X(t) - X(t')$. The ψ and θ equations describe a circular gyromotion in the local magnetic field along with a drift velocity in the θ direction due to the non-uniform magnetic field. The χ equation describes the excursion of the particle parallel to the magnetic field. A trapped particle has $E < \mu B_{max}$, while a transit particle has $E > \mu B_{max}$. Ignored above are higher order terms in the gyroradius to scale length ratio, which include centripetal offsets in θ and ψ and higher harmonics in ξ due to inhomogeneous magnetic field.

The expansion above in ρ/L_R is well justified, since $L_R >> \rho$ everywhere in the octupole. But the condition $\rho/L_B < 1$ breaks down in the regions of the octupole where the magnetic field is particularly small. This can be seen quite clearly along the separatrix, which passes through a magnetic field null (figures 2.2 and 2.3). In fact, the adiabatic invariant μ is not conserved near

this field null. Bearing this qualification in mind and that the conditions do hold through much of the octupole away from the null, we continue with the analysis.

B5. Expansions

ϕ depends on $\chi(t')$ and $\psi(t')$, and it is convenient to define ϕ as a product of the functions $H(\chi)$ and $G(\psi)$. (This separation is justified by the observed wave structure.) H defines the mode structure along a field line, while G defines the mode structure across psi surfaces. Expanding $G(\psi(t'))$ in a Taylor series about $\psi(t)$ yields

$$G(\psi(t')) = G(\psi(t)) + \left\{ \frac{RB}{\Omega} [2\mu B/m]^{1/2} \left[t' \right]_t \right\} G'(\psi(t)) \qquad (6.11)$$

$$+ \left\{ \frac{RB}{\Omega} [2\mu B/m]^{1/2} \left[t' \right]_t \right\}^2 G''(\psi(t))$$

where we have made an expansion using $\rho = [2\mu B/m]^{1/2}$ as a small quantity with respect to the scale length of G.

Trapped particles bouncing in the local magnetic wells of a multipole sample the parallel structure $H(\chi)$ of the wave potential ϕ. Depending on its pitch angle $v_\parallel/v_\perp$ a particle will sample more or less of H, due to varying "depths" of trapping. Further, a particle will sample various portions of H for differing lengths of time, depending on the particle's changing $v_\parallel$. Circulating particles sample all of $H(\chi)$, but they, too, have a changing $v_\parallel$. Using a particle's bounce (circulation) frequency, one can describe $H(\chi(t'))$

as seen by a particle in bounce harmonics[2], which is just a Fourier series

$$H(\chi(t')) = \sum_{p=-\infty}^{\infty} H_p \exp(ip\omega_b \hat{t}) \tag{6.12}$$

where $\hat{t} = \int^{\chi(t')} d\chi/\dot{\chi}$ and $\omega_b(\mu,E) = 2\pi \oint d\chi/\dot{\chi}$. As mentioned above, the component H_p depends on the individual particle's pitch angle in velocity space.

We can express the exponential in θ of equation 6.9 as a sum of Bessel functions

$$\exp\{il(\theta(t') - \theta(t))\} = \sum_m \sum_n J_m(k_\perp\rho)_t \, J_n(k_\perp\rho)_{t'} \cdot \exp\{i(n-m)\xi_0\} \exp\{in\int d\tau\, \Omega\} \exp\{-i\int d\tau\, \omega_d\} \tag{6.13}$$

where the summations are from $-\infty$ to ∞ the integrals are from t' to t, $k_\perp\rho = [2\mu B/m]^{1/2}/R\Omega$, and $\omega_d = lB\,[\mu B/m + v_\parallel^2]/\Omega \cdot \partial \ln B/\partial\psi$.

B6. Phase Angle Average

Substituting the expressions of equations 6.4, 6.11, and 6.13 into equation 6.9 and taking a phase angle average over ξ_0 yields

$$\frac{\langle f\rangle_\xi}{F_{Max}} = \frac{-q\,\phi}{T}(1 + \alpha(\psi_0 - \psi)) - \frac{iq}{T}(\omega - \omega_*)(1 + \alpha(\psi_0 - \psi)) \sum_m J_m \int_{-\infty}^{t} dt'\, e^{i\omega(t-t')}\, e^{-i\int d\tau\, \omega_d}\, e^{mI} \tag{6.14}$$

$$\cdot\Big[J_m G + (J_{m-1} + J_{m+1})\frac{KG'}{2} - (J_{m-1}e^{-I} + J_{m+1}e^{I})\frac{K(t)G'}{2}$$

$$+(2J_m + J_{m+2} + J_{m-2})\frac{K^2 G''}{8} + (2J_m + J_{m-2}e^{-2I} + J_{m+2}e^{2I})\frac{K(t)^2 G''}{8}$$

$$-(J_m(e^{I}+e^{-I}) + J_{m-2}e^{-I} + J_{m+2}e^{I})\frac{KK(t)G''}{4}\Big]\ H$$

where $k_\perp\rho$ is the argument of J; $\psi(t')$ is the argument of G, G', and G"; $\chi(t')$ is the argument of H; $K = [2\mu B/m]^{1/2}RB/\Omega$; and $I = i\int_t^{t'} d\tau\ \Omega$. Unless otherwise noted, the terms in the integrand are functions of t'. A factor $\alpha RB(-v_d/\Omega + \rho\cos(\xi))$ from the distribution function F is ignored with respect to $(1 + \alpha(\psi_0 - \psi))$ in the expression above $(\rho/L_n < 1)$, consistent with the ordering taken to this point.

B7. Integration by Parts

In the next step, the integration by parts over t' is performed, keeping only the leading term. A denominator of the form $(n\Omega + \omega - \omega_d - p\omega_b)$ is generated, but since Ω is much larger than all the other frequencies, only the n=0 terms are kept.

$$\frac{\langle f\rangle}{F_{Max}} = \frac{-q\ \phi}{T}(1 + \alpha(\psi_0 - \psi)) \tag{6.15}$$

$$\frac{-q}{T}(1 + \alpha(\psi_0 - \psi))\ (\omega - \omega_*)\ \sum_p \frac{\exp(ip\omega_b \hat{t})}{\omega_d - \omega + p\omega_b}$$

$$\cdot\Big[J_0^2 H_p G + J_0 J_1 G''\ \frac{\mu B^2/m}{k_\perp \rho \Omega^2}\ (R^2 B H_p + (R^2 B H)_p)\Big]$$

where use is made of equation 6.12, including the generalization of a bounce average over R^2BH. The G′ term is missing above, due to the identity $J_1+J_{-1}=0$. Ignored terms in the integration by parts contain time derivatives of $J_m(k_\perp\rho)$ for m=0,1,2. This approximation does ignore a large variation of $k_\perp\rho_i$ along a field line. From this point J_m terms must be treated as functions of a poloidally averaged $k_\perp\rho_i$ to be consistent.

B8. Quasineutrality and Quadratic Form

To proceed to a dispersion relation, the integral over velocity space is performed to find the perturbed density and quasineutrality is invoked (Poisson's equation with $k^2\lambda^2_{Debye} \ll 1$).

However, equation 6.13 is very complicated with respect to its velocity dependence. The quantities F_{Max}, $k_\perp\rho$, ω_d, ω_b, H_p, and $(R^2BH)_p$ are all dependent on velocity. The equation retains a great deal of generality, retaining radial and parallel structure in ϕ, with the assumptions $\omega \ll \Omega$ and $\rho < L_R, L_B, L_n$. Different authors resolve this difficulty by reducing the complexity of the equation in different ways.

Krall and Rosenbluth[5] solve a simpler problem, ignoring parallel structure to obtain an equation of the form $\partial^2 G/\partial\psi^2 + Q(\psi)G = 0$. This is solved for an eigenfunction $G(\psi)$ and an eigenvalue ω using a WKB formulation. This option is not open, since we wish to include the poloidal structure of the mode.

Coppi and Minardi[2], on the other hand, ignore the radial structure and create a quadratic form from the quasineutrality

condition. The quadratic form they obtain is $\int d\chi\ B^{-2}\ \phi^*(n_i-n_e)$, which is the electric potential energy of the fluctuation in a flux surface, set equal to zero to find ω. As mentioned in section A, we follow their method, with modifications.

We ignore the radial structure of the mode and solve for the dispersion relation one flux surface at a time. The assumption is made that the observed radial structure will show up as a variation of the growth rate for different flux surfaces, with the greatest growth rate coinciding with the largest amplitude of the wave.

Ignoring the radial structure of the wave ($G''=0$) and taking the velocity integral yields

$$\frac{n}{n_0} = \frac{-q\phi}{T} - \frac{qG}{T}(\omega-\omega_*) \int d^3v \left(\frac{m}{2\pi T}\right)^{3/2} e^{-E/T}\ J_0^2 \sum_p \frac{H_p \exp(ip\omega_b \hat{t})}{\omega_d - \omega + p\omega_b} \quad (6.16)$$

Before constructing the quadratic form from equation 6.16, some simplifying approximations are made. The magnetic drift frequency ω_d, a function of χ, is set equal to its value for thermal particles, removing its velocity dependence. The bounce frequency ω_b is replaced by $k_\parallel v_\parallel$ and the pitch angle dependence of H_p is dropped in favor of using the value of H_p for transit particles, in effect allowing all particles to sample the full range of $\phi(\chi)$. This approximation is defended by pointing out that both trapped and untrapped particles do sample very similar parallel structures, due to the periodicity of the mode seen in the experiment. As in the

time integration by parts leading to equation 6.15, the χ dependence of J_0 is ignored. The quadratic form becomes

$$0 = \left(\frac{1}{T_e} + \frac{1}{T_i}\right) \sum_p \int \frac{d\chi}{B^2} H_p H_p^* \tag{6.17}$$

$$+ \frac{\omega - \omega_{*e}}{T_e} \int dv_\parallel \frac{\exp(-m_e v_\parallel^2/2T_e)}{[2\pi T_e/m_e]^{1/2}} \sum_p \sum_r \int \frac{d\chi}{B^2} H_p H_r^* \frac{\exp(i(p-r)k_\parallel x_\parallel)}{\omega_{de} - \omega + pk_\parallel v_\parallel}$$

$$+ \frac{\omega - \omega_{*i}}{T_i} I_0 e^{-b} \int dv_\parallel \frac{\exp(-m_i v_\parallel^2/2T_i)}{[2\pi T_i/m_i]^{1/2}} \sum_p \sum_r \int \frac{d\chi}{B^2} H_p H_r^* \frac{\exp(i(p-r)k_\parallel x_\parallel)}{\omega_{di} - \omega + pk_\parallel v_\parallel}$$

where I_0 is the modified Bessel function with argument $b = k_\perp^2 T_i/m_i \Omega_i$, and $x_\parallel$ is the distance along the parallel direction. No I_0 term appears for the electrons because of the very small electron gyroradius. In the usual drift wave ordering $v_i \ll \omega/k_\parallel \ll v_e$ the electron velocity integration contributes only an imaginary term due to resonant electrons, unless H_0 is non-zero. The ion term, on the other hand, is real, ω_i being too small to promote Landau damping. However, if terms of order $\omega/k_\parallel V_e$ and $k_\parallel V_i/\omega$ are retained, then the electrons contribute a real term and the ions contribute a second real term.

B9. Odd Symmetry Mode

Equation 6.17 forms the dispersion relation for a drift wave, given a particular temperature for ions and electrons, a drift frequency as a function of parallel coordinate χ, and a parallel

structure for ϕ in terms of H_p. From chapter 5 we have seen that the wave of interest has odd symmetry along χ and forms a standing wave. This suggests that a viable model for the octupole could have H_p non-zero for p = 2 or -2 only or, in view of the up-down symmetry of the octupole, that H_p be non-zero for p = 1 or -1 in the upper half of the octupole. Choosing $2H(\chi) = 2H_1 \sin(k_\parallel x_\parallel) = -i[H_1 \exp(ik_\parallel x_\parallel) - H_1 \exp(-ik_\parallel x_\parallel)]$ with the origin of $x_\parallel$ in the inner nose, yields the dispersion relation for the odd symmetry mode

$$0 = \left(\frac{1}{T_e} + \frac{1}{T_i}\right) \int \frac{dx_\parallel}{B} H_1^2 \sin^2(k_\parallel x_\parallel) \tag{6.18}$$

$$+ \frac{\omega - \omega_{*e}}{T_e k_\parallel V_e} \int \frac{dx_\parallel}{B} H_1^2 \sin^2(k_\parallel x_\parallel)\, Z\left(\frac{\omega - \omega_{de}}{k_\parallel V_e}\right)$$

$$+ \frac{\omega - \omega_{*i}}{T_i k_\parallel V_e} I_0(b)\, e^{-b} \int \frac{dx_\parallel}{B} H_1^2 \sin^2(k_\parallel x_\parallel)\, Z\left(\frac{\omega - \omega_{di}}{k_\parallel V_i}\right)$$

where $V_j = \sqrt{2T_j/m_j}$ and $Z(\zeta) = [\pi]^{-1/2} \int_{-\infty}^{\infty} dy\, (y - \zeta)^{-1} \exp(-y^2)$ is the plasma dispersion function. With the usual drift wave ordering ($k_\parallel V_e \gg \omega, \omega_d \gg k_\parallel V_i$), and $T_e = T_i$ we obtain

$$0 = \left(2 + i\sqrt{\pi}\, \frac{\omega - \omega_{*e}}{k_\parallel V_e}\right) \int \frac{dx_\parallel}{B} \sin^2(k_\parallel x_\parallel) \tag{6.19}$$

$$+ (\omega + \omega_{*e})\, I_0(b)\, e^{-b} \int \frac{dx_\parallel}{B} \frac{\sin^2(k_\parallel x_\parallel)}{\omega_{di} - \omega}$$

The terms above can be identified as follows: The two is the Boltzmann response of the electrons and the ions, the term with the imaginary coefficient is the electron resonant response, and the last term is the ion non-Boltzmann response, containing the finite $k_\perp\rho$ effect and a Doppler-shifted denominator, due to magnetic curvature and gradient effects.

The dispersion relation of equation 6.19 is used in the next chapter to make an analysis of the experimental situation.

References for Chapter 6

1. P. H. Rutherford and E. A. Frieman, "Drift Instabilities in General Magnetic Field Configurations", Physics of Fluids 11, 569 (1968).

2. B. Coppi and E. Minardi, "Transport and Particle Scattering Due to Toroidal Plasma Modes", Physics of Fluids 16, 1021 (1973).

3. S. Yoshikawa, "Low-Frequency Instabilities", in Methods of Experimental Physics, ed. R. H. Lovberg and H. R. Griem, (Academic Press, New York, 1971), volume 9A, chapter 8.

4. N. A. Krall and A. W. Trivelpiece, Principles of Plasma Physics, (McGraw-Hill, New York 1973), chapter 7.

5. N. A. Krall and M. N. Rosenbluth, "Low-Frequency Stability of Nonuniform Plasmas", Physics of Fluids 6, 254 (1963).

CHAPTER 7 - RESULTS OF THEORETICAL MODEL

In this chapter the drift wave dispersion relation of equation 6.19 is solved to find the conditions for instability. The variable parameters used in this study are:

1. Ion gyroradius parameter, $\beta = I_0(b)e^{-b}$, where $b = k_\perp^2\rho_i^2$
2. Magnetic drift velocity, $\omega_{di}(x_\parallel) = 2\ (d\ \ln B/d\ \ln N)\ \omega_{*e}$
3. Poloidal magnetic field strength, $B(x_\parallel)$

The implications of the conditions for instability are discussed for the octupole.

In section A the poloidal structure of ω_{di} and B for the octupole are presented for reference. In section B the slab model of the drift wave is considered, for which ω_{di} and B are constant in $x_\parallel$. In section C the approximations $\omega_{di} = \varpi_d(1 + \kappa \cos(2k_\parallel x_\parallel))$ and $B^{-1} = B_0^{-1}(1 + 2\lambda\cos^2(k_\parallel x_\parallel))$ are made. In section D the actual values for $\omega_{di}(x_\parallel)$ and $B(x_\parallel)$, as presented in section A, are used. Sections B and C involve an analytic treatment of the integral, while section D uses a numerical algorithm.

A. Poloidal Variation in the Octupole

Figures 7.1 through 7.4 illustrate the actual ω_{di} structure of the octupole. The figures show d $\ln B/d\psi$ for Ψ = 4, 5, 6, and 7 versus the distance along a field line $x_\parallel$. The origin of $x_\parallel$ is located at χ = 6.4 (0.0) for flux surfaces 4 and 5 (6 and 7). (Refer to figure 2.4.) The largest value for $x_\parallel$ is located at χ = 9.84 for

all flux surfaces pictured. Figures 7.1 and 7.2 show the situation along the upper outer ring, by probe port H. Figures 7.3 and 7.4 show the situation along the upper half of the octupole.

To obtain ω_{di}/ω_{*e} from the graphs, one multiplies by two times the density scale size $2/\alpha$ (see equation 6.4). This factor $2/\alpha$ is negative for the private flux surfaces ($\psi < 5.7$) and positive for the common flux surfaces ($\psi > 5.7$), since the density has its peak on the separatrix. Thus surfaces 4 and 5 have good curvature ($\omega_{di}/\omega_{*e} > 0$) everywhere, whereas 6 and 7 have a mixture of good and bad curvature.

Figures 7.5 through 7.8 show the $\|\phi\|^2/B$ structure of the octupole, with $\|\phi\|^2 \sim \sin^2(k_\| x_\|)$ assumed. The figures show $\sin^2(k_\| x_\|)/B$ in arbitrary units for $\psi = 4$, 5, 6, and 7 versus $x_\|$. Note that the values are smaller for $\psi = 6$ and 7 when $x_\|$ is small, since the magnetic field is larger for smaller distances from the octupole's center line (1/R dependence of B).

B. Slab Model

For the slab model the magnetic field strength B and magnetic drift frequency ω_{di} are taken to be constant along a field line. The dispersion relation, equation 6.19, reduces to

$$0 = 2 + i\sqrt{\pi}\,\frac{\omega - \omega_{*e}}{k_\| V_e} + \beta\,\frac{\omega + \omega_{*e}}{\omega_{di} - \omega} \qquad (7.1)$$

This case is treated in chapter 3, where it is determined that

$$\omega_r = \frac{\beta\omega_{*e} + 2\omega_{di}}{2 - \beta} \tag{7.2}$$

$$\gamma = \frac{\sqrt{\pi}}{k_\parallel V_e} \frac{2\beta(\omega_{*e} + \omega_{di})((1-\beta)\omega_{*e} - \omega_{di})}{(2 - \beta)^3}$$

Instability occurs for $\omega_{di} < \omega_r < \omega_{*e}$.

Figures 7.9 and 7.10 illustrate the conditions on ω_{di} for instability in the slab as a function of β. Also shown are representative points for positions on flux surfaces $\psi = 4$ and 7 for a case in which the density gradient scale size $1/\alpha$ is 1.5 flux surfaces. Where the points correspond to positions accessible from a probe port, those points are marked with the probe port label. Flux surface 4 is a private flux surface, for which the magnetic curvature is good everywhere ($\omega_{di}/\omega_{*e} > 0$). It is seen that the wave is stable for all positions. Instability could be obtained, however, by decreasing the density scale length (increasing ω_{*e}) or increasing the ion gyroradius size (decreasing β). Flux surface 7 is a common flux surface, for which the average magnetic curvature is good, but for which there are regions of local bad curvature. Thus points appear on both sides of the line marking $\omega_{di} = 0$. For this flux surface the instability condition will always hold somewhere, no matter what the size of the density scale length or the size of the ion gyroradius. Note that probe ports at which nodes in the poloidal mode structure are observed experimentally lie outside of the

instability region (A and G). Probe ports for which large amplitude fluctuations are observed lie inside the instability region (B through F).

Thus the slab model agrees qualitatively with the observed radial and poloidal structures of the wave, if the analysis is done on a point to point basis. Note, however, that the slab model does not predict the upper and lower limits on β for instability which are seen in the experiment.

C. Poloidal Variation - Analytic Model

In this section we consider cases for which ω_{di} and B have a poloidal dependence. The following functions are chosen

$$\omega_{di} = \bar{\omega}_d \left(1 + \kappa \cos(2k_{\parallel} x_{\parallel})\right) \tag{7.3}$$

$$B^{-1} = B_0^{-1} \left(1 + 2\lambda \cos^2(k_{\parallel} x_{\parallel})\right)$$

where $k_{\parallel}$ is 2π divided by the distance half way around the octupole for a common flux surface, or twice the distance around a ring for a private flux surface. Note that the 1/R dependence of B is not taken into account.

Section C1 considers the case where ω_{di} varies, but B is a constant. Section C2 adds the effect of varying B.

C1. Magnetic Drift Frequency Variation

In this section B is treated as a constant and ω_{di} is allowed to

vary poloidally as in equation 7.3. The dispersion relation 6.19 becomes

$$0 = 2 + i\sqrt{\pi}\,\frac{\omega - \omega_{*e}}{k_\parallel V_e} + (\omega + \omega_{*e})\,\frac{\beta}{\pi}\int_0^{2\pi} \frac{d\theta\ \sin^2\theta}{\bar{\omega}_d - \omega + \kappa\bar{\omega}_d\cos(2\theta)} \tag{7.4}$$

where $\theta = k_\parallel x_\parallel$. Making the substitution $z = e^{2i\theta}$ transforms the integral above into an integral over the unit circle

$$0 = 2 + i\sqrt{\pi}\,\frac{\omega - \omega_{*e}}{k_\parallel V_e} - \frac{\omega + \omega_{*e}}{\bar{\omega}_d - \omega}\,\frac{\beta}{a} \tag{7.5}$$

$$+ \frac{\omega + \omega_{*e}}{\bar{\omega}_d - \omega}\,\frac{\beta(1 + 1/a)}{ia\pi}\int_c \frac{dz}{z^2 + 2z/a + 1}$$

where $a = \kappa\bar{\omega}_d/(\bar{\omega}_d - \omega)$. This equation has poles at $z = -1/a \pm [a^{-2}-1]^{1/2}$. It is solved by the method of residues to yield a dispersion relation

$$0 = 2 + i\sqrt{\pi}\,\frac{\omega - \omega_{*e}}{k_\parallel V_e} + \frac{\omega + \omega_{*e}}{\bar{\omega}_d - \omega}\,\frac{\beta}{a}\left(-1 \pm \left[\frac{1 + a}{1 - a}\right]^{1/2}\right) \tag{7.6}$$

where the sign of the square root depends on which pole is inside the unit circle. This, in turn, depends on the complex value of ω.

Solving the dispersion relation 7.6 for ω becomes a matter of solving a cubic equation in ω and testing for self-consistent solutions.

A computer routine is used to solve the cubic equation in complex ω which results from the dispersion relation 7.6. Marginally unstable solutions ($\gamma < \|\omega_r\|$) are found as a function of β, κ and $\bar{\omega}_d$.

Figures 7.11 through 7.15 illustrate the region of instability (marked #) for five values of $\bar{\omega}_d$. (The case $T_e = T_i = 10$ eV and $k_\| = 2\pi/225$ cm^{-1} is shown.) The horizontal axis shows κ from -9.8 to 9.8 in steps of 0.4. Since the mode has its peak at $\omega_{di} = (1+\kappa)\bar{\omega}_d$, a value of κ less than zero corresponds to a mode that peaks in the best curvature, while a value of κ greater than zero is a mode that peaks in the worst curvature. For $\kappa = 0$ the slab model is recovered. The vertical axis shows β from 0.01 to 1.0 in steps of 0.03. The value $\beta = 1.0$ corresponds to zero ion gyroradius ($\rho_i = 0$) and β decreases as the ion gyroradius increases.

The condition for instability is observed to obey the relationship $(1+\|\kappa\|)\bar{\omega}_d < \omega < \omega_{*e}$ when the values of ω_r are examined for the unstable points of the diagram. When κ=0 this agrees with the condition for the slab case of section B. From the diagrams it is also seen that for the slab case the condition for instability, $\beta < 1 - \bar{\omega}_{di}/\omega_{*e}$, is recovered.

As κ is made more negative, the effect is to stabilize the mode, restricting it to lower values of β (higher values of $k_\perp\rho_i$). For κ negative enough, $(1-\kappa)\bar{\omega}_d > \omega_{*e}$, the mode is stable for all values of

β. When κ is negative, the mode has its peak amplitude at the minimum of ω_{di} and is an even symmetry mode, like the drift-universal mode of Rutherford and Frieman (section 6A). Their mode, however, peaked where $k_\perp \rho_i$ was maximal, an effect not modeled in this theory.

As κ is made more positive, the effect is to cause the mode to be unstable for a range of β that is higher than for the slab case, allowing instability for smaller values of $k_\perp \rho_i$. This range of β has an upper and a lower (non-zero) bound. For κ positive enough, $(1+\kappa)\bar{\omega}_d > \omega_{*e}$, the mode is stable for all values of β. When κ is positive, the mode has its peak amplitude at the maximum of ω_{di} and is an odd symmetry mode, like the drift-ballooning mode of Rutherford and Frieman (section 6A).

For some of the cases shown in figures 7.11 through 7.15 there is the possibility of both mode symmetries for the same β value and the same $\|\kappa\|$ value. Figure 7.16 shows the same case as figure 7.11, with the dominant mode (higher growth rate) marked with a "0". When β is large, the odd symmetry mode dominates, and when β is small, the even symmetry mode dominates.

All of the figures from 7.11 through 7.15 have average good curvature, $\bar{\omega}_d > 0$, with the curvature increasing from 7.11 to 7.15. It is apparent that good curvature is a stabilizing influence, as there are fewer unstable values for β and κ as $\bar{\omega}_d$ increases. As $\bar{\omega}_d$ increases the unstable cases approach the slab model situation.

Comparison with Experiment

The results of the theory above demonstrate many of the features of the observed wave:

1. Radial Structure - The theory shows stabilization of the mode as $\bar{\omega}_d$ is increased. A radial structure is seen in the octupole consistent with this trend. In the common flux of the octupole, the line averaged curvature drift frequency (referenced to ω_{*e}) varies from about -0.06 at $\psi = 7.8$ to 0.45 at $\psi = 6.0$ ($1/\alpha = 1.5$ flux surfaces). Thus theory predicts larger growth rate for the larger ψ values, and the relative amplitude of the wave in the common flux is observed to be greater at the larger ψ values and less at the smaller ψ values. (Note that the negative $\bar{\omega}_d$ values above come from a line average of ω_{di}, whereas the average good curvature of the common flux is obtained with a dl/B averaging.) For the private flux $\bar{\omega}_d/\omega_{*e}$ ranges from about 1.5 at $\psi = 5.4$ to 0.6 at $\psi = 2.8$, assuming the same gradient scale. These surfaces are all observed to be stable, in agreement with theory. (section 5A1)

2. Ion Gyroradius Dependence - The theory exhibits a range in $k_\perp \rho_i$ (through β) for which there is an unstable odd symmetry mode. It is observed experimentally that the wave has a limited range of values of $k_\perp \rho_i$. (section 5A5)

3. Poloidal Structure - The theory predicts the predominance of the odd symmetry mode over the even symmetry mode for $\beta > 0.6$. The odd symmetry mode only is observed in the octupole for this range of β. (section 5A2)

Thus there are many qualitative agreements between the theory and the observed behavior of the drift wave in the octupole. It is difficult, however, to get direct agreement between theory and experiment using numerical data. One of the problems encountered is that the approximation for ω_{di} as a cosine does not fit the experimental data very well (figures 7.1 through 7.4). The better curvature regions tend to be narrow peaks, and the worse curvature regions broad valleys. (The cosine value offers the advantage of ease of handling in the theory, however.) One is left with a range of $\bar{\omega}_d$ and κ which could be a reasonable fit to the data, but this range is often large.

As an example of a problem that comes up when attempting to get good numerical agreement between experiment and theory, consider the case of $\psi = 6.6$. For this flux surface $\bar{\omega}_d = 0.1$ and $\kappa = 5$, approximately. From figure 7.11, this case should be unstable to the drift wave for $0.65 < \beta < 1.0$. However, when the experiment is done at the large magnetic fields that correspond to $\beta \cong 1.0$, no drift wave is observed.

A feature of the theoretical model that is not observed in the octupole is the even symmetry mode, predicted for small β values. Only the odd symmetry mode is ever seen in the octupole.

In conclusion, the theory to this point works very well as a guideline for drift wave behavior in the octupole, but its predictions are not exact.

C2. Magnetic Field Strength Variation

In this section both B and ω_{di} are allowed to vary poloidally as in equation 7.3. The dispersion relation 6.19 becomes

$$0 = \left(2 + i\sqrt{\pi}\,\frac{\omega - \omega_{*e}}{k_{\parallel} V_e}\right) \int_0^{2\pi} d\theta\, (1 + \lambda + \lambda \cos(2\theta))\, \sin^2\theta \qquad (7.7)$$

$$+ \beta\, \frac{\omega + \omega_{*e}}{\bar{\omega}_d - \omega} \int_0^{2\pi} d\theta\, \frac{(1 + \lambda + \lambda \cos(2\theta))\, \sin^2\theta}{1 + a \cos(2\theta)}$$

where $\theta = k_{\parallel} x_{\parallel}$ and $a = \kappa\bar{\omega}_d/(\bar{\omega}_d - \omega)$. The solution to this equation is obtained in the same manner as for equation 7.4, by a transformation to an integral over the unit circle, using the substitution $z = e^{2i\theta}$. A quartic equation for $\omega = \omega_r + i\gamma$ is obtained which is solved with a computer routine. We follow the solution of section C1 to see how the poloidal variation of B modifies it.

Figure 7.17 shows the results for the case $\bar{\omega}_d = 0.12$, $\kappa = 6.7$, $T_e = T_i = 10$ eV, and $k_{\parallel} = 2\pi/225$ cm^{-1}. The growth rate γ is plotted as a function of λ for $\beta = 1.0$, 0.9, 0.8, and 0.7. This plot uses an approximation for $\psi = 7.4$ (common flux) with $1/\alpha = 2.0$ flux surfaces.

For $\lambda = 0$ the constant B case treated in section C1 is recovered. Note that in this situation $\beta = 1.0$ and 0.9 are unstable, but $\beta = 0.8$ and 0.7 are both stable. This is a similar situation to the example treated at the end of section C1, where $\bar{\omega}_d = 0.1$ was

examined. The mode is stabilized by finite ion gyroradius. But as λ is increased, the mode at $\beta = 1.0$ is stabilized, while the others are destabilized. With a large enough increase in λ each mode becomes stable in turn, highest β values first. (As a point of reference λ varies from 9 at $\psi = 6.0$ to 2 at $\psi = 7.8$. On the separatrix $\psi = 5.7$, which goes through a field null, $\lambda = \infty$.)

For $\lambda \cong 1$ the theory predicts a structure in β similar to that seen in the experiment, where instability occurs between a maximal value of β less than 1.0, and a minimal value of β greater than 0. This effect is not solely attributable to the poloidal variation of B, however. A similar result can be obtained by changing the poloidal dependence of $\|\phi\|^2$ from the $\sin^2(k_\| x_\|)$ dependence assigned to it in chapter 6.

The conclusion of this section is that the mode's β dependence is due to the poloidal dependences of ω_{di}, B, and $\|\phi\|^2$. By varying these dependences, modes with the experimentally observed β dependence can be generated.

D. Poloidal Variation - Numerical Model

A numerical routine is used to analyze the dispersion relation of equation 6.19 using the actual values of $\omega_{di}(x_\|)$ and $\sin^2(k_\| x_\|)/B(x_\|)$ for the octupole (figures 7.1 through 7.4 and 7.5 through 7.8). The algorithm replaces the integral of the dispersion relation with a summation and provides special handling of the regions close to the condition $\omega = \omega_{di}$. Specifically, a spline fit to a function of second order in $x_\|$ is made for both numerator and

denominator in the region of the pole, and the integral is done analytically.

The method of solving for $\omega = \omega_r + i\gamma$ involves a two step process. In the first step, the real part of the dispersion relation is considered, using the condition $\gamma << \|\omega_r\|$ for a marginally unstable wave.

$$0 \cong 2 \int \frac{dl}{B} \|\phi\|^2 + \beta(\omega_r + \omega_{*e}) \int \frac{dl}{B} \frac{\|\phi\|^2}{\omega_{di} - \omega_r} \tag{7.8}$$

The right hand side of equation 7.8 is evaluated for different values of ω_r until a result is obtained that can be made arbitrarily close to zero. In the second step, this value of ω_r is used in the imaginary part of the dispersion relation 6.19 below

$$0 \cong i\sqrt{\pi} \frac{\omega_r - \omega_{*e}}{k_\| V_e} \int \frac{dl}{B} \|\phi\|^2 + i\gamma\beta \int \frac{dl}{B} \frac{\omega_{di} + \omega_{*e}}{(\omega_{di} - \omega_r)^2 + \gamma^2} \|\phi\|^2 \tag{7.9}$$

This equation for γ is solved by varying γ to get a result close to zero.

An iterative procedure can be followed, if terms $\sim\gamma$ are retained in equation 7.8.

When the approximations for ω_{di} and $1/B$ from section C1 are used in the numerical algorithm, the same results are obtained as in section C1.

Figure 7.18 shows γ as a function of Ψ for the private flux surfaces at $\beta = 1$. All of these flux surfaces are stable. However, if β is reduced, the surface $\Psi = 4.4$ becomes unstable for $\beta < 0.5$. For the common flux surfaces, the situation is shown in figure 7.19. These flux surfaces are unstable for $\beta = 1.0$ or 0.8, with greater growth rate for the $\beta = 1.0$ case and slightly greater growth rate for higher values of Ψ. It is also noted that for the common flux surface cases, $\omega_r << \omega_{*e}$, typically $0.1\ \omega_{*e}$. For the stable private flux surfaces $\omega_r > \omega_{*e}$.

The numerical routine shows some of the features of the experiment, notably the stabilization of good curvature. It also shows a destabilizing ability of the ion gyroradius term β (for the private flux surfaces), and it shows a stabilizing ability of β (for the common flux surfaces). The greater growth rate at $\beta = 1.0$ than at $\beta = 0.8$ does not agree with the experimental result (stability at $\beta = 1.0$), but the comments made in section C2 about the effect of the poloidal dependence of $\|\phi\|^2/B$ on the β dependence of the mode might be usefully applied here.

E. Summary

The methods of theoretical drift wave analysis have been adapted to the octupole magnetic configuration (multipole with poloidal field only, large magnetic drifts) and plasma characteristics (density maximum on Ψ_{sep}, no temperature gradients, $k_\perp \rho_i \lesssim 1$). The analysis has revealed that some of the structure of the observed mode can be

explained by features of the theory. At the same time, the theory does not give a completely accurate description of the octupole. Its usefulness lies in being a guide for interpretation of experimental results and an indicator of effects that might be sought out in the experiment.

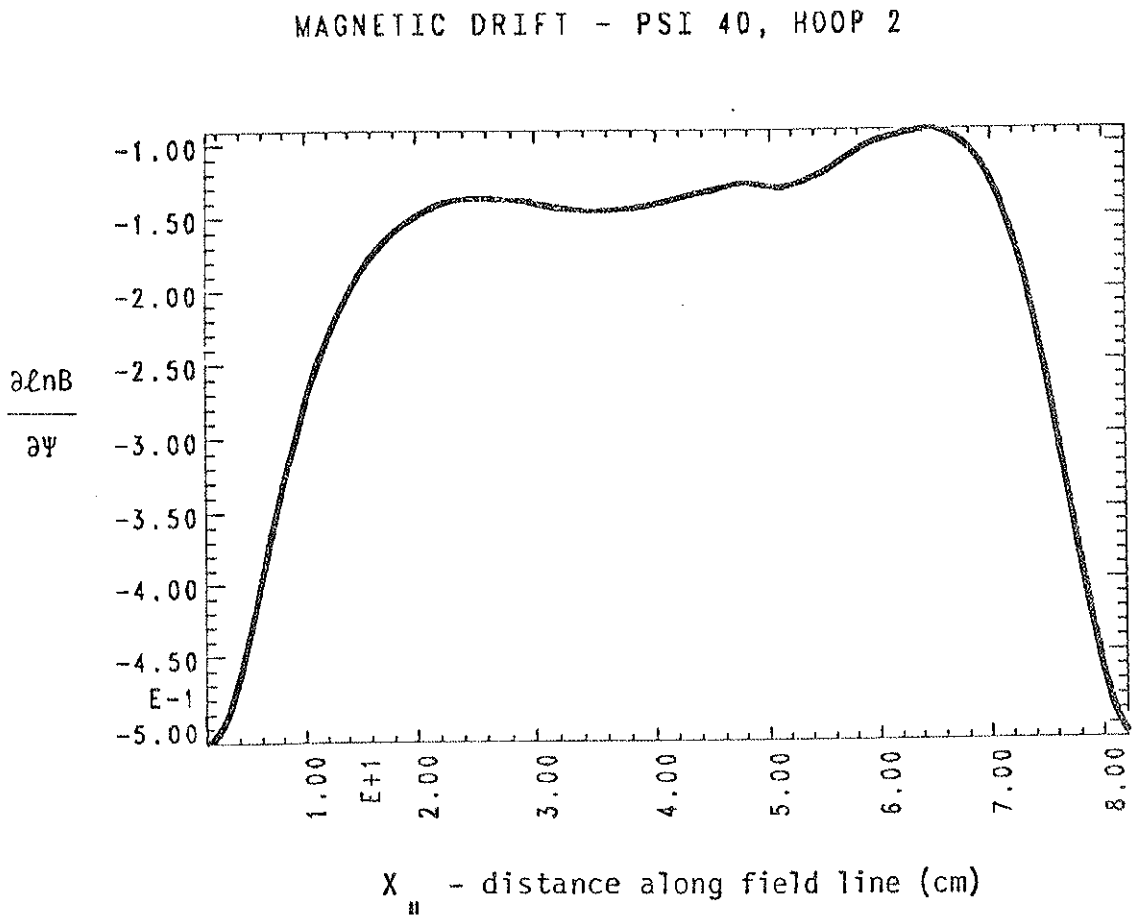

Figure 7.1 - Magnetic Drift for $\Psi = 4.0$ (Private Flux)

The quantity $\partial \ln B/\partial \Psi$ is shown as a function of poloidal position for an outer ring. ($\omega_{di} = 2\omega_{*e}\, \partial \ln B/\partial \ln N$)

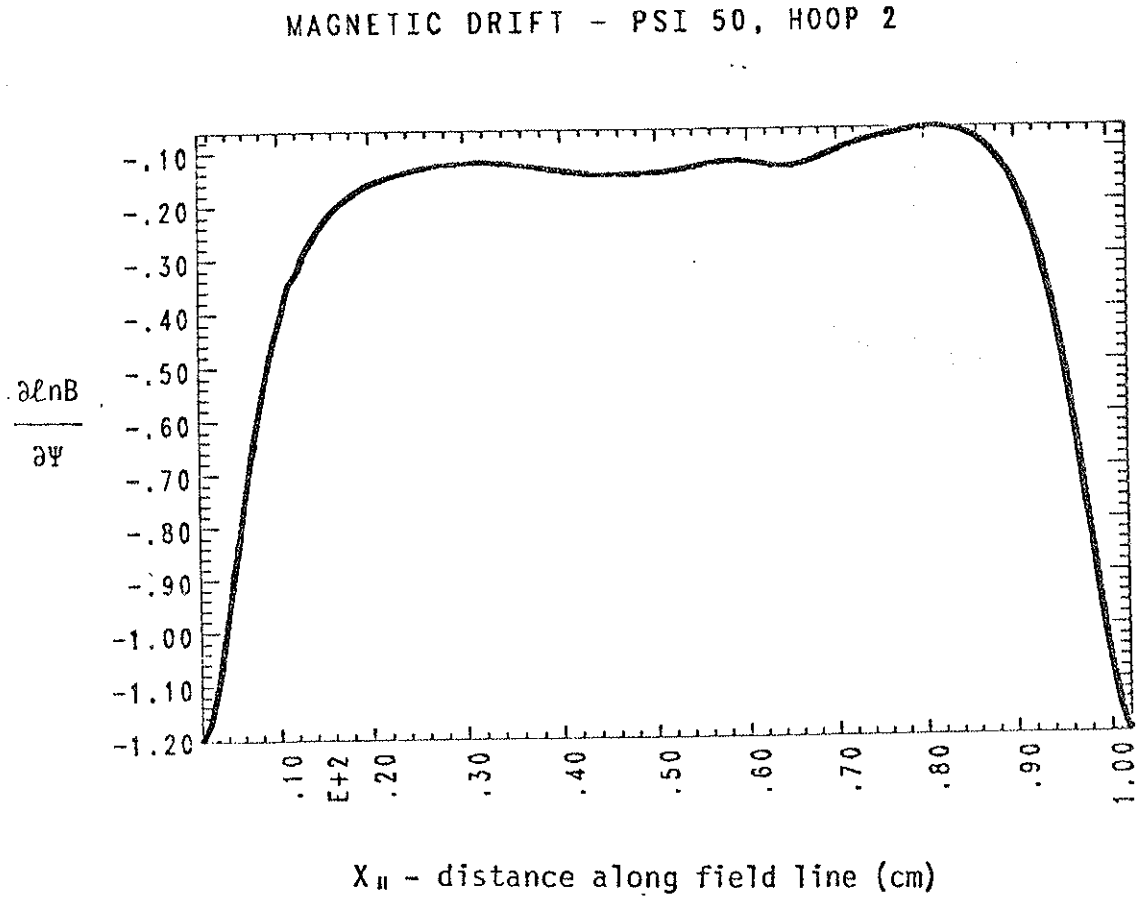

Figure 7.2 - Magnetic Drift for Ψ = 5.0 (Private Flux)

The quantity ∂lnB/∂Ψ is shown as a function of poloidal position for an outer ring. ($\omega_{di} = 2\omega_{*e}\ \partial \ln B/\partial \ln N$)

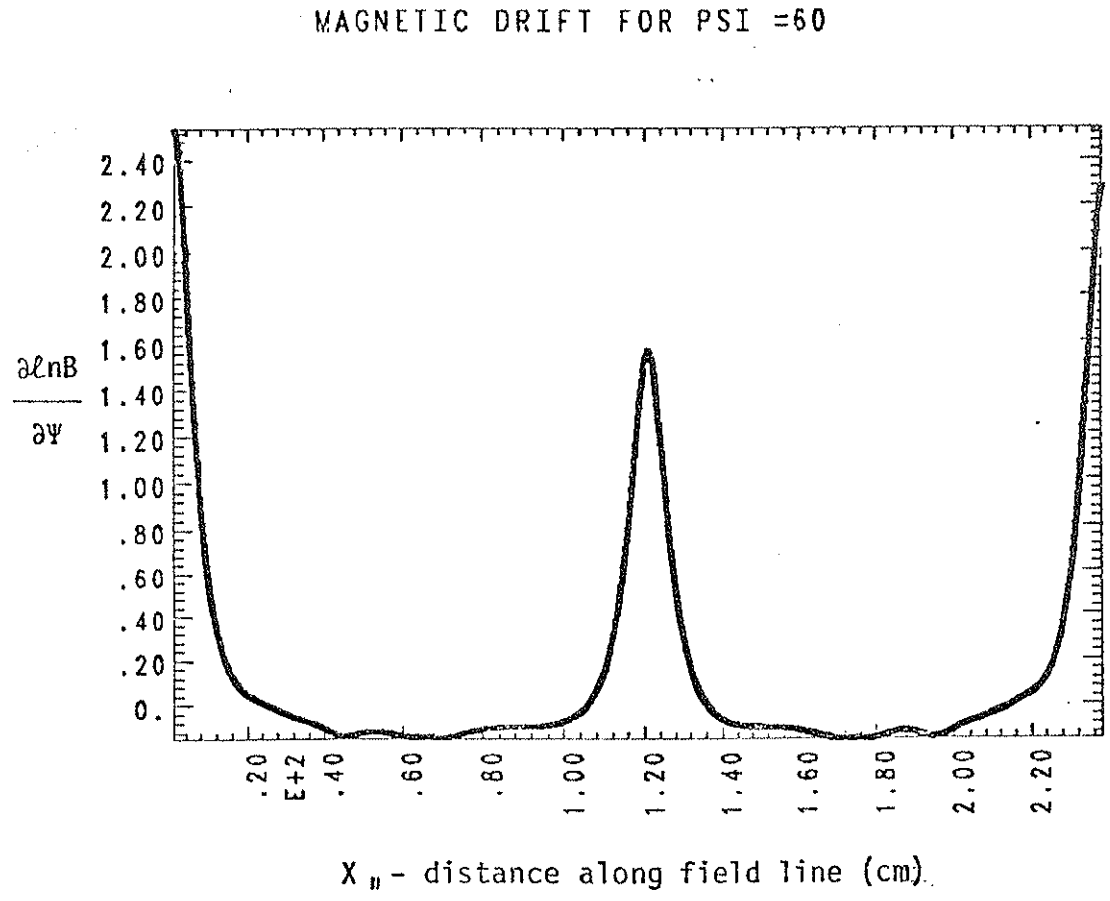

Figure 7.3 - Magnetic Drift for Ψ = 6.0 (Common Flux)

The quantity $\partial \ln B/\partial \Psi$ is shown as a function of poloidal position for the upper half of the octupole. ($\omega_{di} = 2\omega_{*e}\, \partial \ln B/\partial \ln N$)

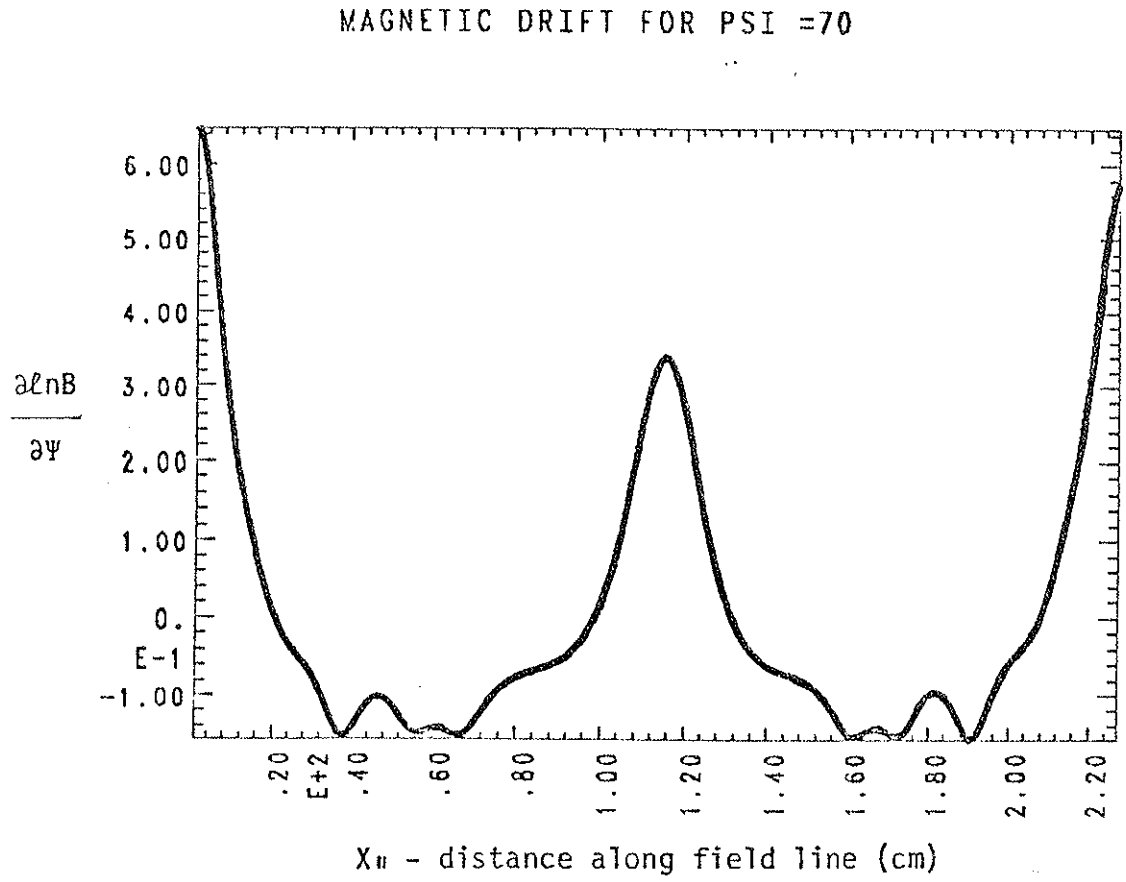

Figure 7.4 - Magnetic Drift for Ψ = 7.0 (Common Flux)

The quantity $\partial \ln B/\partial \Psi$ is shown as a function of poloidal position for the upper half of the octupole. ($\omega_{di} = 2\omega_{*e}\, \partial \ln B/\partial \ln N$)

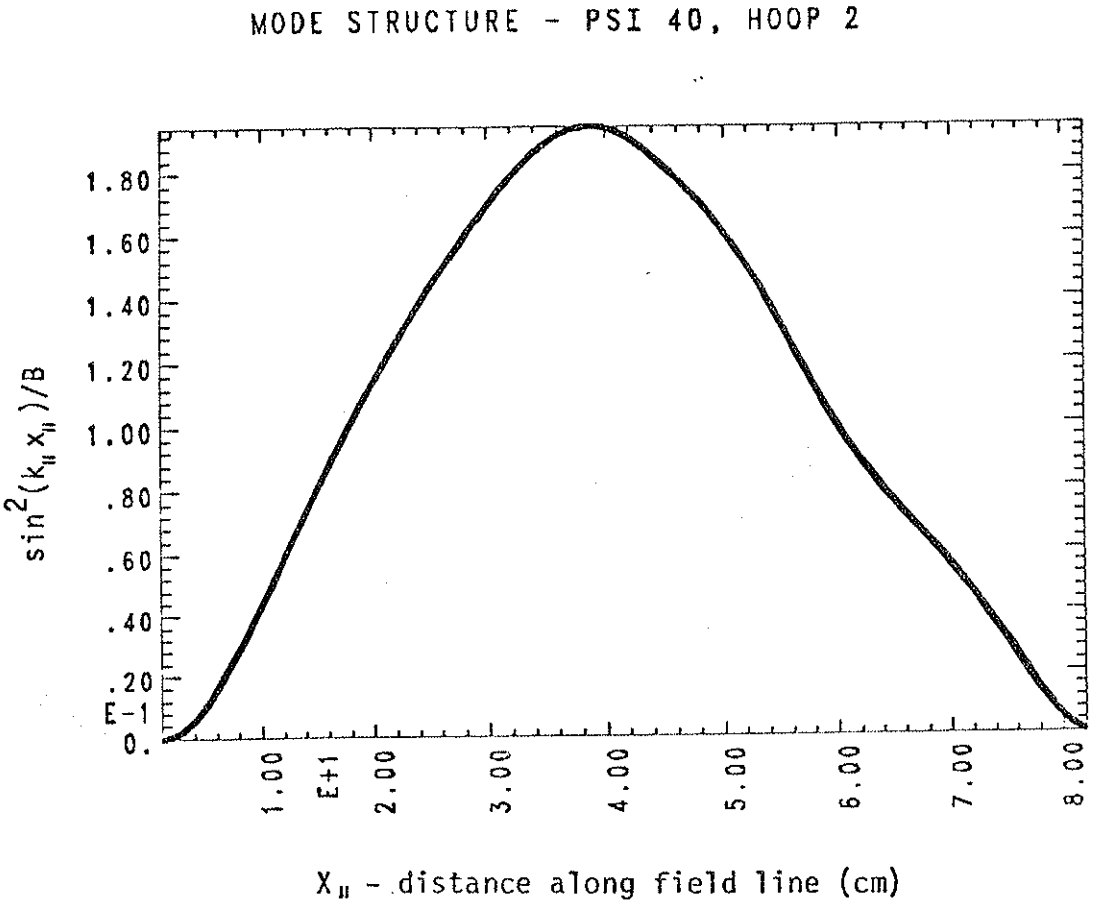

Figure 7.5 - Mode Structure for Ψ = 4.0 (Private Flux)
The quantity $|\phi|^2/B$ is shown as a function of poloidal position for an outer ring.

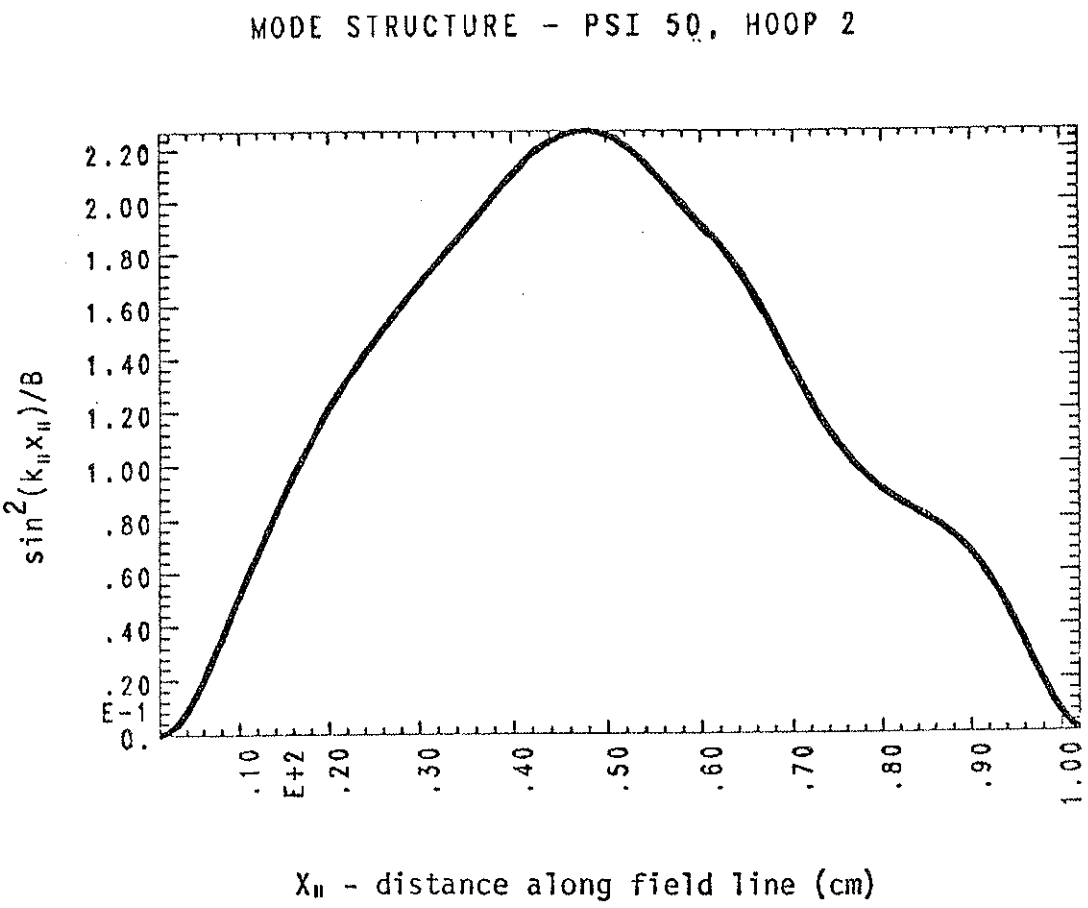

Figure 7.6 - Mode Structure for Ψ = 5.0 (Private Flux)
The quantity $|\phi|^2/B$ is shown as a function of poloidal position for an outer ring.

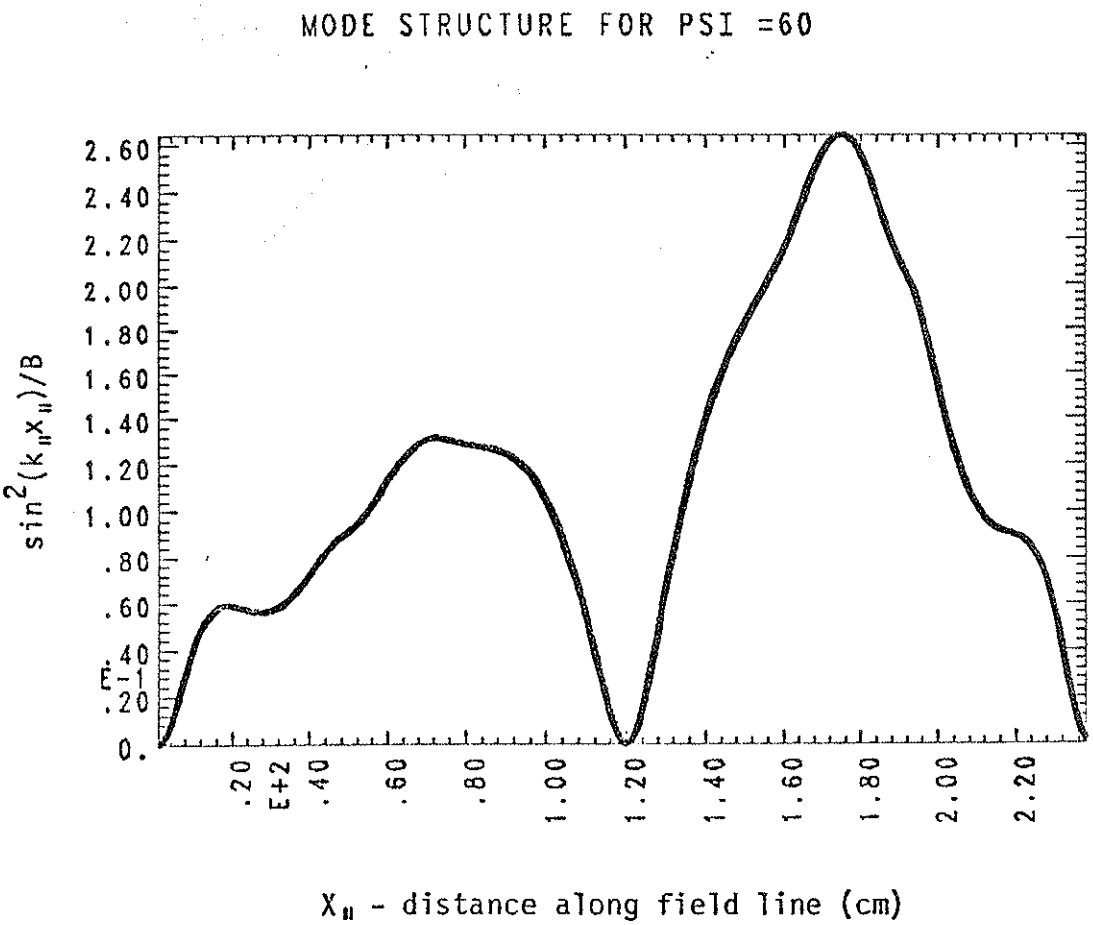

Figure 7.7 - Magnetic Drift for Ψ = 6.0 (Common Flux)

The quantity $\|\phi\|^2/B$ is shown as a function of poloidal position for the upper half of the octupole.

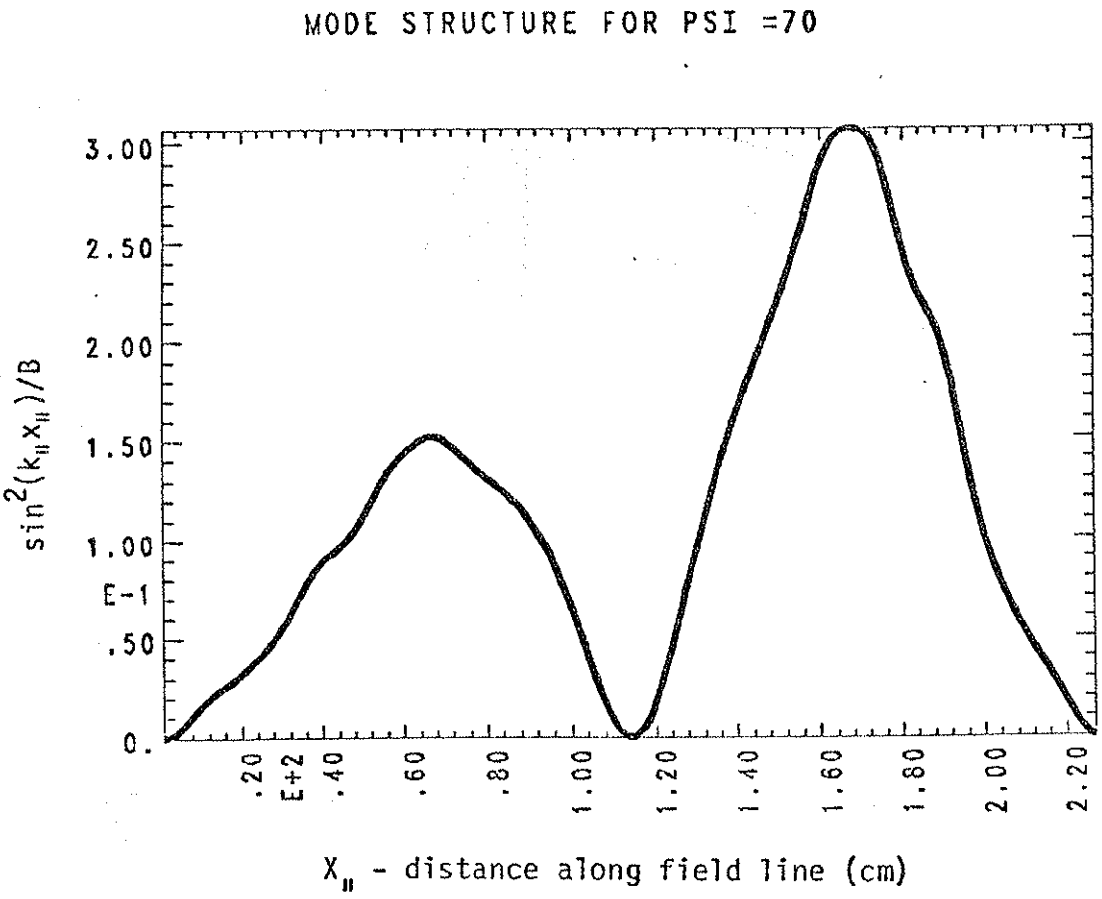

Figure 7.8 - Magnetic Drift for Ψ = 7.0 (Common Flux)

The quantity $\|\phi\|^2/B$ is shown as a function of poloidal position for the upper half of the octupole.

qualitatively all the major observed trends: a mode with odd poloidal symmetry, stabilization of the mode with increasing good magnetic curvature, and a limited range of $k_\perp \rho_i$ for instability. The theory does not, however, agree with the experimental results in numerical detail.

B. Suggestions

The results of this experimental study suggest further investigations which might be undertaken to gain a fuller understanding of the drift wave in the levitated octupole.

Of particular interest is an accurate measurement of the phase and magnitude of the fluctuating plasma potential compared to the fluctuating density. These quantities are crucial for determining the expected transport due to the drift wave. In addition, a measurement of $e\tilde{\phi}/T_e$ compared to $\tilde{n}/n_0$ reveals how the saturated drift wave differs from the expectation of linear theory, $e\tilde{\phi}/T_e = \tilde{n}/n_0$. Determining the plasma potential to good accuracy, however, is difficult, due to the role of the electron temperature (section 4B1). Motley[2] undertook such a study in a Q-machine, using a heated filament Langmuir probe.

A related project is finding the equilibrium plasma potential gradient to good accuracy. With this information, one could determine the ExB induced Doppler shift of the wave frequency, and a comparison with the diamagnetic frequency ω_{*e} could be made.

The stabilization of the drift wave with toroidal field appears to be an area where great progress could be made. The sharp onset of stability is a feature which makes this phenomenon amenable to study. The topic of shear stabilization is an active one in the theory community today, and a definitive experiment which touched on this topic would be very significant.

It would also be interesting to see whether a transition from a purely electrostatic wave to a wave incorporating magnetic fluctuations is observed as the plasma density is further increased to the 10^{13}/cc level and beyond (decreasing C_{Alfven})[3].

More work could be done on the theory, with the understanding that a level of great complexity can quickly be reached, resulting in diminishing returns to the experimentalist interested only in a simulation. One way to extend the theory is to include the effects of trapped particles in an explicit manner. Another is to include the poloidal variation of $k_\perp \rho_i$, an effect which may effect the role of even symmetry waves in the octupole[4].

References for Chapter 8

1. B. Coppi and E. Minardi, "Transport and Particle Scattering Due to Toroidal Plasma Modes", Physics of Fluids 16, 1021 (1973).

2. R. W. Motley, "Hot Probe Measurements of Space Potential Oscillations in a Plasma", Journal of Applied Physics 43, 3711 (1972).

3. B. B. Kadomtsev, Plasma Turbulence, (Academic Press, New York, 1965).

4. P. H. Rutherford and E. A. Frieman, "Drift Instabilities in General Magnetic Field Configurations", Physics of Fluids 11, 569 (1968).